

Quantitative Methods for *In Vitro* and *In Vivo* Characterization of Cell and Tissue Metabolism

by

Gregory James Ekchian

B.S. Biomedical Engineering
Boston University, 2009

M.Eng. Materials Science and Engineering
Massachusetts Institute of Technology, 2010

Submitted to the Department of Materials Science and Engineering
in Partial Fulfillment of the Requirements for the Degree of

Doctor of Philosophy

at the

Massachusetts Institute of Technology

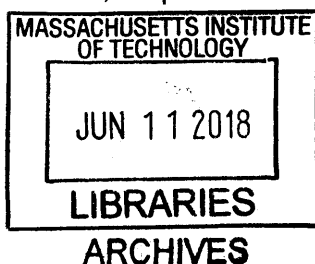
June 2018

© 2018 Massachusetts Institute of Technology. All rights reserved.

Signature of Author: _____ **Signature redacted**
Department of Materials Science and Engineering
April 27, 2018

Certified by: _____ **Signature redacted**
Michael J. Cima
David H. Koch Professor of Engineering
Thesis Supervisor

Accepted by: _____ **Signature redacted**
Donald R. Sadoway
Chairman, Departmental Committee on Graduate Studies



Page Intentionally Left Blank

Quantitative Methods for *In Vitro* and *In Vivo* Characterization of Cell and Tissue Metabolism

by

Gregory James Ekchian

Submitted to the Department of Materials Science and Engineering

on April 27, 2018

in Partial Fulfillment of the
Requirements for the Degree of
Doctor of Philosophy

Abstract

Characterization of cell and tissue metabolism is critical for the diagnosis and tracking of disease and the development and implementation of new treatments. Metrics for metabolism span tissue oxygen and pH levels and cellular thermal output. This need is present in research and clinical applications both of which are underserved by existing technologies. This thesis presents the development of three distinct technologies: an implantable oxygen sensor for clinical monitoring of tumor oxygen content in cervical cancer, an *in vitro* screening platform for monitoring thermal output in a multi-well plate format, and an implantable pH sensor.

This thesis presents a silicone-based quantitative oxygen sensor for clinical use in cervical cancer. Oxygen measurements are made using MRI, which is already part of the clinical workflow for this patient population. This sensor is Institutional Review Board approved for a ten-patient clinical trial in women with pathologically-confirmed cases of cervical cancer. Hypoxia has been linked to poor clinical outcomes, including lower survival rates. Hypoxia-induced resistance to radiotherapy presents an intriguing clinical opportunity because boosting the radiation dose can overcome the radiotherapy resistance present in hypoxic tumor subvolumes. Existing oxygen-sensing methods are not sufficient to enable customization of radiation therapy dose delivery, necessitating the development of new sensing technologies.

The presented work covers the validation and use of a system to measure thermal output from biological and chemical systems. Plate-based screening platforms offer significant advantages over existing alternatives that require substantial deviations from standard experimental protocols. Applications of this platform include screening of new treatments in cell culture and determining the extent of chemical reactions.

This thesis also presents the development of an implantable polymeric pH sensor. It is hydrogel based and provides quantitative measurements of tissue pH levels using MRI.

Measurements of tissue pH are of interest in a number of clinical applications including chemotherapy selection and monitoring tumor response. The oxygen and pH sensors can be used simultaneously to provide parallel measurements of both metrics of metabolism.

Thesis Supervisor: Michael J. Cima

Title: David H. Koch Professor of Engineering

Table of Contents

| | |
|---|----|
| Acknowledgements | 7 |
| List of Figures..... | 9 |
| List of Tables | 14 |
| Chapter 1: Introduction | 16 |
| Fundamentals of Magnetic Resonance Imaging | 16 |
| Qualitative Magnetic Resonance Imaging..... | 18 |
| Quantitative Magnetic Resonance Imaging | 19 |
| T ₁ Relaxation Time..... | 20 |
| T ₂ Relaxation Time..... | 23 |
| Sensor Mechanisms of Action | 26 |
| Diatomic Nature of Molecular Oxygen | 26 |
| Magnetization Transfer | 26 |
| Chapter 2: <i>In Vivo</i> Oxygen Sensor in Cervical Cancer | 29 |
| Background..... | 29 |
| The Role of Oxygen in Oncology | 29 |
| Overcoming Hypoxia-Induced Resistance | 31 |
| High Dose-Rate Brachytherapy..... | 33 |
| Image-guided High Dose Rate Brachytherapy | 34 |
| Dose Delivery..... | 34 |
| Existing Oxygen-Sensing Methods..... | 35 |
| Silicone Oxygen Sensors using H ¹ Magnetic Resonance Imaging | 36 |
| Improvements to the Clinical Work Flow..... | 38 |
| Early Feasibility Clinical Trial – Cervical Cancer..... | 39 |
| Oxygen Sensor Design and Deployment..... | 40 |
| Results | 46 |
| MRI Data Collection..... | 46 |
| MRI Parameter Selection | 49 |
| Equilibration..... | 53 |
| Mechanical Testing | 55 |
| Discussion | 59 |
| Clinical Embodiment 1 | 60 |
| Clinical Embodiment 2 | 60 |
| Methods | 61 |
| Catheter Machining | 61 |
| Silicone Mixing and Curing | 61 |
| Silicone Filling, Capping, and Sealing | 62 |
| MRI Data Acquisition and Processing..... | 63 |
| Signal-to-Noise Ratio Calculation | 63 |
| Voxel Selection Process | 64 |
| Mechanical Testing | 65 |
| Chapter 3: Plate-Based Thermal Screening Platform..... | 69 |
| Introduction..... | 69 |

| | |
|---|------------|
| Background..... | 69 |
| Direct Methods of Characterizing Thermal Output | 69 |
| Thermal Measurements in Biological Systems..... | 70 |
| Oxygen Consumption Measurement Methods..... | 70 |
| System Design – Thermal Screening Platform | 71 |
| System Validation | 73 |
| Thermal Crosstalk | 76 |
| Background Evaporation..... | 77 |
| Thermal Excursion from Liquid Transfer | 78 |
| Results..... | 79 |
| Measurement of Thermal Output from Chemical Reactions | 79 |
| Measurement of Thermal Output from Biological Systems..... | 80 |
| Oxygen at Cell Monolayer – Seahorse FX Analyzer | 81 |
| Discussion | 90 |
| Methods | 91 |
| Data Collection | 91 |
| Power Output Calibration | 92 |
| Cell Culture..... | 92 |
| Oxygen Consumption Measurements | 93 |
| Thermistor Calibration | 93 |
| Chapter 4: Quantitative pH Sensor..... | 95 |
| Background..... | 95 |
| Results..... | 97 |
| Further Expansion of the pH Range | 99 |
| Synthesis Process Improvements | 100 |
| Discussion | 102 |
| Methods and Materials | 103 |
| pHEMA Synthesis | 103 |
| Co-polymer Synthesis | 103 |
| Relaxometry Measurements | 103 |
| Experimental Setup..... | 103 |
| Chapter 5: Conclusions and Future Work..... | 106 |
| References | 108 |

Acknowledgements

The experience as a graduate student is often filled with a mix of emotions, ebbing and flowing between the highs of something proceeding exactly as expected or the lows of initially unexplainable results. While I have certainly experienced many aspects of this, I feel lucky that my journey through graduate school has been one of constant learning and focused on productive steps toward implementing clinically impactful technologies. This has been a process I have thoroughly enjoyed, and it has positively influenced my life in many ways. I did not take this journey alone, and it would not have been possible without those around me.

First, I would like to thank my advisor, Professor Michael Cima. Michael has created an environment for his students to thrive that blends mentorship and guidance with the opportunity for students to lead technology development and to take ownership and responsibility for the projects they work on. Michael has served as my mentor since I first joined his lab as a master's student in the fall of 2009. Since then, I have had the pleasure to interact with Michael on different levels and in many distinct settings. I feel lucky to have re-joined his lab for my PhD in 2013. I am truly grateful for the opportunities he has provided me over the last decade, and I know that it has served as the foundation for me as an engineer, inventor, and innovator. I look forward to a continued relationship with Michael to develop high impact medical technologies.

I would also like to thank my thesis committee, Professor Darrell Irvine and Professor Niels Holten-Andersen. They have both been an invaluable resource as I have progressed through my research. Their feedback and comments have served to improve and refine my research for which I am extremely grateful.

The second half of my PhD has focused on translating our oxygen-sensing technology. I have been truly fortunate to develop a technology that is actively translating to the clinic. This work wouldn't be possible without the Bridge Project Expansion Grant available at

the Koch Institute in collaboration with the Harvard Cancer Center. I also want to thank our collaborators, Doctor Larissa Lee, Professor Robert Cormack, and Professor Junichi Tokuda and those who have helped make the connections that made this collaboration a reality, Doctor Mary-Ellen Taplin and Professor Nobu Hata. Their willingness to discuss our project and make connections to those conducting relevant clinical research has been much appreciated as we look to further develop this technology.

My labmates and classmates have been an integral part of my graduate school experience. They have served as sounding boards for new ideas, provided moral support, and have been the source of many true and lasting friendships -- friendships that I know will stretch well beyond our time at MIT. I am grateful that MIT brought us together and am excited to see what impact we will collectively have on the world.

I would like to thank the many people who have worked with me on developing these technologies for their input and creativity. You have all been a true pleasure to work with.

I would also like to thank my family who have unequivocally encouraged me from a young age. Their unconditional support of my professional and educational endeavors has been a source of consistency in my life that I have come to rely on.

To all, I am truly grateful.

List of Figures

| | |
|---|----|
| Figure 1 (A) Spins are randomly oriented when no magnetic field is applied. (B) The spins are aligned in the parallel and anti-parallel states when a magnetic field is applied. | 17 |
| Figure 2 The first hydrogen MRI scan conducted by Paul Lauterbur in 1973 of two tubes containing water. Reprinted by permission from Springer Nature: Lauterbur, P. Image Formation by Induced Local Interactions: Examples Employing Nuclear Magnetic Resonance. Nature 242 (1973). | 18 |
| Figure 3 A single snapshot captured along the relaxation curve of two different tissues. Tissue 1 is more relaxed than tissue 2 at the time of data collection. Selection of delay period between excitation measurement can be adjusted to highlight the difference between different tissues and tissue and exogenous materials. | 19 |
| Figure 4 The process of collecting a single point during an inversion recovery pulse sequence. The duration between B and D dictates the inversion time. Data must be collected with multiple inversion times to obtain the necessary points to fit the inversion recovery equation. | 21 |
| Figure 5 Shows multiple snapshots of intensity measured along the T1 relaxation recovery curve. Each of these snapshot measurements would be made during a separate relaxation cycle during traditional data acquisition processing. Each cycle requires excitement and subsequent relaxation of the system. | 22 |
| Figure 6 The net magnetization is flipped once into the transverse plane. 180 degree refocusing pulses are applied to the net magnetization. A measurement is made once per refocusing pulse. | 24 |
| Figure 7 Each point corresponds to a measurement made following a refocusing pulse. This is repeated until the system is fully relaxed. | 25 |
| Figure 8 The exchange of protons between free water molecules and the polymer backbone produces a pH-dependent measurable signal. The exchange of protons is catalyzed in both acidic and basic environments. | 27 |
| Figure 9 Patients with hypoxic tumors suffer a 30% lower survival rate at three years compared to patients with more well-oxygenated tumors. Tumor hypoxia is characterized by hypoxic fraction, the percentage of measurements made with a pO ₂ below 5 mmHg. Reprinted from Radiotherapy and Oncology, Volume 53, Issue 8, Knocke, T. H., Weitmann, H. D., Feldmann, H. J., Selzer, E. & Pötter, R. Intratumoral pO ₂ -measurements as predictive assay in the treatment of carcinoma of the uterine cervix, 99-104 (1999), with permission from Elsevier. | 31 |

| | |
|--|----|
| Figure 10 Comparison of survival fraction for cells irradiated in different oxygen environments. Reprinted by permission from Springer Nature: Nature Reviews Cancer, Brown, J. M. & Wilson, W. R. Exploiting tumour hypoxia in cancer treatment. Nat Rev Cancer 4, 437-447, doi:10.1038/nrc1367 (2004). | 32 |
| Figure 11 Radio-biological modeling supporting dose escalation for hypoxic tumors. Well oxygenated (.-), normal oxygen levels (--) and hypoxic (solid). ⁴⁰ | 33 |
| Figure 12 Examples of silicone oxygen sensors. The silicone sensor can be produced in multiple formats and shapes due to the elastomeric matrix. | 37 |
| Figure 13 The theoretical relationship between the T_1 relaxation time and oxygen concentration. The relaxation time of the sensor is greatest when no oxygen is present and decreases as the concentration of oxygen increases. | 38 |
| Figure 14 A modified version of the existing brachytherapy treatment catheter that incorporates the oxygen-sensing silicone. | 41 |
| Figure 15 A cross-section of the oxygen sensor catheter. The red layer is a higher viscosity silicone that is used to plug the holes for oxygen diffusion. The blue layer is a more oxygen-sensitive silicone blend. The black layer is a Delrin plug. The yellow layer is a light cure acrylic epoxy to seal the silicone from the ambient oxygen in the lumen of the catheter. | 42 |
| Figure 16 The purple template is used to define the position of catheters during the treatment planning process. The red catheters denote the oxygen-sensing catheters. The oxygen-sensing catheters will be inserted along the obturator. These catheters may be removed after the measurement and replaced with treatment catheters during the study. | 43 |
| Figure 17 Compares the relaxation time of silicone oils with a range of viscosities under conditions of 0% and 21% oxygen. Data collected using Bruker Minispec (0.5 T).. | 45 |
| Figure 18 A schematic of the MRI phantom. The MRI phantom has three separate tubes for gas exposure. The phantom is filled with water to mimic human tissue. The tubes are positioned relative to the endorectal coil such that they span the range of distances from the coil expected in vivo. The spin coil is under the phantom and the body-matrix coil is placed on top of the phantom. | 47 |
| Figure 19 The MRI phantom with the endorectal coil inside the phantom and the body-matrix coil placed on top of the phantom. The spin coil is in the bed of the MRI. | 48 |
| Figure 20 MRI scan of the phantom. The endorectal coil is positioned at the far left. Three tubes containing catheters are shown spaced evenly across the phantom. Each tube can have the environmental oxygen concentration modified in real-time to test the kinetic response of the catheter to changes in oxygen concentration. Folding of the | |

| | |
|--|----|
| scan can be seen in the lower portion of the scan represented by the brighter white band. Accurate measurement of the catheters requires that they be outside the folding region..... | 48 |
| Figure 21 The body-matrix (left) and endorectal (right) coils. | 49 |
| Figure 22 SNR decreases moving away from the endorectal coil. The decreased SNR reduces the ability to accurately fit the relaxation data and decreases resolution... | 50 |
| Figure 23 Data collected with TR=3000 ms and TR=5000 ms have equivalent relaxation times and amplitudes indicating that the shorter relaxation time is suitable for clinical use. | 52 |
| Figure 24 Shows the equilibration of catheters in response to switching from an air environment to a nitrogen environment. The point at T=0 was under an air environment. The red region denotes the time points to be collected during in vivo measurements. The green region denotes the data collection window. The time points represent the mid-point of the data acquisition window. The intensity values that are used to obtain a relaxation time are collected over 42 minutes. N=6 error bars represent one standard deviation. TP is used to abbreviate time point..... | 54 |
| Figure 25 Shows the measured relaxation time at time point zero which was in an environment with 21% oxygen and once equilibrated at time point four in a 0% oxygen environment. Time point zero is significantly different from time points four, five and six ($p < 0.001$) and time points four, five and six are not significantly different. N=6, error bars represent a single standard deviation..... | 55 |
| Figure 26 The relationship between failure force and catheter height is a linear relationship. The height is defined from the tip of the catheter to the top of the epoxy layer. The height displayed is from the tip of the catheter to the top of the epoxy layer. The high friction tests were conducted against 400 grit sandpaper. Forces shown are forces at the catheter tip, the frictional force associated with contact between the catheter and the template has been subtracted from the measured force. | 57 |
| Figure 27 Catheters tested with and without lubrication showed equivalent use and termination forces. The unlubricated state represents a worst-case scenario of minimal lubrication during insertion or interference with an unlubricated surface. .. | 58 |
| Figure 28 A) The external surface of the oxygen-sensing catheter. The oxygen-sensitive silicone is spaced discretely along the outer surface. B) The cross-section of the catheter with the inner lumen to accept the insertion stylet, reader coil, and radioactive treatment source. | 61 |
| Figure 29 The cross-section plane through the catheter. | 64 |

| | |
|--|----|
| Figure 30 An MRI scan of the catheter containing the silicone oxygen sensor. Scan shows a 2 mm slice. Each voxel is 0.41 mm x 0.41 mm x 2 mm. A 5 by 5 grid is selected. Each pixel is fit individually. A final determination of points is made based on a weighted average by SNR of the 8 highest SNR points. | 65 |
| Figure 31 The catheter is gripped around the circumference 1 inch from the distal end. The catheter is gripped with four mutually perpendicular set screws. | 66 |
| Figure 32 An anatomically oriented mechanical test setup was used to test catheters in the format used in vivo. | 67 |
| Figure 33 Thermistor array on PCB. Custom well plates are placed on top of the array. The middle column of components measures thermal output from each well. The outer columns on each side do not measure temperature, but are designed to keep the well plate level. Pairings of thermistors across (right side minus left side) the board produce the differential measurement. Pairings from top to bottom of the board are denoted 1 to 8. Photo by Alex Lammers. | 72 |
| Figure 34 The passive corrugated aluminum enclosure reduces the standard deviation of the temperature during a steady-state period by almost 50%. Data processing techniques to further subtract remaining thermal background fluctuations reduced the standard deviation to under 10% of the incubator fluctuations. | 74 |
| Figure 35 The real-time micro calorimeter enables rapid mixing. The four images show the mixing of cell culture media colored with different water-soluble dyes. (A) Before liquid transfer, (B) 0.25 seconds after liquid transfer begins, (C) one second after liquid transfer begins, and (D) two seconds after liquid transfer begins. | 75 |
| Figure 36 Resistor-based calibration of the system shows a linear response that is statistically equivalent for channels 4 and 5. Each calibration point is n=7. The linear fit of the averages across both channels has an $R^2 = 0.9962$ | 76 |
| Figure 37 Power is dissipated in channels 4 and 5. The thermal crosstalk is measured in the neighboring wells on either side. The thermal signal is measurable in all channels. | 77 |
| Figure 38 The power output as a result of evaporation. Power levels determined by monitoring well strip weight. | 78 |
| Figure 39 Power dissipated from a urea hydrolysis reaction. n=2 at each power dissipation level. The data points are overlapping for the two lower power dissipation levels. | 80 |
| Figure 40 Basal oxygen consumption rate for a range of cell densities. | 82 |

| | |
|---|-----|
| Figure 41 Time course response of DNP addition to C2C12 cells. The response was best sustained for 50 μ M DNP. Higher concentrations of DNP were not observed to increase the OCR response and, in some cases, produced a smaller increase. | 83 |
| Figure 42 The difference in OCR between the basal period before DNP addition and the 60 – 160 minute window after DNP addition. Per cell power outputs were normalized assuming 30% of the cell monolayer was contributing to the measurement. | 84 |
| Figure 43 The partial pressure drops in response to the probe being positioned immediately above the cell monolayer. The probe first measures oxygen consumption prior to DNP (two minute measurement window) and after DNP addition with a two minute measurement window, 3 minute measurement window, four minute measurement window, and a two minute measurement window. Five measurements were made under each configuration. | 85 |
| Figure 44 Example time course of oxygen measurement in a static environment. Liquid transfer occurs at 189 minutes. | 87 |
| Figure 45 The decrease in partial pressure is driven by the increased height rather than the response to DNP. | 88 |
| Figure 46 OCR was independent of the presence of silicone oil on top of the media. In all cases (with and without DNP), a decrease in OCR was observed after the liquid transfer. | 89 |
| Figure 47 The relationship between T_2 relaxation time of a pHEMA based sensor and pH. | 97 |
| Figure 48 The T_2 relaxation profile of four co-polymer configurations of DMAEMA and AA. Configurations were evaluated for location of the local and absolute maxima and the existence of monotonically increasing regions. | 98 |
| Figure 49 There is a low level of variability between distinct batches of copolymer pH sensors. Error bars represent the standard deviation across three samples. | 99 |
| Figure 50 The copolymer and pHEMA sensors have peak positions at distinct pH values which allows them to be used together to map the full pH range. | 100 |

List of Tables

| | |
|--|-----|
| Table 1 Design constraints and the implications of each constraint. | 44 |
| Table 2 Summary of MRI settings..... | 53 |
| Table 3 provides an overview of the formulations of the two silicone layers. | 62 |
| Table 4 Slope of partial pressures without and with DNP. | 86 |
| Table 5 Summarizes the slope of oxygen partial pressures collected with the fiberoptic probe. | 88 |
| Table 6 The synthesis configurations evaluated..... | 101 |
| Table 7 The results of the five different synthesis configurations evaluated. | 102 |

Page Intentionally Left Blank

Chapter 1: Introduction

Monitoring of oxygen and pH in living systems is important in characterizing diseased and healthy tissue, developing new treatments, and understanding how cells respond to different environments and stimuli. Changes in oxygen and pH can induce changes in living systems as well as be the result of dysregulation of another process.

This dissertation presents novel methods for quantitatively characterizing metabolism through quantification of oxygen and pH in living systems *in vivo*. Technologies covered include a novel quantitative oxygen sensor for *in vivo* use in cervical cancer patients, a novel plate-based system for characterizing thermal output in chemical and biological applications, and a new sensor for characterizing *in vivo* pH in the physiologically relevant range. The *in vivo* oxygen and pH sensors are based on the MR (magnetic resonance) response of the sensor to changes in environmental oxygen and pH levels. The mechanisms of action for each sensor are described later in this chapter. The motivations and implementation of each technology are described in detail in their respective chapters.

Fundamentals of Magnetic Resonance Imaging

NMR (nuclear magnetic resonance) is the underlying mechanism of MRI (magnetic resonance imaging). MRI is a powerful tool that produces non-invasive images of the internal structure of the human body. It is an extremely common imaging tool due to its high resolution and soft tissue contrast. MRI is used to characterize tissue in pathologies ranging from brain abnormalities to tendon injuries and cancer. There are many forms of MRI that utilize different atoms. The majority of MRI focuses on hydrogen atoms due to their ubiquity in nature and in the human body.

The magnetic moment associated with a hydrogen atom can be modeled as a bar magnet which can be influenced by an applied magnetic field. When no magnetic field is applied to a material, the spins of the individual atoms are randomly oriented (Figure 1A). There

are two possible states for each hydrogen spin when a magnetic field is applied. The spin can be parallel or anti-parallel to the applied field. The spins parallel to the field occupy a lower energy state compared to the anti-parallel spins. This difference in energy leads to a net number of spins in the parallel orientation. The net spins produce a small, but measurable, net magnetization (Figure 1B). Clinically relevant magnetic fields range from 0.5 T to 7 T. The earth's magnetic field at the surface of the planet is on the order of μT .

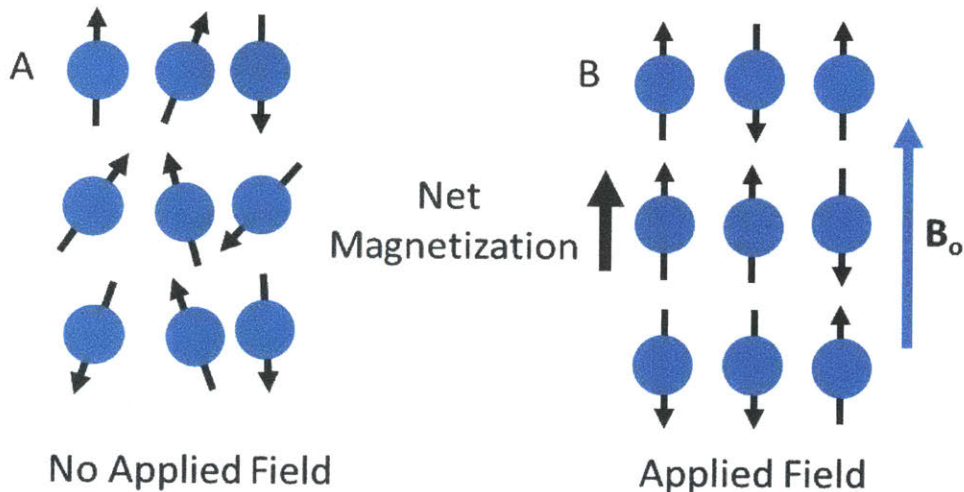


Figure 1 (A) Spins are randomly oriented when no magnetic field is applied. (B) The spins are aligned in the parallel and anti-parallel states when a magnetic field is applied.

Manipulation of the net magnetization with RF (radio frequency) pulses and measurement as it returns to the equilibrium state produces the MRI signal. Application of gradient magnetic fields enables locational information and assembly of three-dimensional MRI scans. These scans are generally a qualitative representation of the system being imaged. Early MRI scans (Figure 2)¹ were relatively low resolution and provided limited clinical utility. This work, however, laid the foundation for the modern MRI equipment used clinically today.



Figure 2 The first hydrogen MRI scan conducted by Paul Lauterbur in 1973 of two tubes containing water. Reprinted by permission from Springer Nature: Lauterbur, P. Image Formation by Induced Local Interactions: Examples Employing Nuclear Magnetic Resonance. *Nature* 242 (1973).

Many improvements have been made to MRI since Lauterbur's first scan in 1973. MRIs today have higher field strengths and better resolution and are much more user friendly. MRI, in spite of these improvements, primarily remains a qualitative imaging tool in standard clinical practice. MRI is also capable of making quantitative measurements of the human body and other proton containing materials. These methods have historically been used sparingly in clinical applications. They generally have longer scan times compared to qualitative imaging. High value applications of quantitative MRI will be discussed in this thesis.

Qualitative Magnetic Resonance Imaging

MRI leverages two distinct relaxation mechanisms, T_1 and T_2 . The T_1 relaxation time is also termed the spin-spin or longitudinal relaxation time and represents a measure of the rate at which energy is dissipated between protons in the system. The T_2 relaxation time, also termed the spin-lattice or transverse relaxation time, tracks the rate at which energy is dissipated from protons to the surrounding environment.

Clinical MRI is used primarily to conduct qualitative scans of patients. Qualitative MRI can be augmented by using contrast agents to modify the MR signal based on how much of the agent has distributed to different tissues at the time of the scan. The tissue will return to its equilibrium state faster as the concentration of the contrast agent in tissue increases. Qualitative MRI relies on a single measurement of the extent of relaxation at a single point during the recovery (Figure 3). MRI scans that are T_1 -weighted (strong influence from T_1 relaxation mechanisms) represent more relaxed tissues as brighter and less relaxed regions as darker (after passing through the null point, it is reversed before the intensity passes through zero).

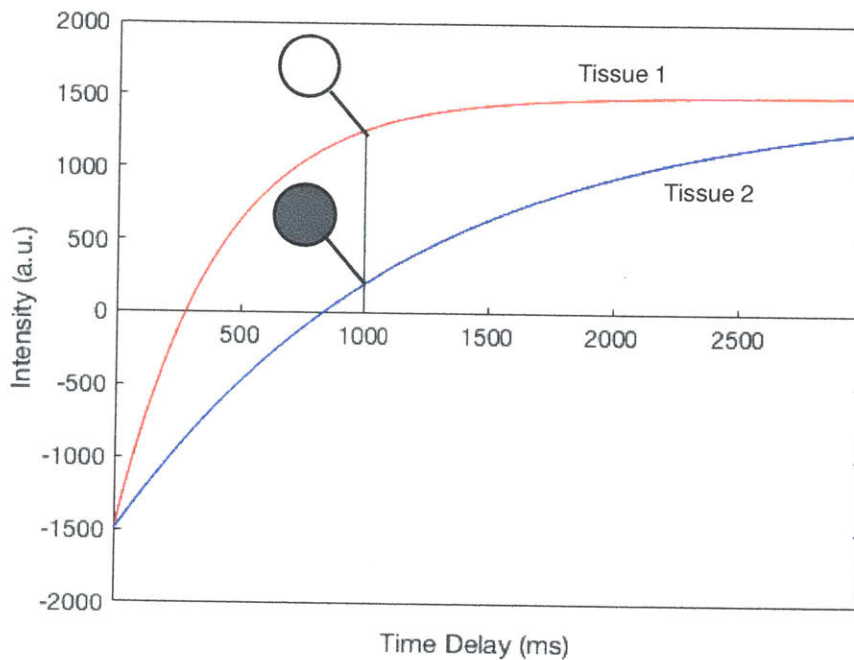


Figure 3 A single snapshot captured along the relaxation curve of two different tissues. Tissue 1 is more relaxed than tissue 2 at the time of data collection. Selection of delay period between excitation measurement can be adjusted to highlight the difference between different tissues and tissue and exogenous materials.

Quantitative Magnetic Resonance Imaging

Quantitative MRI offers the ability to further probe the healthy and diseased states of the human body and interrogate implanted exogenous materials by quantifying the degree of

the T_1 and T_2 relaxation mechanisms. It can be used to quantify tissue oxygen levels² and hydration state³ and to characterize stroke damage.⁴ Quantitative MRI provides more information than the qualitative alternatives. Quantitative MRI differs from its qualitative counterpart by requiring multiple snapshots throughout the relaxation process. This data is then processed to extract the relaxation time. The T_1 and T_2 relaxation times can each be measured.

T_1 Relaxation Time

T_1 relaxation occurs when the net magnetization is parallel to the applied magnetic field. MRI measurements, however, can only be made by measuring the component of the magnetization that is projected into the plane 90° to the direction of the applied magnetic field. The T_1 relaxation measurements generally involve a repetitive process. Relaxation is allowed to occur in the longitudinal direction before the remaining net magnetization is flipped into the transverse plane for measurement. The net magnetization immediately experiences T_2 relaxation mechanism. This process (Figure 4) produces a single intensity measurement. The system is then left to return to its equilibrium state before repeating the measurement to obtain another intensity value. The spins align parallel/anti-parallel to the applied magnetic field when the static field is applied, producing a net magnetization (Figure 4A). Energy is added to the system to flip the net magnetization 180° to the applied magnetic field (Figure 4B). The system then relaxes for a pre-determined duration (inversion time) (Figure 4C). The net magnetization is then flipped to the transverse plane for measurement (Figure 4D).

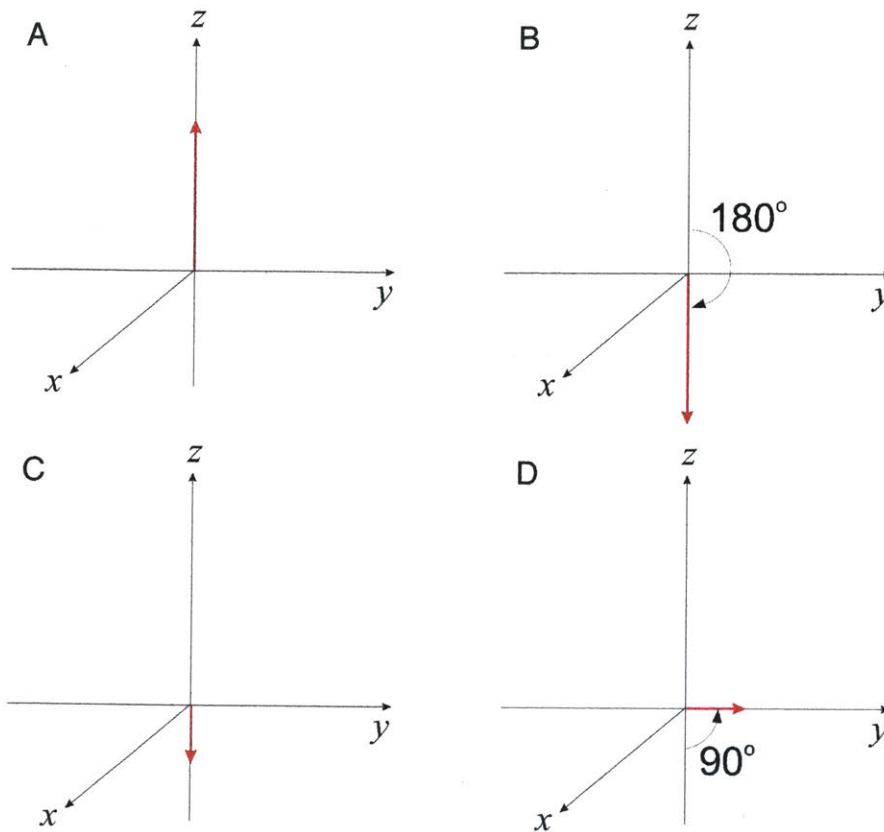


Figure 4 The process of collecting a single point during an inversion recovery pulse sequence. The duration between B and D dictates the inversion time. Data must be collected with multiple inversion times to obtain the necessary points to fit the inversion recovery equation.

Each cycle with a different inversion time produces an additional intensity measurement. Altering the delay between excitation and measurement in the transverse plane is used to develop a curve that is dependent on T_1 relaxation mechanisms (Figure 5). The different intensities are represented as different levels of brightness on the scans.

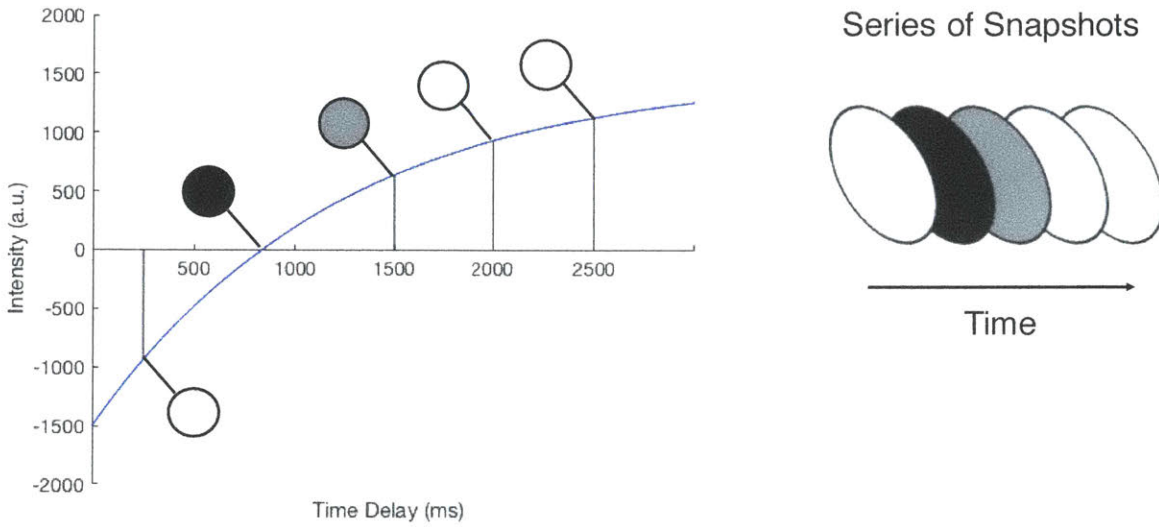


Figure 5 Shows multiple snapshots of intensity measured along the T₁ relaxation recovery curve. Each of these snapshot measurements would be made during a separate relaxation cycle during traditional data acquisition processing. Each cycle requires excitement and subsequent relaxation of the system.

This data is then fit to the inversion recovery equation and the T₁ relaxation time is extracted as a fit parameter.

$$M_z(t) = M_o(1 - 2e^{-t/T_1})$$

The T₁ relaxation time is a measure of how long it takes for the net magnetization to become 63% recovered in the direction of the applied field. The number of points collected at each inversion time and the number of inversions collected is determined by the properties of the sample and the total time allocated for data acquisition. Collection of a single point on this curve can range from seconds to many minutes depending on the sample and the type of equipment being used for data collection (single voxel benchtop system vs. human MRI).

T₂ Relaxation Time

The T₂ relaxation time characterizes relaxation due to the transfer of energy from protons to surrounding matter other than protons. The T₂ relaxation time is a measure of how long it takes for the signal in the transverse plane to relax 63%. The mechanism of T₂ relaxation occurs in the same plane where the measurement is conducted. This allows many measurements to be made in a single relaxation cycle. This can reduce scan time or allow more points to be collected for a fixed scan time measurement.

The spins align parallel/anti-parallel to the applied magnetic field when the static field is applied, producing a net magnetization (Figure 6A). Energy is added to the system to flip the net magnetization 90° to the applied magnetic field (Figure 6B). The system then relaxes for a pre-determined duration while simultaneously dephasing (Figure 6C). A 180° refocusing pulse is applied to counter the dephasing. A measurement is made after the spins are fully refocused (Figure 6D). The system continues to dephase while relaxing (Figure 6E) and another refocusing pulse is applied to enable another measurement (Figure 6F). This process is repeated to produce the T₂ relaxation curve (Figure 7A-D).

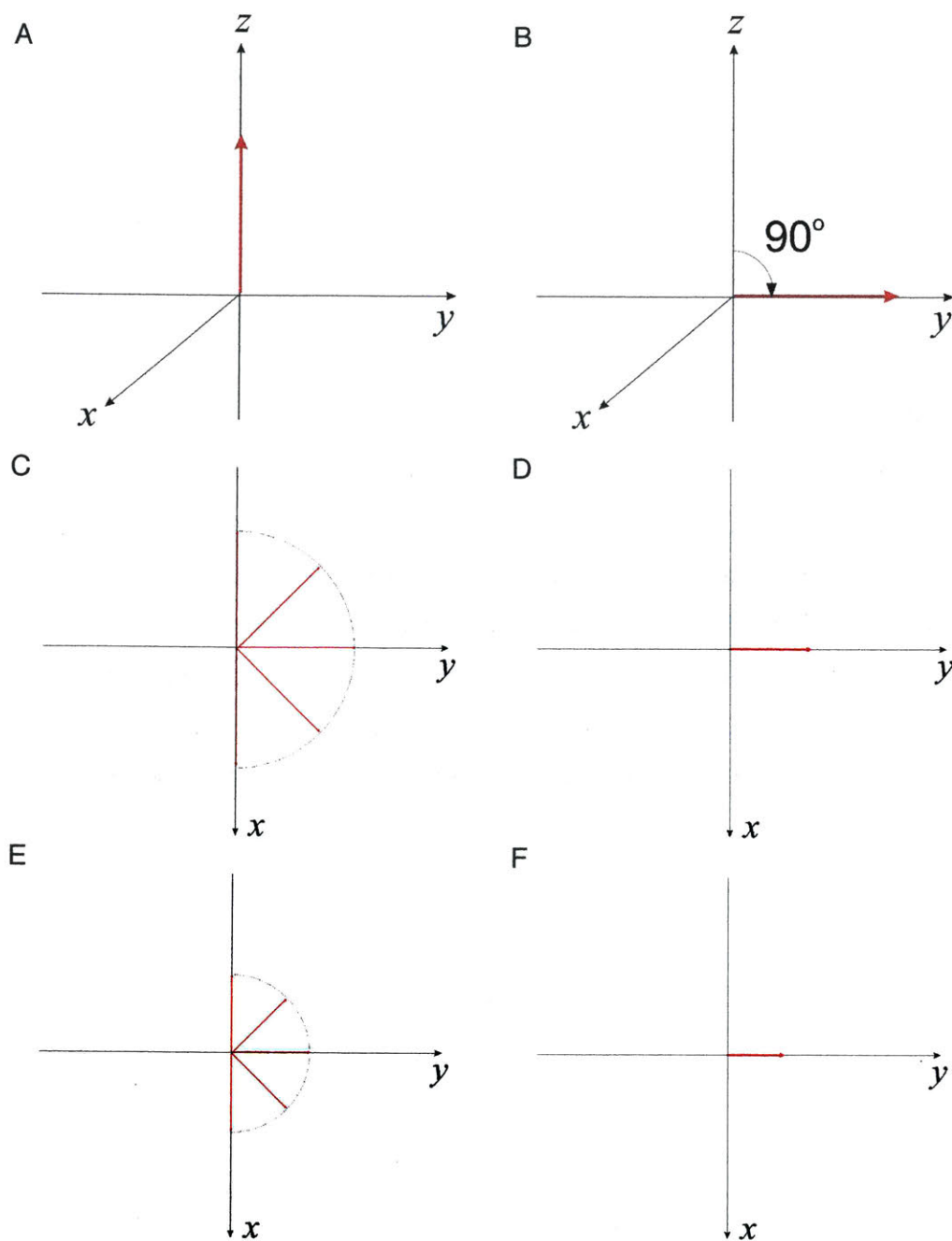


Figure 6 The net magnetization is flipped once into the transverse plane. 180 degree refocusing pulses are applied to the net magnetization. A measurement is made once per refocusing pulse.

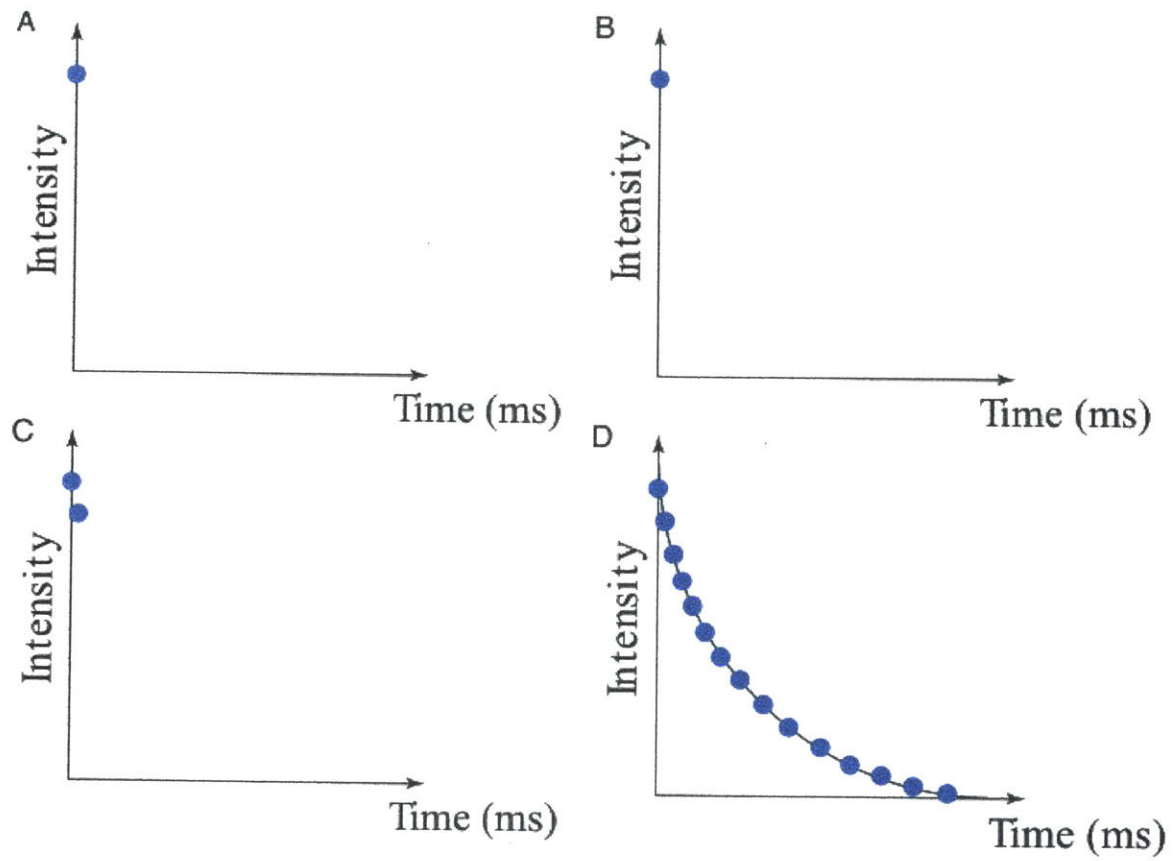


Figure 7 Each point corresponds to a measurement made following a refocusing pulse. This is repeated until the system is fully relaxed.

This data is then fit to the T_2 relaxation equation and the T_2 relaxation time is extracted as a fit parameter.

$$M_{xy}(t) = M_{xy,0}(e^{-t/T_2})$$

Sensor Mechanisms of Action

Diatomic Nature of Molecular Oxygen

Gadolinium-based contrast agents (e.g. Magnevist) are paramagnetic and influence the water molecules present in the body by disrupting the local magnetic field. The magnitude of this disruption is a function of the amount of contrast agent present.

Molecular oxygen, similar to gadolinium contrast agents, is paramagnetic due to the presence of two unpaired electrons. The sensor maintains a constant state of equilibrium with the surrounding tissue as oxygen diffuses in and out of the sensor. The concentration of molecular oxygen present in the sensor directly influences the relaxation time of the material. These concentration changes modify the relaxation time of the sensor. Calibration of the sensor under known oxygen conditions allows relaxation times measured during use to be mapped into the oxygen domain.

Magnetization Transfer

Magnetization transfer can occur as a result of many mechanisms including the binding of water molecules to solutes or macromolecules, dipole interactions, and chemical exchange.⁵ Protons present on macromolecules (natural and synthetic) have relatively short relaxation times ($\sim\mu\text{s}$) compared to protons present on free water molecules ($\sim\text{s}$). Certain hydrogen-containing bonds serve as efficient sources of transferable protons, including NH and OH.^{6,7} Bound protons effectively reduce the relaxation time of the free water protons due to the magnetization transfer between the polymer and free water molecules (*Figure 8*). This mechanism enables pH measurements because the rate of exchange, and thus the influence on relaxation time, is acid- and base-catalyzed, with the slowest exchange generally occurring near a more neutral pH. A pH calibration curve is developed which allows measured relaxation times to be mapped into the pH domain.

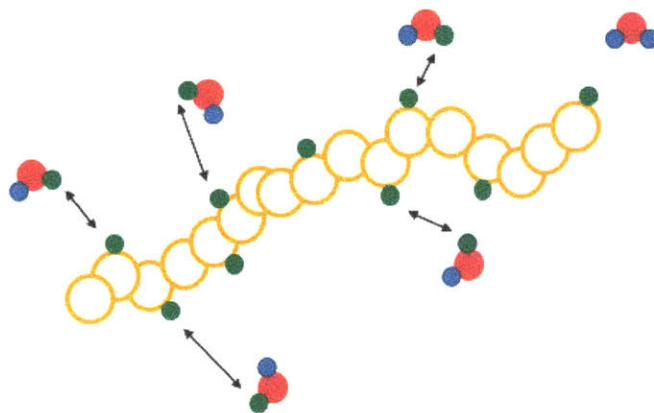


Figure 8 The exchange of protons between free water molecules and the polymer backbone produces a pH-dependent measurable signal. The exchange of protons is catalyzed in both acidic and basic environments.

Page Intentionally Left Blank

Chapter 2: *In Vivo* Oxygen Sensor in Cervical Cancer

Background

There were 13,240 new cases of cervical cancer and 4,170 cervical cancer deaths in 2018 in the US.⁸ The occurrence rate of cervical cancer has decreased dramatically with the use of Pap testing and the detection of pre-cancerous lesions. This significant progress in detection has not been ubiquitous, and it remains the leading cause of cancer in women who did not receive regular screenings. There were 530,000 new cases of cervical cancer and 270,000 cervical cancer deaths worldwide in 2012.⁹ Ninety percent of these deaths occurred in the developing world.¹⁰ Almost all cervical cancers are associated with HPV infection, highlighting the role of vaccination efforts against strains known to increase the likelihood of cervical cancer.¹¹

The frontline treatment for patients diagnosed with locally advanced cervical cancer is a combination of EBRT (external beam radiation therapy), sensitizing chemotherapy, and brachytherapy.¹² EBRT is typically delivered daily, five days per week, for five weeks. Chemotherapy (cisplatin) is delivered concurrently, starting the first day of radiotherapy, and is continued in weekly bolus doses. Concurrent chemotherapy has been shown to serve as a radiosensitizer, improving overall survival in patients by 5%.¹² Patients are also treated with radiation dose-boosts utilizing high dose-rate brachytherapy. This enables higher doses to subsets of the tumor volume while respecting dose limits to surrounding healthy tissue and organs.

The Role of Oxygen in Oncology

The important role of oxygen in oncology treatment has been well characterized in a wide range of cancers. Tumors are generally understood to be hypoxic, characterized by an extreme lack of oxygen.^{13,14} This is attributed to the disrupted vasculature in tumors and the oxygen demands of growing tumors.¹² Tumor hypoxia varies both spatially and temporally.^{15,16} Designation of a tumor as hypoxic is typically based on a median PO_2 (oxygen partial pressure) below a certain threshold or percentage (hypoxic fraction) of

spatially disparate measurements below a certain level. The cutoff to designate a tumor as hypoxic is often specific to a given study.

The challenges associated with treating hypoxic tumors have been well-characterized. These have been observed in bladder, cervical, head and neck, prostate, and renal cancers. The oxygen state of the tumor, in many cases, imparts distinct outcomes. Hypoxia is an independent prognostic indicator for disease-free survival in patients with cervical cancer. Hypoxia also predicts tumor spread beyond the cervix and resistance to radiation. Cervical cancer patients with hypoxic tumors were found to have a lower five-year survival rate than patients with more well-oxygenated tumors.¹⁷⁻¹⁹ Hypoxia has also been found to be an important and independent predictive clinical tool in patients with prostate cancer. Tumor oxygen content, in these cases, has been shown to predict the likelihood of relapse following radiotherapy.¹⁸

Cervical tumors, as is the case with many solid tumors, are oxygen depleted.¹⁷ The difference in oxygen content of tumors vs. co-located healthy tissue is significant. Measured median tumor oxygen levels in cervical cancer patients was 5.0 mmHg compared to 51 mmHg in healthy tissue.²¹ In prostate cancer, a similar trend was observed, where the median tumor oxygen level was 2.4 mmHg compared to healthy tissue which had an oxygen level of 30.0 mmHg.²² This trend has also been observed in head and neck, lung, and pancreatic cancers.²³⁻²⁶ Hypoxic tumors or tumor sub-volumes impart many challenges on patient treatment. These difficult-to-treat tumors cause patients with hypoxia to generally have worse clinical outcomes.²⁷⁻³¹ Hypoxia induces metastasis formation, transition to more aggressive cell phenotypes, and resistance to chemo- and radiation therapy.^{17,28,32,33} Tumor hypoxia varies spatially and temporally, making characterization of tumor hypoxia a complicated and potentially longitudinal process. The resistance to treatment manifests itself in drastically different treatment outcomes (Figure 9).³⁴⁻³⁷

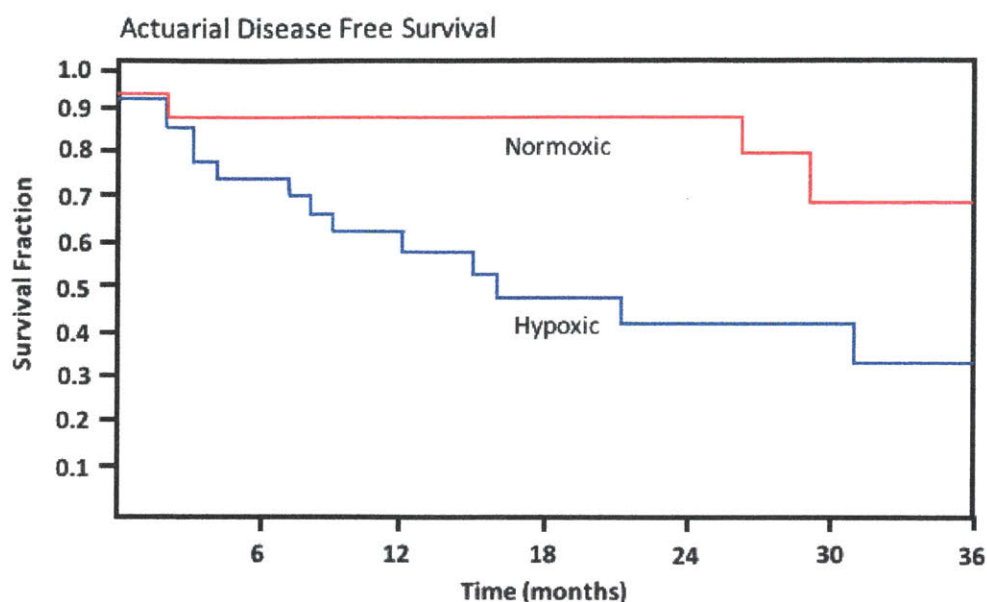


Figure 9 Patients with hypoxic tumors suffer a 30% lower survival rate at three years compared to patients with more well-oxygenated tumors. Tumor hypoxia is characterized by hypoxic fraction, the percentage of measurements made with a pO₂ below 5 mmHg. Reprinted from *Radiotherapy and Oncology*, Volume 53, Issue 8, Knocke, T. H., Weitmann, H. D., Feldmann, H. J., Selzer, E. & Pötter, R. Intratumoral pO₂-measurements as predictive assay in the treatment of carcinoma of the uterine cervix, 99-104 (1999), with permission from Elsevier.

The survival rate of cervical cancer patients with a hypoxic tumor is 40%, compared to 70% for patients with a more well-oxygenated tumor. Pre-treatment tumor oxygen state was determined to be an independent predictive indicator of treatment outcomes in a study of prostate cancer patients.

Overcoming Hypoxia-Induced Resistance

Efforts to address the challenges of hypoxic tumors have focused on the development of new therapeutics²⁰ and radiation therapy dose escalation among other techniques. These treatments are of limited clinical value without a means to stratify the patient population based on tumor oxygen content before starting treatment. The focus of the work in this dissertation is related to radiation therapy dose escalation, but the sensor could be applied to other treatment approaches.

The pathway of a cell exposed to ionizing radiation is a function of the environmental oxygen content. Radiation therapy delivered in the presence of oxygen proceeds down a path of irreversible damage that leads to cell death. In low-oxygen (hypoxic) environments, cells exposed to radiation therapy can recover and avoid cell death. This is the fundamental source of radiotherapy resistance. Oxygen level-independent cell death can be achieved by altering the radiation dose delivered. Increased dose levels in hypoxic environments can achieve an equivalent outcome to lower doses in more well-oxygenated environments (Figure 10).³⁸

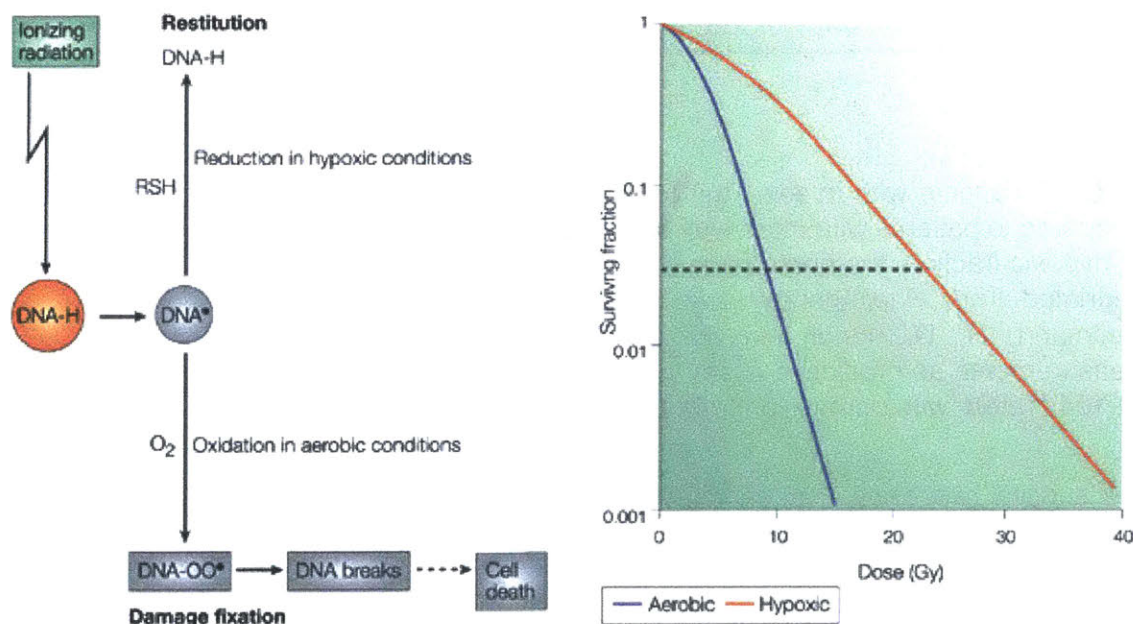


Figure 10 Comparison of survival fraction for cells irradiated in different oxygen environments. Reprinted by permission from Springer Nature: Nature Reviews Cancer, Brown, J. M. & Wilson, W. R. Exploiting tumour hypoxia in cancer treatment. *Nat Rev Cancer* 4, 437-447, doi:10.1038/nrc1367 (2004).

This principle has been expanded to explore clinical use with radiobiological modeling in prostate cancer (Figure 11).³⁹ This analysis shows similar trends that increased dose can overcome hypoxia-induced radiation therapy resistance.

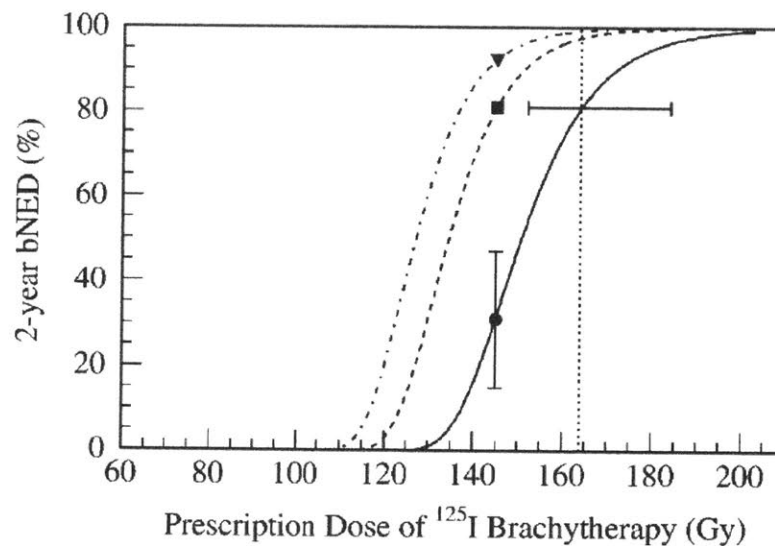


Figure 11 Radio-biological modeling supporting dose escalation for hypoxic tumors. Well oxygenated (.-), normal oxygen levels (--) and hypoxic (solid).⁴⁰

High Dose-Rate Brachytherapy

Some forms of radiation therapy provide easier and more direct means of achieving dose escalation. HDR-brachy (high dose-rate brachy therapy) is a form of radiation therapy where the radioactive source is placed directly in or within close proximity to the tumor. This method often uses a plug of Iridium-192 attached to a wire.⁹ The radioactive source is placed in rigid catheters distributed throughout the tumor. The wire allows a remote loading system to precisely position the source anywhere within the catheter for a pre-determined duration. The position and duration of the catheters and the source within them is based on an in-depth and highly technical process of treatment planning. There are three primary forms of HDR-brachy: intracavitary, interstitial, and hybrid. Intracavitary is the most common form of HDR-brachy for cervical cancer, and involves placement of the source near the tumor but not directly in the tissue.⁴¹ Interstitial brachytherapy is used in cases where high doses delivered directly to the tumor are required. The hybrid approach combines both intracavitary and interstitial brachytherapy.

Image-guided High Dose Rate Brachytherapy

Patients undergoing HDR-brachy often have imaging sessions to characterize the tumor and its proximity to healthy tissue and organs,⁴⁰ as well as to determine catheter positioning. Imaging helps to optimize placement of the catheters and define dose distribution. Varying types of image guidance are employed. The primary limiting factor in determining the type and quality of imaging is the availability of specific modalities at the treatment facility.

Real-time MRI-guided implantation, as opposed to imaging post-implantation, is the preferred method of catheter insertion as catheter position can be adjusted in real-time.⁴² This typically involves a cyclic process of scanning and adjustment of catheter position following an initial round of catheter placement. The initial round of placement is often conducted under ultrasound guidance. Real-time imaging is not always possible and sometimes a scan is conducted at the end of the implantation process, and before treatment starts, to characterize the position of the catheters. CT (computed tomography) is a less preferred method of imaging because it doesn't offer the same resolution and soft tissue contrast as MRI.⁹ In some cases, when no imaging modality is available, clinicians are forced to implant catheters without any imaging-based feedback. Distribution of catheters throughout the tumor is important to enable dose distribution and avoid concentrating an excessive dose in one location. The catheter implantation process is often involved, sometimes taking hours. This, in combination with the complications of treatment planning, means that the catheters will often remain in place throughout the duration of treatment, which often includes multiple fractions (multiple delivery sessions) over 2-3 days.

Dose Delivery

Treatment delivery is an automated process. The hollow catheters are attached to a remote afterloader which places the radioactive source into specific locations within each catheter for specific durations. The remote afterloader is disconnected between fractions and the patient is allowed to rest. Fractions are typically spaced at least six hours apart.

The duration of radioactive source dwell time within each position is determined based on the desired dose distribution. Dose can be modified by increasing the dwell time to deliver higher doses. No information about oxygen content is currently included in the dose planning process.

Existing Oxygen-Sensing Methods

There are many methods being used and researched for sensing oxygen in humans. The capabilities of these methods are diverse. Actionable oxygen measurements must be quantitative, repeatable, and compatible with the existing clinical work flow. Existing alternatives do not meet these requirements.

Much of the historical data highlighting the important role that hypoxia plays in cancer treatments was collected with the Eppendorf Oxygen Electrode.^{21,23} This technology provided quantitative oxygen measurements, but suffered from many limitations and is no longer widely used. The fundamental method of measurement required oxygen consumption, causing prolonged measurements to artificially reduce tissue oxygen content further, distorting the underlying tumor oxygen measurement. The probe only allowed a single point measurement, which overlooked the importance of the heterogeneity of hypoxia. Efforts to overcome this involve step-wise measurements of the tumor along multiple needle tracks, but this isn't practical for long-term measurements.

Fiber-optic probes have since become the focus of probe-based measurements. These probes do not suffer from the same issues with local consumption of oxygen challenges, but still only provide a single point measurement. They are also more fragile and can break easily. They are not currently available for clinical use.

The focus, more recently, has shifted to imaging-based methods utilizing endogenous and exogenous markers to characterize tumor hypoxia. HIF-1 α ,^{48,49} a transcription factor that regulates the response to hypoxia has been shown to not correlate with tumor hypoxia.^{9,43} This makes it difficult to use as tool for mapping tumor oxygen content.

The leading and most widely accepted method of tumor hypoxia characterization is PET/CT^{44,45} (positron emission tomography/computed tomography), utilizing the exogenous markers FDG (fluorodeoxyglucose) or FMISO (fluoromisonidazole). This method is fundamentally limited by the relatively low resolution of clinical PET/CT (4-8 mm) and the inability to directly measure tissue oxygen levels (PO_2). There is also a lag-time of up to two hours between injection and measurement, making measurement of acute (hourly fluctuations)⁴⁶ temporal changes in hypoxia more difficult. MRI-based methods can be appealing due to their comparatively easy integration with the existing clinical workflow. Qualitative methods (blood oxygen level dependent or dynamic contrast enhanced MRI) rely on the presence of blood flow, which is often inconsistent and disrupted. Quantitative methods (fluorine MRI) require different MRI hardware, which is not widely available, and multiple scans to obtain both oxygen information and physiological structure. The need for multiple scans may lead to motion artifacts which would diminish the spatial value of the oxygen measurement.

Silicone Oxygen Sensors using H^1 Magnetic Resonance Imaging

The relaxation time of silicone is a function of the concentration of the dissolved oxygen in the material. This phenomenon can be attributed to the paramagnetic nature of molecular oxygen. Molecular oxygen has a similar influence on the relaxation time of protons as do gadolinium contrast agents which are also paramagnetic. The chemical structure of silicone limits the ingress of biological materials, enabling accurate measurement of the silicone that is primarily dependent on the dissolved oxygen concentration. Liquid silicones oils are generally more sensitive in detecting oxygen changes than elastomeric silicone. Low molecular weight silicones have been reported for this purpose, but their use is limited because they diffuse away from tissue injection sites with a half-life of about 35 hours.⁴⁷ This necessitates re-injection for longitudinal tissue oxygen tracking. Elastomeric silicones, while less sensitive, remain at the site of injection for extended periods enabling repeated measurements.

The Cima Lab has developed an oxygen-sensitive silicone material that combines the high sensitivity of silicone oils and the locational stability of elastomeric silicone by swelling the elastomer with silicone oil during curing. This silicone formulation mechanically entraps the silicone oil and limits its diffusion away from the site of injection. The elastomeric nature of the silicone also enables production in a wide range of formats including microparticles, coatings, and disks (Figure 12).

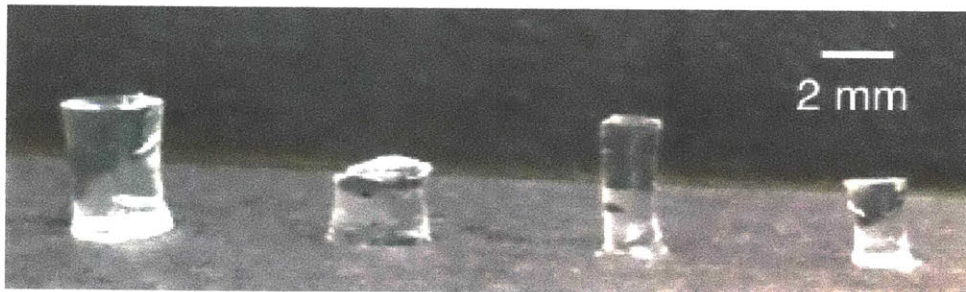


Figure 12 Examples of silicone oxygen sensors. The silicone sensor can be produced in multiple formats and shapes due to the elastomeric matrix.

The relaxation time of the silicone measured with H^1 MRI can be converted to a partial pressure based on a pre-existing, application-independent, calibration curve (Figure 13). The curve is developed by measuring the relaxation time of the silicone in known oxygen concentrations. The calibration curve is, however, a function of the silicone formulation and the specific silicone oil selected.

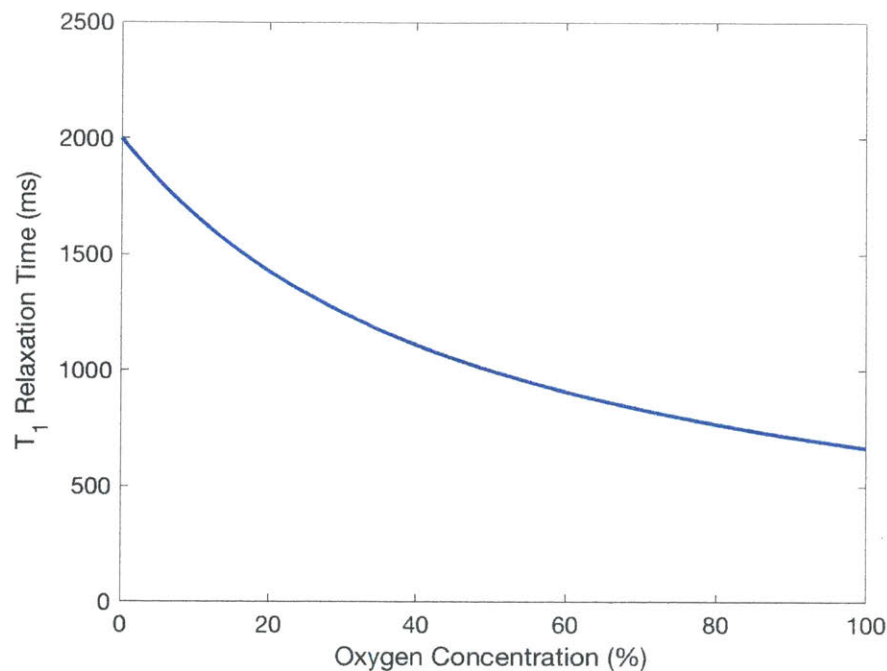


Figure 13 The theoretical relationship between the T_1 relaxation time and oxygen concentration. The relaxation time of the sensor is greatest when no oxygen is present and decreases as the concentration of oxygen increases.

Improvements to the Clinical Work Flow

There is a wealth of data supporting the disparity in outcomes between patients with well-oxygenated and poorly-oxygenated tumors. The concept of increasing radiation dose to achieve a higher rate of cell death in hypoxic regions is also well established. HDR-brachytherapy provides a safe and practical means to selectively increase dose in poorly oxygenated tumor sub-volumes. This method is unique in the ability to hyper-locate the elevated dose without unnecessarily exposing healthy tissues and organs to the increased dose. The lack of a viable, quantitative, oxygen measurement method that is MRI compatible has greatly hindered addressing this unmet clinical need.

The silicone-based oxygen-sensitive materials developed by the Cima Lab provide an ideal means to make the necessary quantitative oxygen measurements. Clinicians prefer MRI-guided placement of treatment catheters because of the higher quality scans (better

soft tissue contrast and enhanced spatial resolution) as compared to other imaging modalities. Integration with this clinical work flow necessitates, at a minimum, MRI compatibility. The silicone material is not only MRI compatible, but is measured using MRI, avoiding the need for new hardware to be introduced into the operating room. Oxygen measurement and tissue structure can be obtained on the same scan, enabling an understanding of oxygen levels throughout the tumor. The polymeric nature of the material allows one or more depots to be implanted with fine location control. This can be done at the beginning of treatment and will remain in place throughout the duration of treatment (or longer). This becomes particularly useful in cases when multiple brachytherapy fractions are delivered (e.g. cervical cancer). Each brachytherapy fraction provides an opportunity to optimize dose, and an oxygen measurement would be part of the decision making and treatment planning process. The silicone can also be implanted permanently, depending on the specifics of the embodiment employed for deployment, allowing clinicians to track tissue oxygen during recovery.

Early Feasibility Clinical Trial – Cervical Cancer

The work in this chapter is in support of an early feasibility clinical trial to evaluate the performance of the oxygen-sensitive silicone polymer. The FDA defines an early feasibility trial as “a limited clinical investigation of a device early in development, typically before the device design has been finalized.” These trials are conducted with a limited number of patients to evaluate device design for initial clinical safety and device functionality. These results are often used to guide device modifications before submission to the FDA for approval.

This trial will focus on patients with pathologically-confirmed cases of cervical cancer who are undergoing HDR-brachy. Patients will be enrolled at Brigham and Women’s Hospital and the procedure will occur in the Advanced Multimodality Image Guided Operating Suite. The study will enroll ten patients and involve placing 2-4 oxygen sensors per patient. The device for this trial has been designated a non-significant risk by the Dana Farber IRB (Institutional Review Board). Designations of non-significant risk do not

necessitate trial approval by the FDA, but rather just that of the governing IRB(s). This clinical trial has also been approved by the IRB at the Massachusetts Institute of Technology.

Deviations from the existing clinical practice require approval from the IRB. The IRB has approved a period of 120 minutes for the sensor to equilibrate post-insertion. The oxygen sensors are inserted prior to the placement of the treatment catheters, allowing the silicone to equilibrate with the tissue environment during treatment catheter insertion. MRI scans are already conducted as part of the normal clinical practice, but the IRB has approved an additional 30 minutes of scan time to collect the data necessary to make the oxygen measurement. The sensors will then be removed and the treatment protocol will proceed following existing clinical practice.

The study's primary endpoint is the safe placement and removal of the oxygen sensor and measurement of the oxygen sensor T_1 relaxation time within the constraints of the existing clinical workflow. Secondary endpoints will evaluate patient response through 6-month PET/CT scans which are already part of normal clinical practice. The scans are used to track response and recurrence and, for this study, will be used to investigate whether a correlation exists between patients with lower tumor oxygen levels and poor clinical outcomes in cervical cancer.

Oxygen Sensor Design and Deployment

The design of the sensor for this early feasibility clinical trial has unique constraints that will not apply to the next generation embodiment. The sensor for the early feasibility trial was produced by modifying an existing brachytherapy treatment catheter to incorporate the oxygen-sensitive silicone (Figure 14).

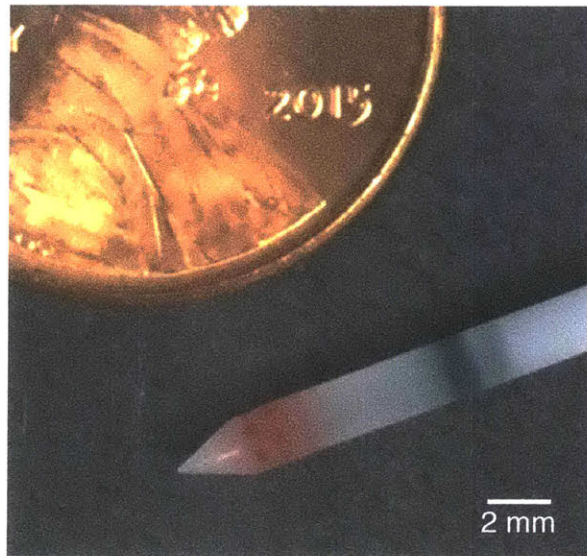


Figure 14 A modified version of the existing brachytherapy treatment catheter that incorporates the oxygen-sensing silicone.

The brachytherapy treatment catheter is made from polyoxymethylene, a rigid polymer that has low oxygen permeability. Placement of the oxygen-sensitive silicone in the catheter requires a method to enable the efficient exchange of gases between the tissue and the inside of the catheter. Oxygen exchange was achieved by machining holes into a portion of the distal end of the catheter that will be placed in the tumor. The catheter containing the silicone will be used for oxygen measurement only and not for treatment.

The design for the early feasibility trial has two rows of six holes each (Figure 15). This design configuration was selected to provide sufficient mechanical strength while meeting the performance requirements for this study. The rows are rotated 30 degrees relative to each other to maximize the distance between holes. The rows are vertically spaced 0.77 mm on center. The hole diameter is 0.51 mm. The bottom of the catheter is filled with 7 mm of oxygen-sensitive silicone and then capped with a 1 mm tall polyoxymethylene plug and sealed with a 1mm thick layer of light cure acrylic epoxy.

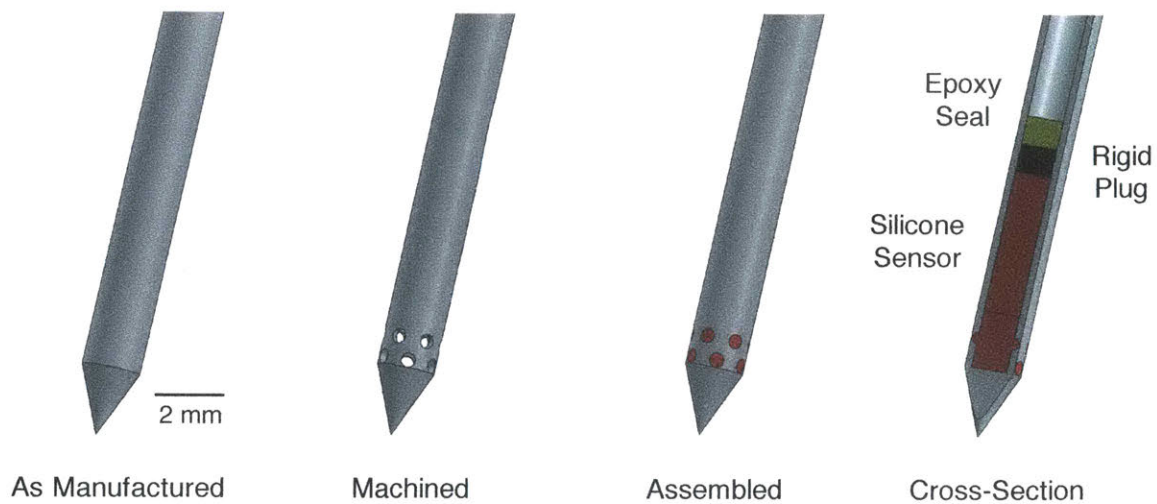


Figure 15 A cross-section of the oxygen sensor catheter. The red layer is a higher viscosity silicone that is used to plug the holes for oxygen diffusion. The blue layer is a more oxygen-sensitive silicone blend. The black layer is a Delrin plug. The yellow layer is a light cure acrylic epoxy to seal the silicone from the ambient oxygen in the lumen of the catheter.

The design decision to incorporate the silicone material in the brachytherapy catheter was driven by the desire to create a device that mimics those already used during the existing brachytherapy procedure. This format will integrate well with the current clinical work flow and minimize changes for the clinician.

The oxygen sensor catheters will be inserted in the same manner as the treatment catheters using the same equipment (Figure 16). A rigid metal stylet will be placed in the inner lumen of the catheter during insertion to improve rigidity and then removed when the catheter has been fully placed in the tissue. The oxygen sensor catheters will be removed before treatment proceeds and their location may subsequently be used for treatment catheters. No clinical decisions will be made based on the oxygen measurements collected during this trial. This trial will be used to inform the design and define the necessary capabilities of the next generation sensor.

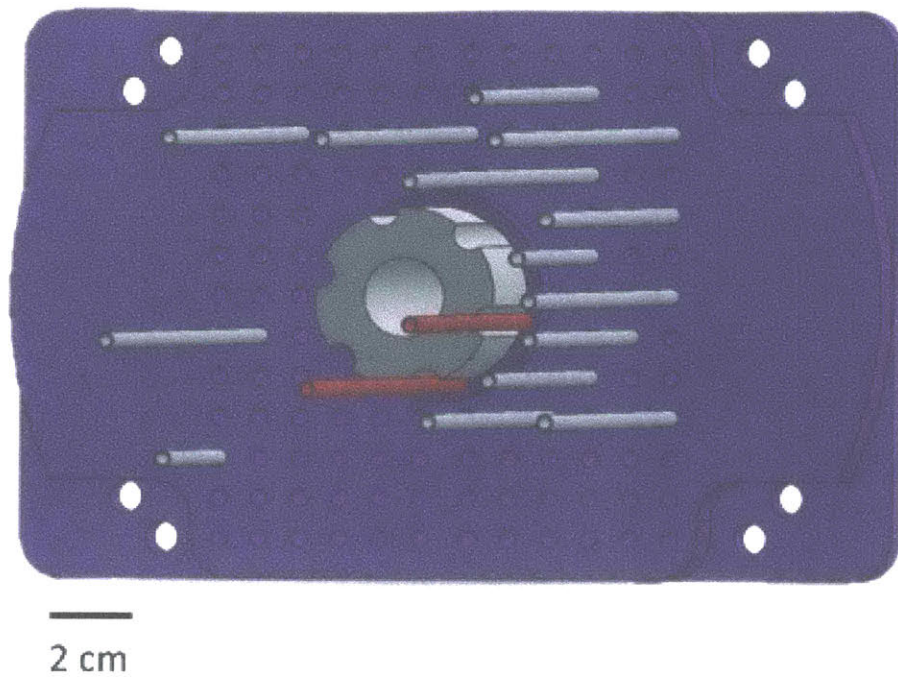


Figure 16 The purple template is used to define the position of catheters during the treatment planning process. The red catheters denote the oxygen-sensing catheters. The oxygen-sensing catheters will be inserted along the obturator. These catheters may be removed after the measurement and replaced with treatment catheters during the study.

The design constraints for this generation of the sensor are outlined in Table 1. Key considerations and constraints are the safe insertion, measurement and removal of the sensor, the rate of sensor equilibration to the tumor environment, and data acquisition time. Many of these design considerations are not completely independent because a single design decision impacts multiple performance characteristics. This will not be the case with subsequent iterations of the sensor, but must be considered for this generation.

Table 1 Design constraints and the implications of each constraint.

| Property | Limitations | Design Implications |
|---------------------|---|--|
| Materials Selection | Design for implantable medical use | Type of silicone |
| Acquisition Time | 30 min | MRI acquisition parameters, amount of silicone |
| Equilibration Time | 120 min | Amount of silicone, insertion vehicle |
| Sensor Resolution | Distinguish between 21% and 0% O ₂ | Amount of silicone, MRI acquisition parameters |
| Mechanical | Safe insertion and removal | Amount and type of silicone, insertion vehicle |

The first design decision is focused on the formulation of the silicone. It impacts sensor resolution and mechanical performance. Sensor resolution is dictated by the ability to distinguish between vanishingly close oxygen levels. There are multiple factors that contribute to sensor resolution including MRI settings, acquisition time, and liquid silicone viscosity. The resolution requirement for the early feasibility trial is to distinguish between environments with 0% and 21% oxygen. Sensor resolution is defined as the change in relaxation time vs. the change in oxygen content. The difference in relaxation time at 0% and 21% oxygen is used as a metric to compare different silicone formulations. Silicone sensors produced using short chain length silicone oils (which correspond to lower viscosity silicones) have a larger difference between 0% and 21% oxygen than longer chain length silicone oils (Figure 19).⁵⁰ Absent other considerations, these may be the preferred materials for the oxygen sensor.

Biocompatibility data provided by the silicone manufacturers (Nusil) supports the use of these silicone oils for different applications based on their viscosity. Existing biocompatibility data on individual materials does not absolve one of the responsibility to conduct biocompatibility testing on the final device, but that data can be used to select materials with a greater chance of successfully passing those tests. This consideration leads to the selection of a silicone oil with moderate chain length that has a viscosity of

100 cSt (Figure 17). This material is intended for implantable use by the manufacturer. Materials with shorter chain lengths are currently intended for topical applications and their use for implantable devices will require more extensive testing.

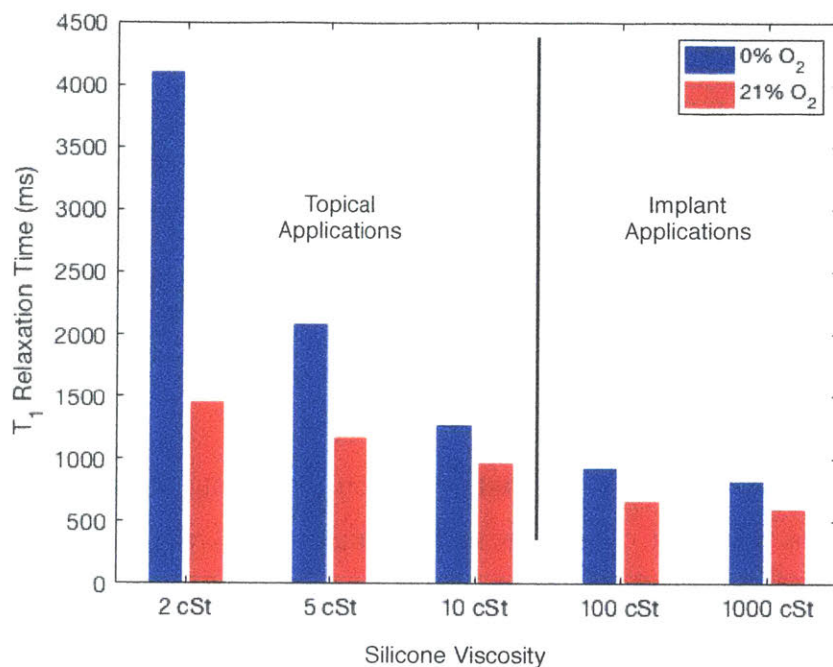


Figure 17 Compares the relaxation time of silicone oils with a range of viscosities under conditions of 0% and 21% oxygen. Data collected using Bruker Minispec (0.5 T).

Independent of the silicone oil selection, an increase in the total volume of silicone can increase the SNR (signal-to-noise ratio) which improves sensor resolution. Increased silicone volume is not without its drawbacks. It decreases the equilibration rate (assuming a constant number and size of the holes) and reduces the failure force, both of which are further discussed later in this chapter. This highlights the interconnected nature of the design decisions for this generation of the sensor. This is further elucidated by the impact that hole number, size, and position have on sensor performance (equilibration rate and mechanical properties).

The analysis of sensor performance is presented in the subsequent Results section. The design decisions were evaluated in totality to ensure a safe and functional device that

meets the requirements necessary for use in this clinical trial. These design constraints will be decoupled during the design of subsequent versions of the sensor. Future embodiments of the sensor are outlined at the end of this chapter.

Results

The work in this chapter focused on incorporating the silicone material into a format for a pilot human clinical trial. The sensor design was evaluated for three primary criteria: sensitivity, equilibration rate, and mechanical strength. The work presented also includes optimization of MRI parameters to ensure efficient and accurate sensor measurement within the time constraints approved by the IRB.

MRI Data Collection

Translation to a clinical MRI requires determination of the pulse sequence and MRI parameters that will allow for consistent and accurate measurement of the sensor in humans. An MRI phantom (Figure 18) was fabricated to mimic *in vivo* conditions while simultaneously allowing the sensor to be exposed to different concentrations of oxygen.

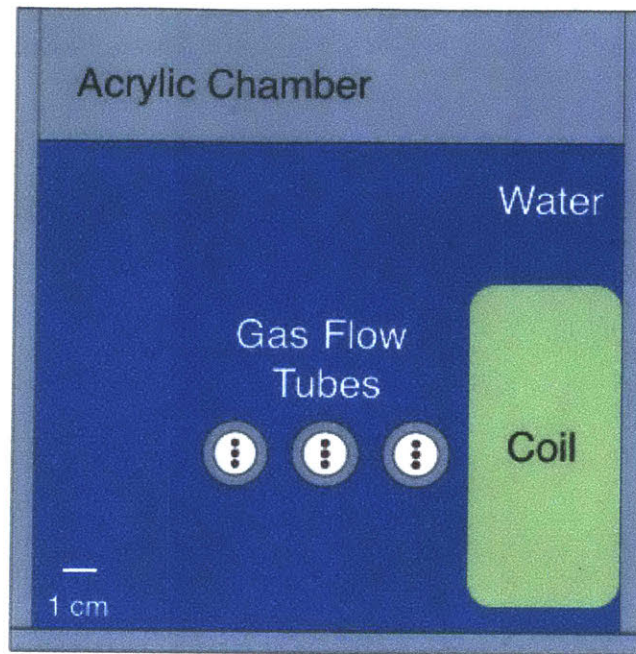


Figure 18 A schematic of the MRI phantom. The MRI phantom has three separate tubes for gas exposure. The phantom is filled with water to mimic human tissue. The tubes are positioned relative to the endorectal coil such that they span the range of distances from the coil expected *in vivo*. The spin coil is under the phantom and the body-matrix coil is placed on top of the phantom.

The phantom is designed to accommodate the endorectal and the body-matrix receive coils, two options to improve the signal quality of the data collected. The phantom enables catheters to be positioned in three tubes spaced 1 cm, 3.5 cm, and 6 cm from the endorectal coil. These positions span the range of distance from the coil expected *in vivo*. Extra focus is given to the two closest tubes because catheters are expected to be positioned within 3.5 cm of the endorectal coil during clinical use. The body-matrix coil is placed on top of the phantom in a manner similar to how it would be oriented on top of the patient during clinical use (Figure 19). A cross-section through the phantom is used to collect intensity data for the relaxation time measurement (Figure 20).



Figure 19 The MRI phantom with the endorectal coil inside the phantom and the body-matrix coil placed on top of the phantom. The spin coil is in the bed of the MRI.

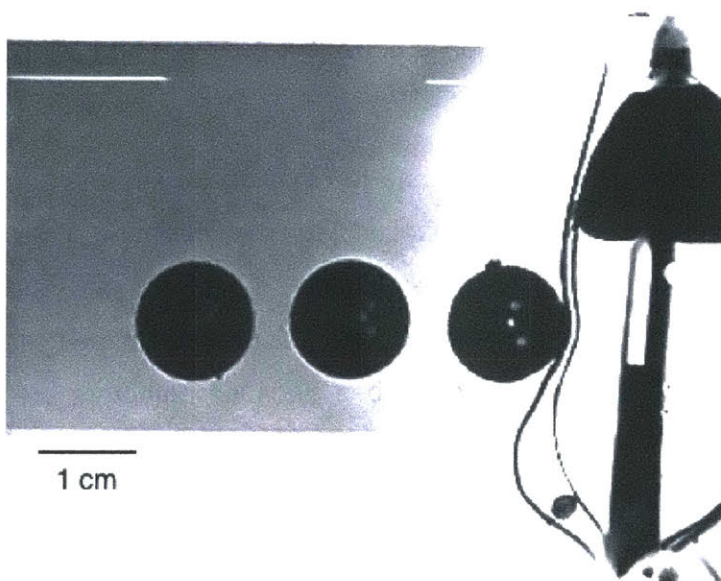


Figure 20 MRI scan of the phantom. The endorectal coil is positioned at the far left. Three tubes containing catheters are shown spaced evenly across the phantom. Each tube can have the environmental oxygen concentration modified in real-time to test the kinetic response of the catheter to changes in oxygen concentration. Folding of the scan can be seen in the lower portion of the scan represented by the brighter white band. Accurate measurement of the catheters requires that they be outside the folding region.

MRI Parameter Selection

Optimization of MRI parameters and settings can be extensive and many permutations exist. This work focused on the key parameters of receive coil selection, slice thickness, repetition time (TR), and inversion time selection.

Clinical MRIs have distinct coils for excitation and measurement (receive). Excitation coils are generally fixed in their position and are located around the bore of the magnet. The options for the receive coil are far greater and are often specific to the anatomy being imaged. Options include coils in the bed of the scanner or ones that are placed on the patient (body-matrix or around specific body parts of interest) or in the patient (vaginal or endorectal) (Figure 21). The work presented evaluates the use of the spine, endorectal, and body-matrix coils for measuring the oxygen sensor in the phantom.

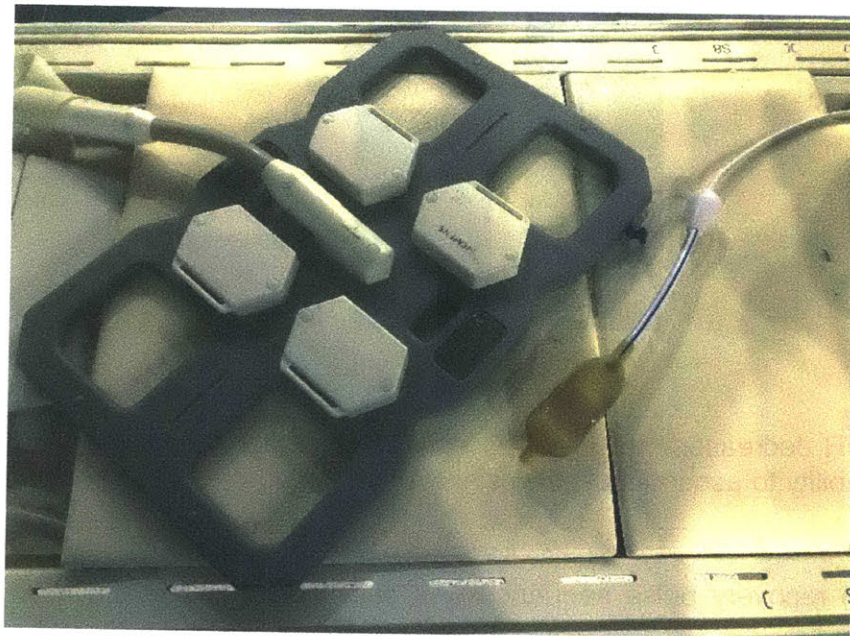


Figure 21 The body-matrix (left) and endorectal (right) coils.

Measurements were made using all combinations of the three coils. The predominant source of the signal is obtained from the endorectal coil (Figure 22) due to its close proximity to the sensor. The spine coil also provides additional signal strength. The body-

matrix coil was observed to have minimal impact on the quality of the measurement. The spine coil and the body-matrix coil are considered the standard of care for the patient population, and the endorectal coil use has been approved by the Dana Farber IRB for this study. All three coils will be used during the clinical study. The body-matrix coil was included, despite the minimal impact observed with the phantom, to insure against differences between the phantom and the patient and because it is already considered part of standard clinical practice.

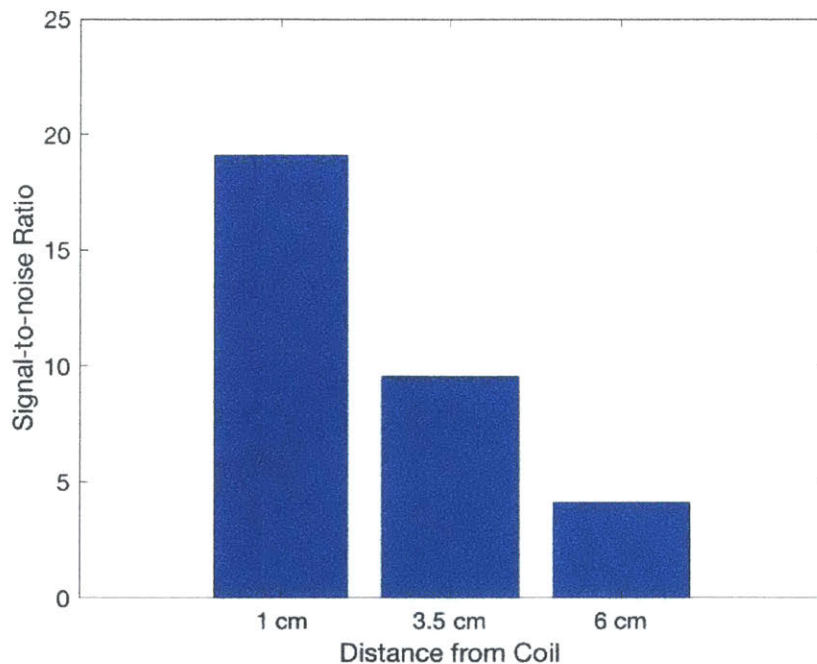


Figure 22 SNR decreases moving away from the endorectal coil. The decreased SNR reduces the ability to accurately fit the relaxation data and decreases resolution.

The inversion recovery pulse sequence was selected for data acquisition. The pulse sequence utilized has a minimum slice thickness of 2 mm. Increased slice thickness (3 mm) was also evaluated. Increasing the slice thickness by 50% would theoretically lead to a 50% increase in signal strength in a uniform system. An increase in the SNR of the sensor was not measured. This is likely due to the edge effects and the layered nature of the sensor, where movement in either direction of the ideal location by more than 1-2 mm

would lead to sampling of the rigid plastic cap or the tip of the catheter which should add minimal signal to the measurement. A slice thickness of 2 mm was selected to ensure easier slice positioning during clinical scans and to avoid confounding the signal with non-silicone materials in the catheter. The importance of slice positioning, and its influence on SNR, was highlighted when comparing slices that were shifted 2 mm from the original slice plane. This shift produced a 73% reduction in the SNR. This reinforces the importance of proper slice position. The decrease in SNR can be attributed to an increased percentage of the measurement region being occupied by a material other than the silicone in the sensor.

Measurement of a T_1 relaxation time requires multiple independent data points as outlined in the Quantitative MRI section. The repetition time is a measure of the duration between independent measurements. A repetition time that is too short may lead to incomplete relaxation between measurements, and thus distorted results. Longer repetition times increase the total scan time. It is important to determine whether the increased scan time is warranted. Repetition times of 3000 ms and 5000 ms were evaluated (Figure 23). Data collected with each of these repetition times had equivalent results (relaxation time and amplitude). This equivalency allows the shorter repetition time to be used which reduces the total acquisition time.

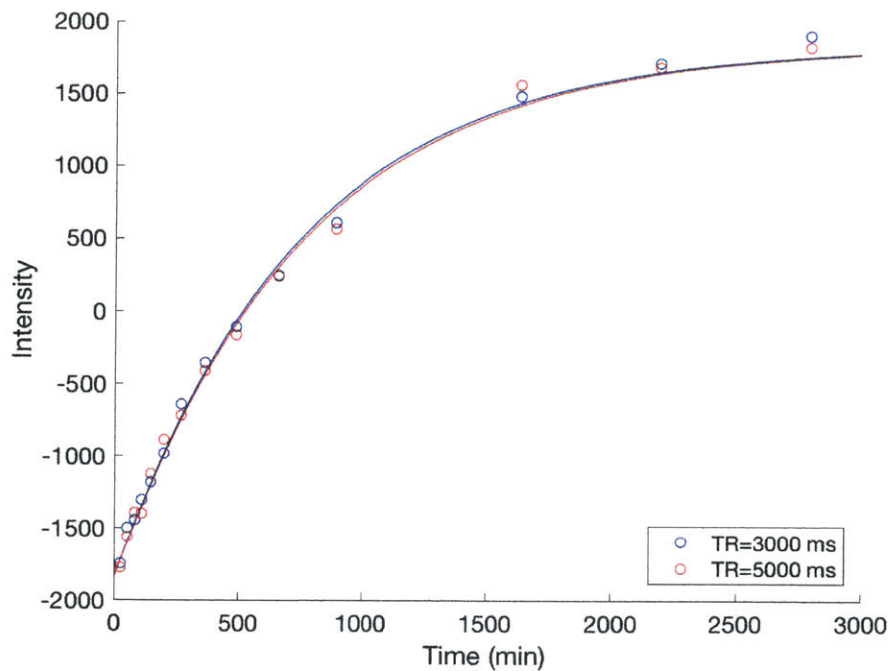


Figure 23 Data collected with TR=3000 ms and TR=5000 ms have equivalent relaxation times and amplitudes indicating that the shorter relaxation time is suitable for clinical use.

The IRB approved a 30-minute data acquisition window for each patient during the clinical trial. Each inversion takes 1.5 minutes (TR=3000 ms). Initial phantom data collected intensities at fourteen inversions with two averages at each inversion (42-minute scan), a total of 28 points. The total points collected must be reduced to 20 to comply with the 30 minutes allotted by the IRB. Different combinations of inversion times were evaluated to determine which points could be removed while having minimal impact on the measured relaxation time and the ability to distinguish between measurements made under conditions of 0% and 21% oxygen. The selected inversion times are included in Table 2.

Table 2 Summary of MRI settings.

| Setting | Value |
|----------------------|--|
| Repetition Time (ms) | 3000 |
| Echo Time (ms) | 15 |
| Slice Thickness (mm) | 2 |
| Number of Inversions | 10 |
| Inversion Times (ms) | 24, 80, 146, 268, 363, 490, 663, 896, 2200, 2800 |

Equilibration

Time to equilibration is critically important for this initial clinical trial. Incorporation of the silicone oxygen-sensing material into the HDR-brachy therapy catheter required machining holes to enable oxygen diffusion. The number and position of these holes was limited to ensure the mechanical integrity of the oxygen sensor catheter. The IRB approved a period of two hours for equilibration, the period when other portions of the procedure are already taking place. The two properties that are the primary drivers of equilibration time are the silicone volume and the surface area of the exposed silicone (a function of the number and size of the holes). The sensor will start in an ambient environment (21% O₂) prior to insertion into the patient. The cervical tumor oxygen levels are expected to be less than 1-2% in the hypoxic regions. Equilibration times were characterized from 21% to 0% O₂ to ensure that the sensor could equilibrate to the maximum change in oxygen content possible *in vivo* within the allotted 120 minutes. This data was analyzed and considered in conjunction with force testing to ensure that the final design met the requirements for both equilibration and safe use.

An initial relaxation measurement was made while the catheter was exposed to a 21% oxygen environment. Repeated relaxation measurements were made immediately after exposing the catheter to a nitrogen environment (Figure 24). These measurements were made during, as well as after, the equilibration period to validate that the sensor had in fact reached equilibration.

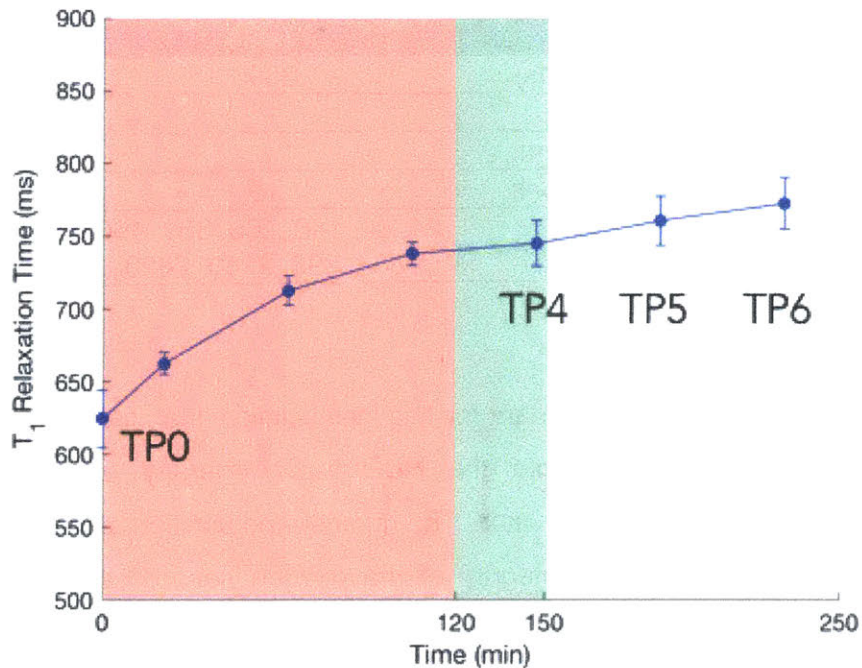


Figure 24 Shows the equilibration of catheters in response to switching from an air environment to a nitrogen environment. The point at T=0 was under an air environment. The red region denotes the time points to be collected during *in vivo* measurements. The green region denotes the data collection window. The time points represent the mid-point of the data acquisition window. The intensity values that are used to obtain a relaxation time are collected over 42 minutes. N=6 error bars represent one standard deviation. TP is used to abbreviate time point.

Analysis of these results focuses on two key areas: the duration to reach equilibration when placed in the 0% oxygen environment, and whether the relaxation times measured at 0% oxygen and 21% oxygen are statistically different. This is explored by focusing on time points TP0, TP4, TP5, and TP6 (Figure 25).

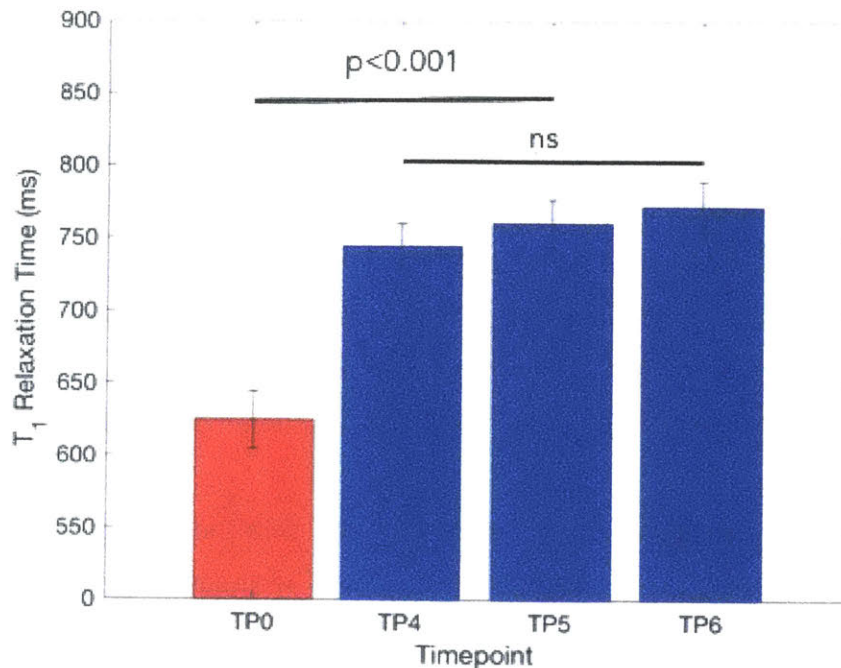


Figure 25 Shows the measured relaxation time at time point zero which was in an environment with 21% oxygen and, once equilibrated, at time point four in a 0% oxygen environment. Time point zero is significantly different from time points four, five and six ($p < 0.001$) and time points four, five and six are not significantly different. $N=6$, error bars represent a single standard deviation.

Time point four corresponds with the clinical measurement that would be made during the study. This measurement point would be completed within the 30-minute window following the 120-minute equilibration period. Time point four is not statistically different from time points five or six, which were used to confirm that the sensor had reached equilibrium at time point four. Each of time points four to six is statistically significant from time point zero which was measured under conditions of 21% oxygen. This sensor design meets the requirements for equilibration and resolution (distinguishing between 0% and 21% oxygen environments).

Mechanical Testing

Mechanical testing was conducted under multiple conditions and with two distinct test configurations. Initial measurements were made using an Instron mechanical testing

machine to enable consistent evaluation criteria and faster testing while iterating between different configurations. These tests included characterizing the insertion force into steak, a human tissue surrogate, and determining the failure force of different catheter designs. Failure force was determined by translating the catheter at a fixed rate (1 cm/s) until contacting a hard surface. Translation was continued until failure. This was characterized against surfaces of different frictional coefficients to determine the influence on failure force. A second, custom mechanical, testing configuration was used to more closely mimic the orientation of the *in vivo* use case and to allow measurement and characterization while the catheter was handled by a human operator.

The failure load of the catheter decreases linearly with increasing length (combined silicone, plug, and epoxy) of the sensor (Figure 26). The linear nature of this relationship suggests that failure mode is not a simple buckling mechanism. The buckling force of a rod can be characterized by the equation for Euler's Critical Load, which is proportional to $1/L^2$. Deviation from this relationship suggests a more complex loading configuration, likely due to the way the catheter is held during insertion. The surgeon grips the catheter around its outer circumference. This was mimicked during mechanical testing and outlined in the Methods section. This relationship between height and failure force was considered when determining the amount of silicone to add to the catheter. A device with a total height of 10.5 to 11 mm was selected.

The failure force of the catheter is independent of the coefficient of friction of the interface. Catheters were tested against surface finishes of a polished aluminum plate and the aluminum plate with 400 grit sandpaper adhered to the surface. The failure force with sandpaper followed the same linear failure force trend as the data collected when testing against the polished aluminum surface, indicating no influence based on surface finish.

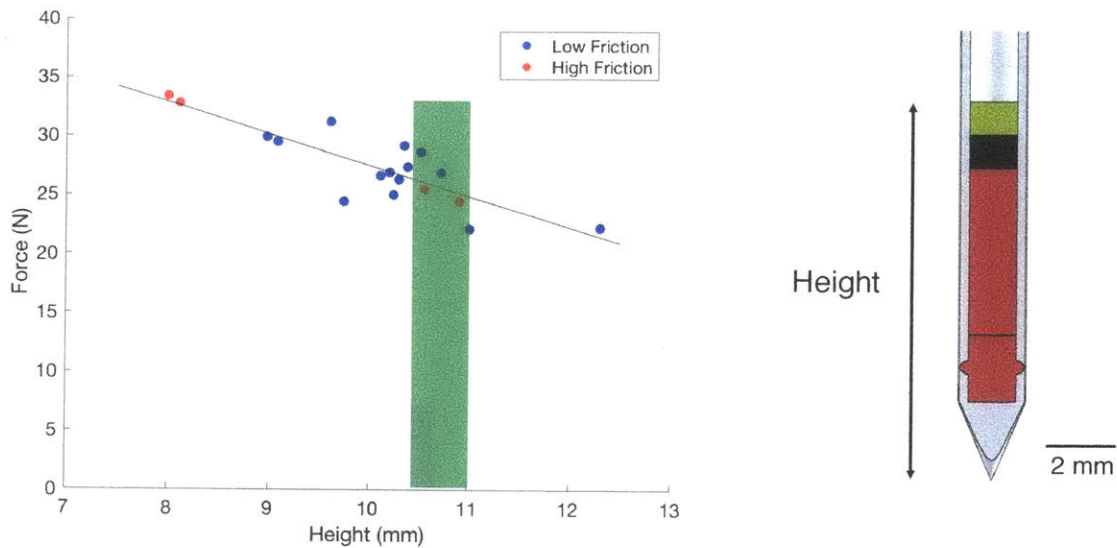


Figure 26 The relationship between failure force and catheter height is a linear relationship. The height is defined from the tip of the catheter to the top of the epoxy layer. The high friction tests were conducted against 400 grit sandpaper. Forces shown are forces at the catheter tip. The frictional force associated with contact between the catheter and the template has been subtracted from the measured force.

Catheters were then evaluated using an anatomically-oriented mechanical test system. The test fixture mimics the angle of insertion that the surgeon will experience *in vivo*. Measurements were made while a surgeon inserted along the obturator and through the template and pressed against a load sensor. Two forces are important when evaluating sensor performance: the expected use force and the force at which the surgeon would terminate use of the catheter. Ensuring a safe margin between the termination force and the failure force is critical for safe use. A water soluble medical grade lubricant was used to ease catheter insertion through the template. Insertion forces with and without lubrication were evaluated to characterize the range of forces experienced under the extremes of use. No lubrication was tested to characterize the experience of encountering a high friction surface during insertion. The average lubricated use force was determined to be 4.2 N (Figure 27). The surgeon indicated that she would cease attempting to insert the catheter if she experienced an average force of 8.7 N. The average unlubricated use force was found to be 3.8 N and the termination force was determined to be 9.7 N. The

use force and the termination force were measured with and without lubrication. With and without lubrication were found to be not statistically significant in each case.

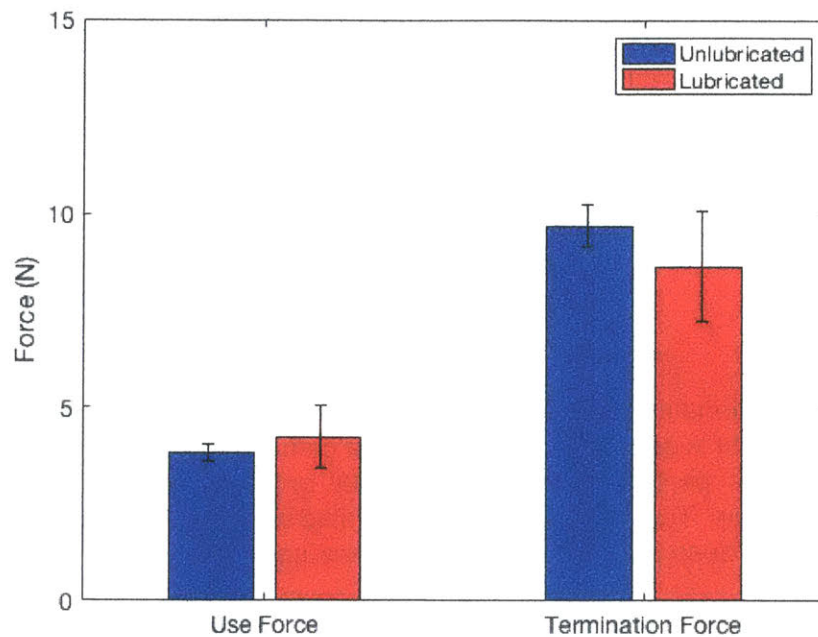


Figure 27 Catheters tested with and without lubrication showed equivalent use and termination forces. The unlubricated state represents a worst-case scenario of minimal lubrication during insertion or interference with an unlubricated surface.

The expected use force is less than 25% of the failure force and the termination force is less than 50% of the failure force measured on the Instron mechanical tester. This provides sufficient safety factors, based on clinician feedback, to ensure that this device design is appropriate for the early feasibility clinical trial.

Discussion

There is a clear clinical need for quantitative oxygen sensing to improve treatment planning and patient outcomes in cervical and other cancers. Quantitative oxygen measurements are the missing piece in providing truly customized radiation therapy. Localized dose boosting has great potential to improve outcomes and reduce relapse rates, but is greatly limited by a clinician's ability to make actionable oxygen measurements. Dose can be selectively boosted in low oxygen regions while respecting the exposure limits to healthy tissue. A design for a first-generation quantitative oxygen sensor that uses oxygen-sensitive silicone-based materials is presented. This sensor leverages the existing use of MRI in the clinical work flow and avoids the need to introduce additional hardware to the clinical workflow.

The design for the early feasibility trial meets the performance requirements and constraints of this study. The oxygen sensor catheter equilibrates within 120 minutes and the oxygen measurement can be completed within 30 minutes. It can withstand the use forces needed for safe insertion and removal of the device. This study focuses on the insertion, measurement, and removal of the sensor. The data collected and knowledge gained from this study will be used to develop the next generation sensor for broader clinical implementation.

Two additional designs for future implementation are presented. These designs are more suitable for many of the broader oncology and non-oncology applications and will allow greater resolution and sensitivity and faster scan times. Deployment of these embodiments will greatly improve the standard of care for these patient populations. These designs remove the interconnected constraints previously outlined for the current design.

Clinical Embodiment 1

Fiducial markers are small, commonly gold, seeds placed in tissue to enable cross-registration between imaging platforms and tracking of disease progression via imaging. The fiducial marker must be reliably visible on all imaging platforms of interest (primarily CT and MRI). Current fiducial markers do not provide any additional information beyond position. Incorporation of the silicone oxygen-sensing material into an existing fiducial marker or the development of a stand-alone oxygen sensor that also serves as a fiducial marker may offer many advantages over the existing alternative. Fiducial markers today are long-term implants. Incorporation of oxygen-sensing capabilities would allow long-term oxygen tracking to be conducted pre-, during, and post-treatment. Multiple fiducial markers are typically implanted which would provide a multi-site tumor oxygen map that could be re-measured serially to characterize patient progression.

Clinical Embodiment 2

The design of the oxygen-sensing catheter used during the 10-patient trial is for oxygen-sensing only and not for treatment. This is suitable for a pilot trial, but co-locating sensing and treatment may be preferred in future studies (Figure 28). This can be achieved through multiple design approaches. The oxygen-sensing silicone can be placed on the external surface of the catheter. This would greatly reduce the equilibration time by increasing the surface area to volume ratio of the silicone. It would also allow the silicone to be placed along the entire implanted length of the catheter to enable oxygen measurements along the insertion path without sensor movement. This would overcome another limitation of the previously used Eppendorf oxygen electrode. The inner lumen can be used to incorporate a stylet for insertion, radioactive treatment seed, and/or the insertion of a custom receive coil. The proximity of the receive coil to the silicone sample would greatly improve the SNR, producing higher resolution and/or reducing measurement duration. This technique also allows the voxel of interest to be pre-defined. A pre-defined voxel of interest would avoid the time associated with location of the silicone and thus further reduce scan time.

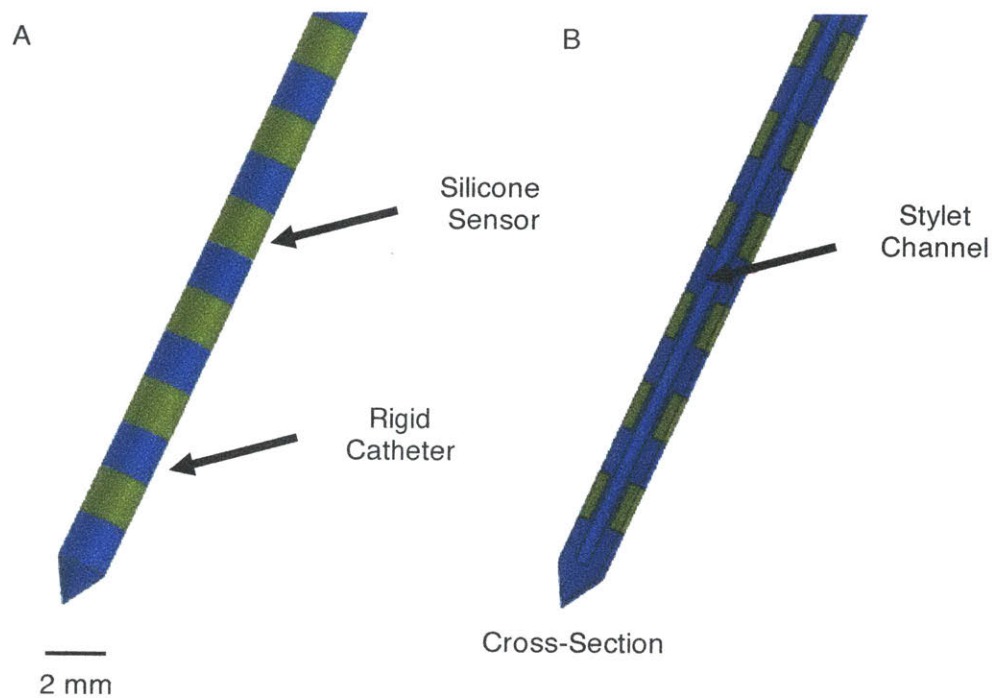


Figure 28 A) The external surface of the oxygen-sensing catheter. The oxygen-sensitive silicone is spaced discretely along the outer surface. B) The cross-section of the catheter with the inner lumen to accept the insertion stylet, reader coil, and radioactive treatment source.

Methods

Catheter Machining

The existing, as manufactured, brachytherapy catheters are machined (Cameron Micro CNC) to place 12 holes in the distal end of the catheter to enable oxygen equilibration. These holes are in two rows of six holes each. The rows are rotated by 30 degrees to maximize the distance between holes from row to row. The holes are 0.51 mm in diameter.

Silicone Mixing and Curing

The silicone portion of the sensor was produced from Nusil silicone products (formulations are outlined in Table 3). The pre-cured elastomer and silicone oils were dispensed into a mixing cup in the ratios outlined below. Silicone formulation 1 was produced in 5 g quantities and silicone formulation 2 was produced in 10 g quantities. The formulations

were mixed using a dual asymmetric centrifugal mixer (Flacktek, USA). The mixing was conducted at 2150 rpm for 30 seconds. Formulation 1 was then transferred to a syringe barrel and re-mixed (no change to the formulation, sample is already homogeneous) to degas the material following transfer to the syringe. The silicone is then transferred (tip-to-tip) to a syringe barrel for dispensing. Formulation 2 is poured into a polystyrene dish for curing. Curing is conducted at 50° C for 2 hours.

Table 3 provides an overview of the formulations of the two silicone layers.

| | Silicone Layer 1 | | Silicone Layer 2 | |
|-------------|------------------|--------------------|------------------|--------------------|
| | Components | Formulation (w/w%) | Components | Formulation (w/w%) |
| Component 1 | MED-361 | 20% | MED-361 | 70% |
| Component 2 | MED-6019 | 80% | MED-6019 | 30% |

Silicone Filling, Capping, and Sealing

The silicone is placed in the catheter in a two-step process. The bottom layer of silicone is dispensed pre-cured, and the top layer is added post cure. The bottom layer is dispensed through a 14.5" 21-gauge needle using a pneumatic dispensing system (Nordson, USA). The silicone is dispensed for 10 seconds at 70 psi. The catheter containing the silicone is placed in a curing oven at 50°C for 2 hours. The second silicone layer is then added post-cure on top of the first layer. Cylinders of the silicone formulation 2 are cored using a blunt tip 12.5" 18-gauge needle. The needle is then placed into the catheter and a stylet is used to deposit the cored silicone in the distal end of the catheter. This is repeated until the desired amount of silicone is deposited. A Delrin plug is then placed on top of the second layer of silicone and a light cure epoxy (Loctite 3944) is dispensed on top of the plug using a pneumatic dispensing system. The epoxy is dispensed for 0.25 seconds at 40 psi and with a vacuum of 18" H₂O. The epoxy is then cured using a 405 nm light source at 100% power for 2 seconds (Loctite, USA).

MRI Data Acquisition and Processing

Sensor relaxation properties were evaluated on a 3 Tesla MRI scanner (Siemens). Measurements were conducted in phantoms containing water to mimic tissue. The catheters were placed within tubes in the phantom to allow for modification of the environmental oxygen concentration. MRI data was processed using the MATLAB Curve Fitting Tool Box (MathWorks, USA). Data was fit to the inversion recovery equation.

$$M_z(t) = M_o(1 - 2e^{-t/T_1})$$

Signal-to-Noise Ratio Calculation

The signal-to-noise (SNR) ratio was calculated using the SNR calculation below. The intensity value is obtained based on the M_o parameter from the inversion recovery fit. The standard deviation of the noise is obtained by selecting a 25-voxel region where there is no sample, phantom, or water.

$$SNR = \frac{M_o}{\text{Stdev}(\text{noise})}$$

Voxel Selection Process

A plane (Figure 29) is defined to measure a cross-section through the catheter.

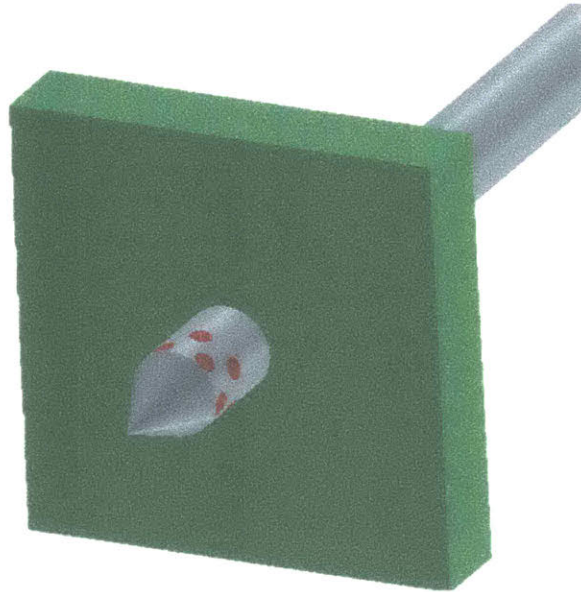


Figure 29 The cross-section plane through the catheter.

Voxels of interest were determined by defining an initial region of interest (ROI) that encompassed the sensor and surrounding voxels corresponding with air (Figure 30). Each voxel was fit separately and the SNR was determined on a voxel-by-voxel basis. A weighted average (based on SNR) of each inversion time was then calculated.

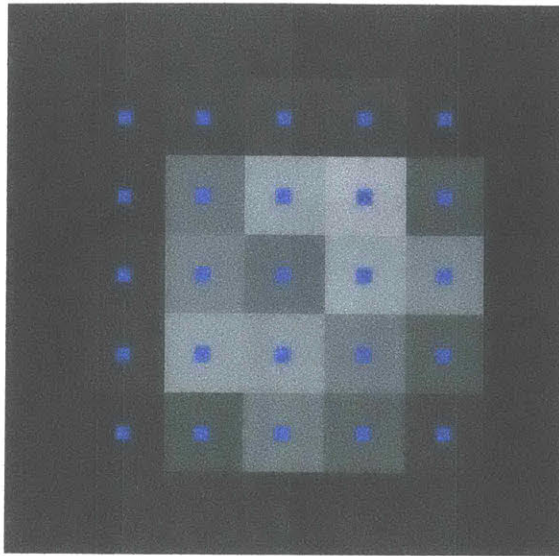


Figure 30 An MRI scan of the catheter containing the silicone oxygen sensor. Scan shows a 2 mm slice. Each voxel is 0.41 mm x 0.41 mm x 2 mm. A 5 by 5 grid is selected. Each pixel is fit individually. A final determination of points is made based on a weighted average by SNR of the 8 highest SNR points.

Mechanical Testing

Catheter mechanical testing was conducted using two test setups. Initial screening was conducted using an Instron mechanical tester (Figure 31). A rigid metal insertion stylet was placed in the inner lumen of the catheter. The catheter was gripped around its circumference 1 inch from the proximal end. This grip fixture mimicked the position of the surgeon's hand during the procedure. The stylet served to add rigidity to the catheter, but force was not applied axially to the stylet from the distal end. The catheter was translated linearly through the template and along the obturator at a rate of 1 cm per second. The force was measured throughout the translation until the point of failure or end criteria.

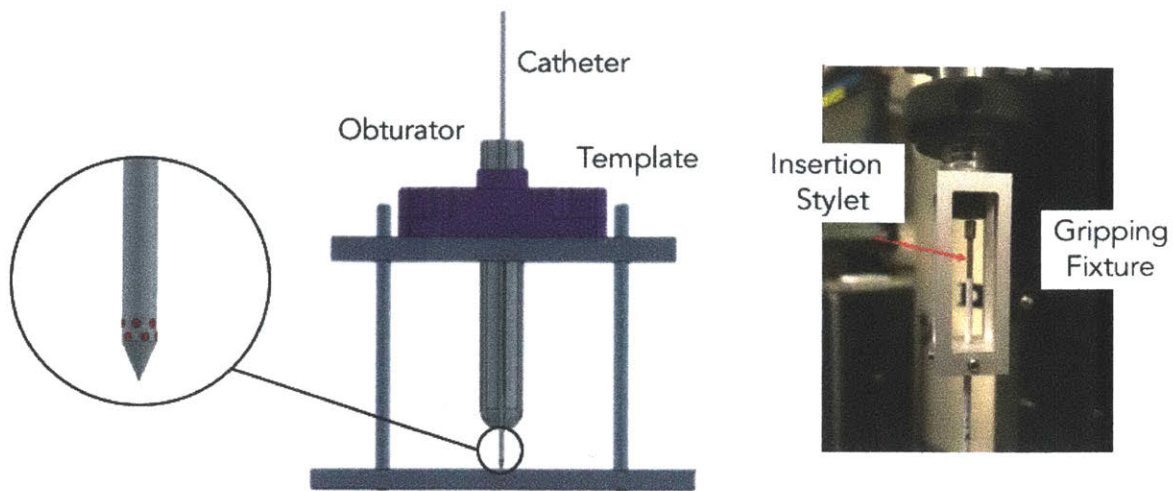


Figure 31 The catheter is gripped around the circumference 1 inch from the distal end. The catheter is gripped with four mutually perpendicular set screws.

A second mechanical testing configuration (Figure 32) was used to characterize use force and surgeon technique and allowed the surgeon to test catheters in a manner and orientation that mimicked *in vivo* use. A rigid metal insertion stylet was placed in the inner lumen of the catheter. The catheter was gripped by the gloved hand of the surgeon and pushed through the template and along the obturator in the same manner as the Instron testing. This method did not regulate insertion rate. Data was collected continuously using a force sensor.



Figure 32 An anatomically-oriented mechanical test setup was used to test catheters in the format used *in vivo*.

Page Intentionally Left Blank

Chapter 3: Plate-Based Thermal Screening Platform

Introduction

The measurement of thermal output from chemical and biological systems has been the focus of much research. Historical efforts have focused on different forms of calorimetry. These methods are most suitable for extremely low levels of thermal output, but their drawbacks are not justified for applications with less sensitive thermal measurement requirements. Calorimeters also require an isolated system that can limit throughput and prevent deployment for specific applications.

The work in this chapter focuses on the validation and characterization of a plate-based system for thermal measurement that enables liquid transfer to introduce stimuli and reagents. It is designed to allow liquid transfer after reaching thermal equilibrium which enables a baseline measurement to be made before introducing the stimuli. A system must be scalable, allow higher throughput, and not necessitate significant deviations from the existing experimental practice. The dissertation also discusses considerations and limitations when making thermal measurements. This system has been applied to both chemical and biological systems.

Background

Direct Methods of Characterizing Thermal Output

Efforts to measure thermal output have been wide ranging and are often driven by the specifics of the application. Techniques include calorimeters, infrared cameras, and contact measurements using thermocouples and thermistors. Much of the past research involving the measurement of thermal output, power dissipation, and thermal properties of materials has focused on the use of calorimeters (e.g. isothermal titration calorimetry). This has worked well to investigate the binding properties of enzyme/inhibitor, enzyme/substrate, and, protein/protein systems.⁵¹ Calorimeter test chambers remain relatively isolated to ensure high sensitivity but this limits their use as a high throughput screening platform for certain chemical and biological applications.

Thermal Measurements in Biological Systems

Efforts to adapt systems designed for measuring thermal output of chemical or biochemical systems for biological applications have produced mixed results. Initial work focused on adapting techniques used in calorimetry for chemical reactions to biological systems. They prevent the use of traditional cell culture consumables which introduces a source of deviation from normal cell culture protocols.

The desire to increase the throughput of thermal screening systems has led to the development of alternative screening platforms. One reported technique utilizes an infrared (IR) camera contained in a cell culture incubator.⁵² This method has the potential to be much higher throughput (whole plate) while allowing traditional cell culture consumables to be used, but also suffers from significant limitations. This technique will be revisited in the Discussion section and reviewed in the context of the results presented in this chapter.

Oxygen Consumption Measurement Methods

The interest in measuring thermal output from biological systems is partially driven by the desire to characterize thermal output from oxygen and non-oxygen sources of energy dissipation. Development of a screening platform that can be applied to biological systems also necessitates the understanding of the measurement of oxygen consumption rates.

Historically, methods and techniques have varied widely. Researchers have employed the Clark Electrode^{53,54} to make oxygen measurements in cell culture, an electrochemical-based method. More recently, many researchers have shifted to the Seahorse FX Analyzer (Agilent)⁵⁵⁻⁵⁸, an integrated system utilizing a fiberoptic probe that allows media addition. An important consideration in collecting OCR data and comparing results across platforms is the condition and environment of the measurement. The Clark Electrode requires constant stirring and actively consumes oxygen at the probe interface. Fiberoptic probe measurements are static and do not consume oxygen. The Seahorse Analyzer

provides “continuous” oxygen monitoring through a series of discrete longitudinal measurements. Each measurement requires probe movement to the surface of the cell monolayer which acts to stir the media.

System Design – Thermal Screening Platform

The work completed in this chapter was conducted in collaboration with Pfizer Inc. The thermal measurement system outlined in this section was conceived of and fabricated by Alex Lammers.

The design criteria for this system focused on making a thermal screening system that could measure individual wells of a polystyrene well plate. The well plate must allow liquid transfer into the test well to enable introduction of chemical stimuli and mixing for two-part reactions. Additional considerations focused on the fabrication of a system with a sufficiently stable thermal environment.

Efforts to mitigate thermal fluctuations included both system design approaches and data processing techniques. The well plate is placed in a test chamber that is contained inside an incubator kept at 37° C. The test chamber containing the well plate is a dual corrugated aluminum box to further isolate the experiment. The well plate sits on a printed circuit board with an array of surface mount thermistors (Figure 33).

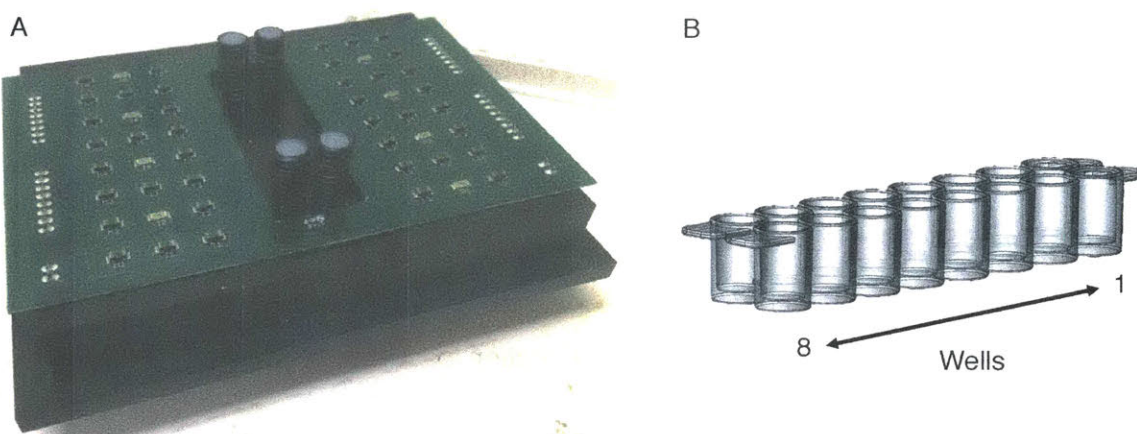


Figure 33 (A) Thermistor array on PCB. The middle column of components measures thermal output from each well. The outer columns on each side do not measure temperature, but are designed to keep the well plate level. Pairings of thermistors across the board produce the differential measurement. Pairings from top to bottom of the board are denoted 1 to 8. (B) A pneumatically coupled pair of 8 well strips. Well 1 corresponds to channel 1 at the top of the board. Photo and rendering by Alex Lammers.

Experiments are conducted in a custom, pneumatically-coupled well strip. Each well plate is produced from two 8-well strips. Wells in these strips are the same size as a well in a 96-well plate. Holes are drilled in the side wall of the well and tubing is epoxied in place between the wells to enable liquid transfer. Liquid transfer is initiated by pressurizing the reagent well while venting the test well.

Efforts were taken to minimize evaporative losses from the liquid in each well to avoid confounding the measured thermal output. A high viscosity (1000 cSt) silicone oil was dispensed on top of the aqueous liquid in the reagent and test wells. The well plate is also covered with a sheet of silicone septa to further reduce evaporation. The septa sheet also seals the wells to allow pressurization for liquid transfer.

The system is designed such that measurement and liquid transfer is mirrored left-to-right across the array of thermistors. One side of the board serves as the control side and one as the experimental. The control side serves two primary purposes: to account for any thermal differences or thermal output from mixing associated with the transfer of liquid,

and to allow for subtraction of thermal fluctuations occurring in the experimental test chamber. This produces a differential measurement that removes background fluctuations and transient thermal excursions associated with mixing. Thermal fluctuations are further reduced through subtraction of background excursions as measured at other thermistors in the array.

System Validation

System performance was validated in three key areas: 1) thermal stability, 2) rate of mixing following liquid transfer, and 3) characterization of the system sensitivity. These three performance specifications dictate the limit-of-detection of the system.

Thermal stability was evaluated under four distinct conditions: in the incubator but outside of the experimental test chamber, a thermistor inside the test chamber, a differential thermistor measurement (experimental side minus control side), and double differential measurement (differential measurement and subtracting fluctuation measured by thermistors at the top and bottom of the array) (Figure 34). Variability was evaluated using the metric of standard deviation. The differential and double differential methods performed similarly and greatly reduced thermal fluctuations compared to the active and passive insulation methods alone.

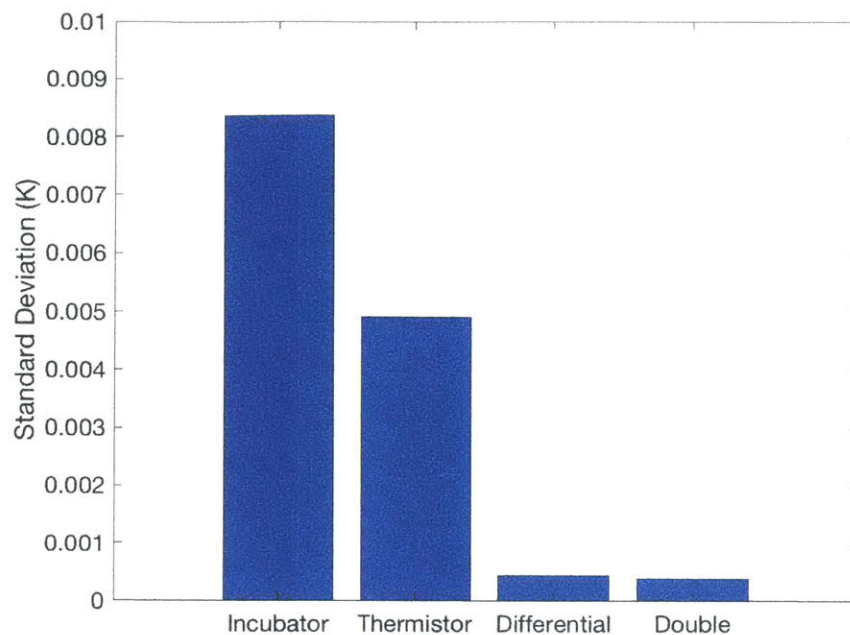


Figure 34 The passive corrugated aluminum enclosure reduces the standard deviation of the temperature during a steady-state period by almost 50%. Data processing techniques to further subtract remaining thermal background fluctuations reduced the standard deviation to under 10% of the incubator fluctuations.

The best performing technique was the double differential measurement, which subtracts the temperature associated with the mirrored well on the other side of the board as well as the average of the temperature seen by thermistors at the top and bottom of the array. This technique achieved a standard deviation that was 10% that of the incubator.

Liquid transfer testing was conducted to determine the rate of mixing to ensure that the liquid was fully mixed in a period of time significantly shorter than the anticipated thermal response. The reagent well was pressurized for a period of 45 seconds to ensure full transfer and to account for minor differences in liquid transfer rate between different well plates. The silicone oil on top of the media in the reagent well also serves to plug the transfer tube and prevent the introduction of air and bubbling of the liquid in the test well. The mixing was characterized with a water-soluble dye (Figure 35).

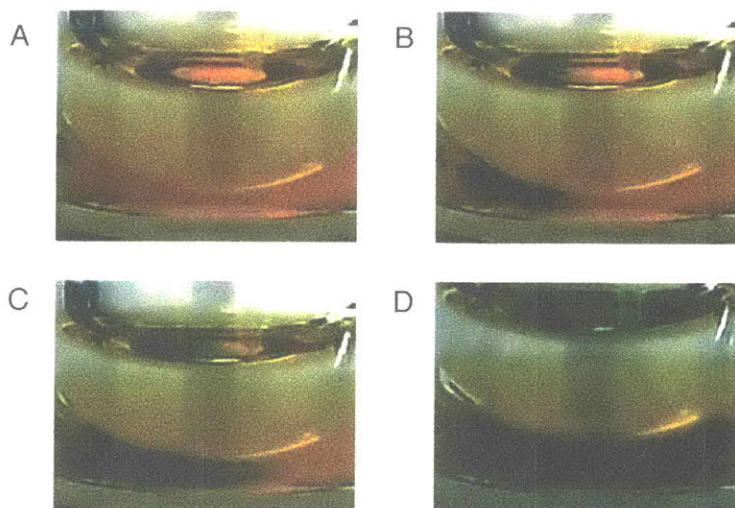


Figure 35 The real-time micro calorimeter enables rapid mixing. The four images show the mixing of cell culture media colored with different water-soluble dyes. (A) Before liquid transfer, (B) 0.25 seconds after liquid transfer begins, (C) one second after liquid transfer begins, and (D) two seconds after liquid transfer begins.

Mixing is observed to be almost immediate with the dye being fully distributed within the test well within the first two seconds of liquid transfer. This ensured that the measured thermal signal was not influenced by the mixing rate.

The relationship between temperature change and power output was characterized by passing a known current through a resistor. A surface mount resistor ($10\text{ K}\Omega$) was epoxied to the bottom of a well plate using a thermally conductive epoxy. Resistors were placed in the middle of two wells (4 and 5). Current was passed through the resistors in series at four different power output levels, while the temperature excursion was measured on all 16 thermistors (8 experimental and 8 control). An average temperature excursion value was calculated after reaching steady state. This process was conducted at power output

levels of 3.24 μW , 6.25 μW , 12.25 μW , and 25 μW (Figure 36). This calibration curve serves to convert measured temperature excursion to power output levels.

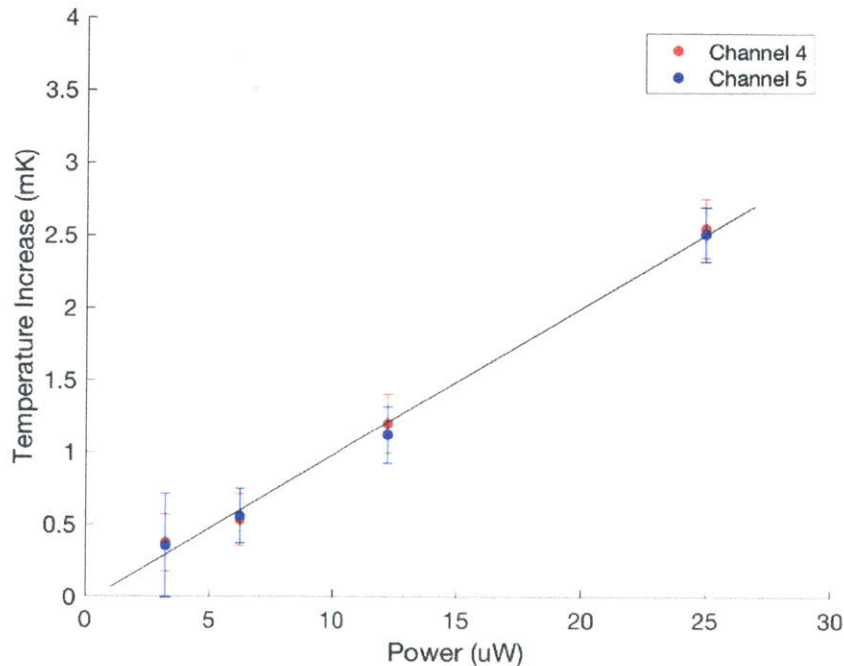


Figure 36 Resistor-based calibration of the system shows a linear response that is statistically equivalent for channels 4 and 5. Each calibration point is $n=7$. The linear fit of the averages across both channels has an $R^2 = 0.9962$.

Thermal Crosstalk

The thermal crosstalk was evaluated between neighboring and nearby wells within a well plate to determine the ability to evaluate distinct experimental configurations within a single plate. The thermal excursion measured in the well immediately adjacent to a well containing a resistor dissipating power was 40% to that of the resistor well (Figure 37). The signal is still detected in the outermost wells which experience a temperature increase of 7% of that of the resistor well. This result requires consideration of experimental layout and prevents distinct configurations from being evaluated in neighboring and nearby wells due to the significant thermal crosstalk. The thermal crosstalk can, however, be used to boost the signal of neighboring wells when the experimental conditions being tested are the same and the system is mirrored.

Experiments discussed throughout this chapter include identical experimental configurations in wells 4 and 5. These are treated as independent measurements due to equivalent thermal crosstalk and mirroring between these wells.

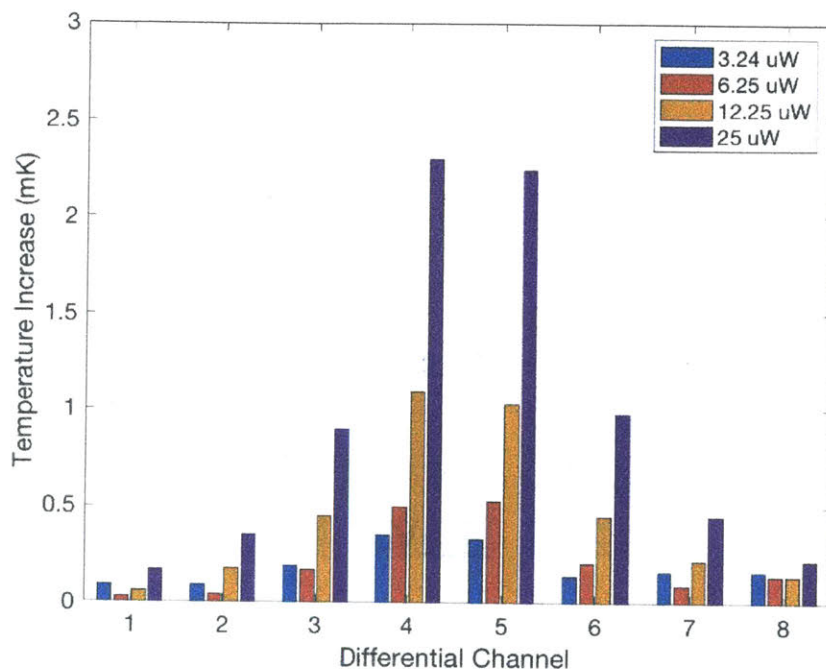


Figure 37 Power is dissipated in channels 4 and 5. The thermal crosstalk is measured in the neighboring wells on either side. The thermal signal is measurable in all channels.

Background Evaporation

Background evaporation from aqueous liquids in the well can be a large source of variability in the measurement. A multistage approach was used to reduce evaporation-related variability. This included the use of a silicone septum and anti-evaporation silicone oil. The cooling effect from evaporation without silicone is on the order of 10x larger than the limit of detection for the system. Steps can be taken to mitigate evaporation of media, but they must be balanced with the need to allow oxygen to diffuse to the media for biological applications of the platform. Different volumes of high viscosity silicone oil (1000 cSt) to mitigate evaporation effects were evaluated (Figure 38). A volume of 130 μ L was

selected because of the significant reduction in evaporation experienced. Space constraints in the well prevented larger volumes of silicone oil from being used.

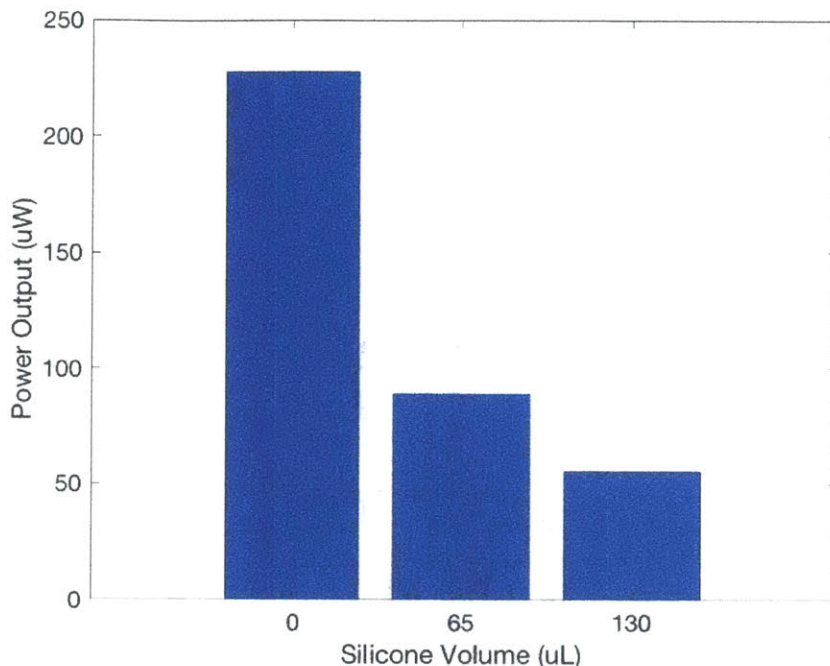


Figure 38 The power output as a result of evaporation. Power levels determined by monitoring well strip weight.

Thermal Excursion from Liquid Transfer

The sensitive nature of this system results in the detection of thermal excursions related to the transfer of liquid from the reagent well to the test well. This excursion has a transient and steady-state component. The transient component is a result of differences in the temperature of the liquid in the reagent well and the liquid in the test well. The new steady-state thermal signal is likely a result of changes in the boundary conditions. There are two primary sources of these changes, a reduction in the evaporation rate of the media in the reagent well as a result of liquid transfer and permanent changes height of the liquid test well. The average thermal excursion as a result of liquid transfer was 0.46 mK (± 0.78 mK stdev). Detectable thermal signals during experimental use must be in excess of this level. Using the limit of detection relationship (eq below), the minimum detectable thermal signal

that can be reliably measured is 1.75 mK. This corresponds to a power output of 17.5 μ W.

$$\text{LOD} = \text{LOB} + 1.645 * (\text{stdev low level})$$

Results

Measurement of Thermal Output from Chemical Reactions

The thermal screening platform was used to measure the output from a two-part chemical reaction. This was evaluated through thermal measurement of a zero-order chemical reaction. These results also served the secondary purpose as an additional calibration method since the expected power output from the reaction was known. This relationship was evaluated through a urea hydrolysis reaction⁵⁹ (Figure 39). The screening platform is less responsive to the urea hydrolysis power dissipation as evidenced by the smaller thermal response for a given power output. This is due to less efficient transfer of heat to the thermistor due to reaction occurring in the bulk. Thermal transfer from an adherent resistor is more efficient than the bulk urea hydrolysis-based experiment.

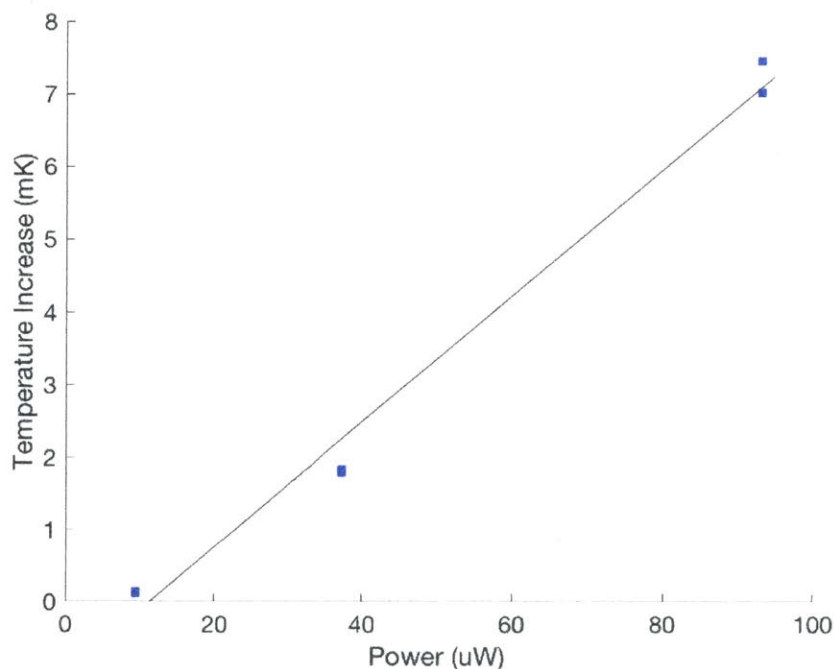


Figure 39 Power dissipated from a urea hydrolysis reaction. $n=2$ at each power dissipation level. The data points are overlapping for the two lower power dissipation levels.

Measurement of Thermal Output from Biological Systems

This screening platform also has applications in the measurement of biological systems. Commercially available thermal measurement platforms are even less suitable for biological applications due to the required deviations from standard cell culture protocols. Published literature regarding thermal output has suggested stimulated levels of oxygen consumption could produce thermal excursions on the order of 1 K,⁵² well within the measurement capabilities of this system. Sources of this level of thermal excursion were not individually identified, but can be assumed to be a combination of both OCR (oxygen consumption rate) and non-OCR mechanisms. Further exploration of oxygen measurement methods was required to better understand making OCR and thermal measurements in static cell culture.

Oxygen at Cell Monolayer – Seahorse FX Analyzer

Note: All data collected using the Seahorse FX Analyzer was collected by Michael Rukstalis (Pfizer). Analysis presented was conducted by the dissertation author (Gregory Ekchian).

The Seahorse FX Analyzer (Agilent) has become an extremely common method of characterizing OCR. It was used as a frontline screening tool to select cell lines for subsequent testing. The C2C12 (ATCC) murine muscle line was selected due to its large response to stimulus with DNP (dinitrophenol), a mitochondrial uncoupling agent which increases oxygen consumption and thermal output.

The Seahorse Analyzer is often used to characterize response of a well of cells under different conditions. Some have attempted to present the results on a per cell basis, but this requires an assumption regarding the percentage of the well that is sampled. The Seahorse Analyzer operates by lowering a microchamber containing a fiberoptic probe over a portion of the well. Knowledge that the probe only samples a subset of the cells in the well should be considered when converting the Seahorse data into a per cell measurement.

Basal OCR was characterized at a range of cell densities (90,000 to 363,000/cm²) and per cell OCR was determined to be independent of cell density (Figure 40). Per well measurements were normalized based on a per cell basis assuming 30% of the well surface was being sampled. This percentage is based on the geometry of the well and the probe. Per cell OCR ranged between 20.55 and 26.81 fmol/min/cell. This is higher than some of the reported OCR values from literature which assume sampling of 100% of the well.

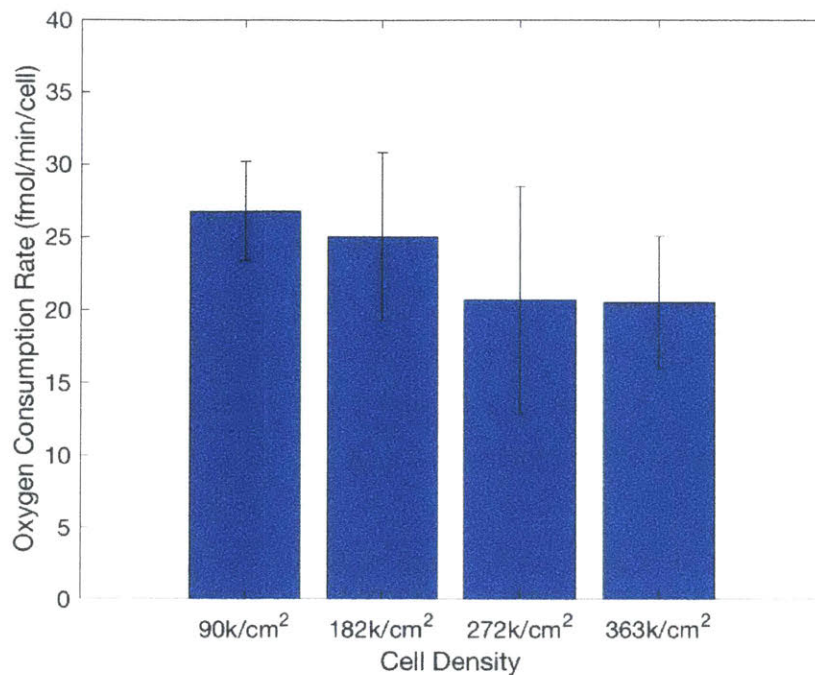


Figure 40 Basal oxygen consumption rate for a range of cell densities.

The magnitude and the kinetics of the response to DNP stimulus were evaluated to select the appropriate DNP dose (Figure 41). The DNP dose response was not linear. A plateau was observed between 50 μ M and 100 μ M. Exposure to 150 μ M produced a weaker response than 50 μ M. A DNP concentration of 50 μ M was selected to avoid excessively stressing the cells and to avoid introducing complications associated with a rapid decrease in oxygen consumption rate.

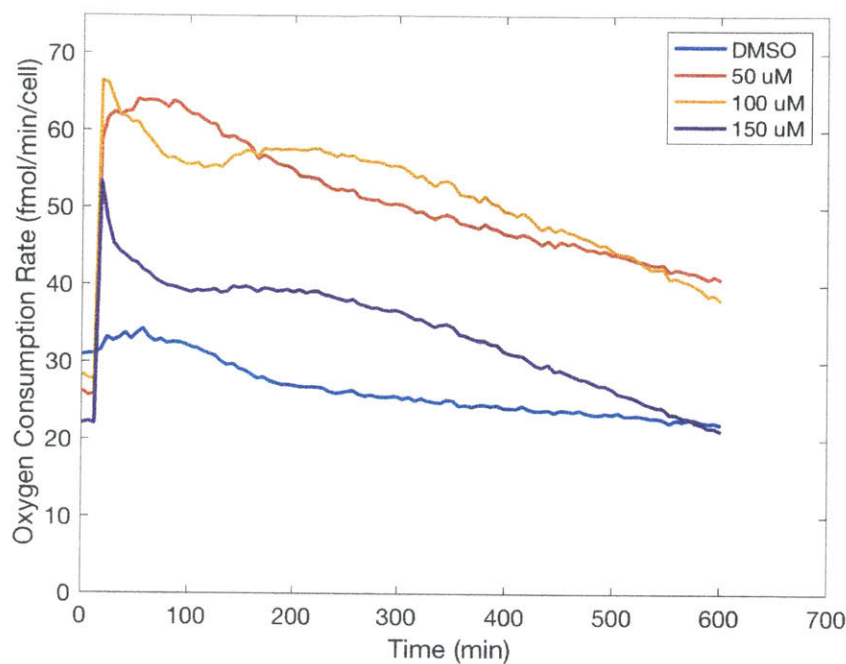


Figure 41 Time course response of DNP addition to C2C12 cells. The response was best sustained for 50 μ M DNP. Higher concentrations of DNP were not observed to increase the OCR response and, in some cases, produced a smaller increase.

A window 60 to 160 minutes following the addition of DNP was used to quantify the OCR change in response to DNP compared to the basal OCR (Figure 42). The 50 μ M DNP concentration produced a greater than two-fold increase in the OCR from the basal rate.

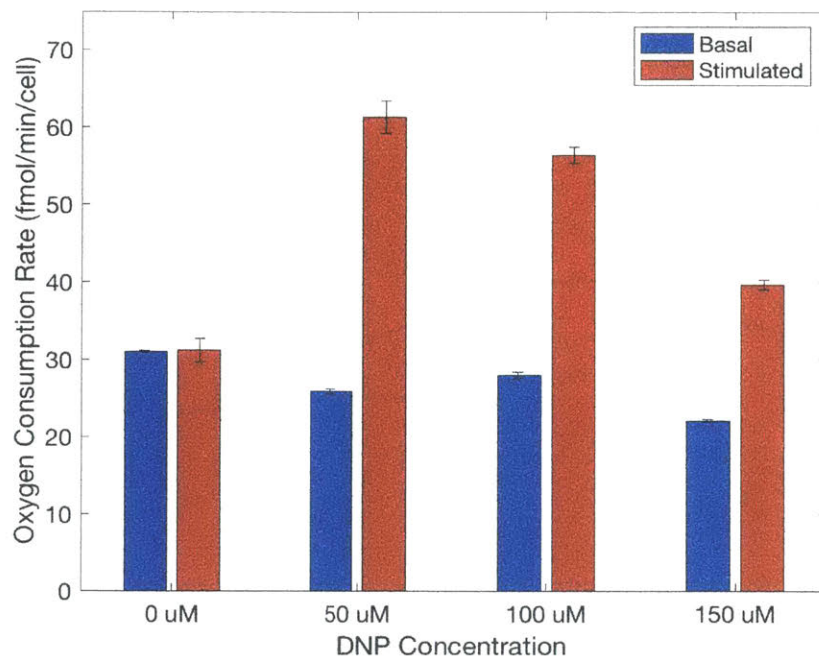


Figure 42 The difference in OCR between the basal period before DNP addition and the 60 – 160 minute window after DNP addition. Per cell power outputs were normalized assuming 30% of the cell monolayer was contributing to the measurement.

The data from the Seahorse Analyzer can more accurately be represented as a sequence of discrete oxygen measurements. Each measurement cycle involves the probe being lowered to the cell surface, remaining at that location for 2-4 minutes (depending on settings), and then returning to the resting position away from the cell surface.

Probe movement provides a drastically different experimental condition than static cell culture, which relies heavily on diffusion to transport oxygen from the surface in equilibrium with the atmosphere to the cell monolayer. The cyclic probe movement that coincides with each measurement introduces an additional oxygen transport mechanism due to mixing in the media. The movement occurring immediately prior to measurement initiation serves to deliver a fresh supply of oxygen and nutrients to the cell monolayer.

The raw partial pressure data was analyzed during each probe cycle to characterize the influence of probe movement on the oxygenation in the media (Figure 43). Partial pressure measurements began immediately after the probe had moved into position above the cell monolayer. Measurements continued for 2-4 minutes depending on the settings, with a measurement occurring roughly every 15 seconds. There are three immediate observations from analysis of this data: the decrease in the partial pressure during each cycle, the difference in the first point measured during the basal and stimulated cases, and the return to a consistent partial pressure between measurements.

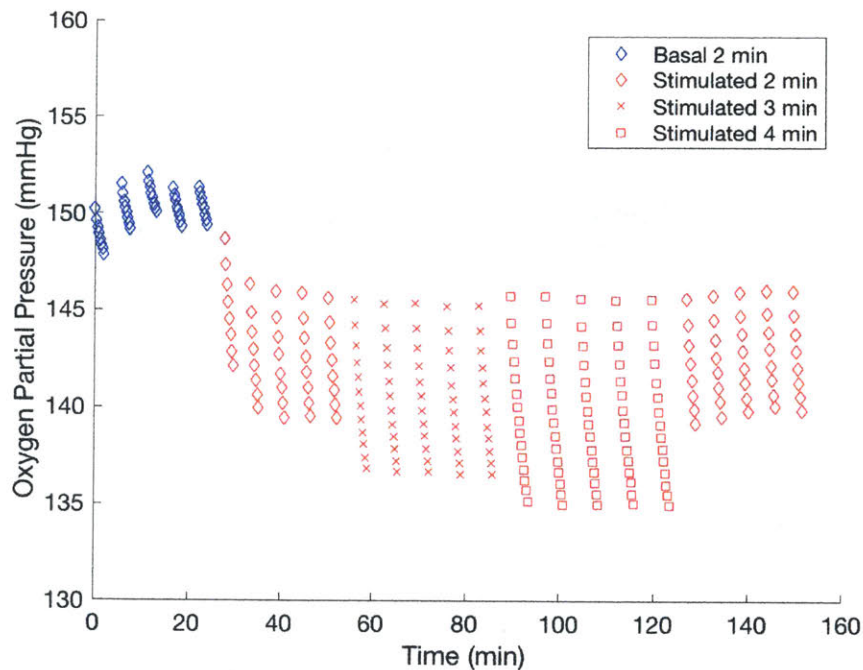


Figure 43 The partial pressure drops in response to the probe being positioned immediately above the cell monolayer. The probe first measures oxygen consumption prior to DNP (two minute measurement window) and after DNP addition with a two minute measurement window, three minute measurement window, four minute measurement window, and a two minute measurement window. Five measurements were made under each configuration.

A decrease in the partial pressure occurs while the probe is parked over the cell monolayer and has created a pseudo diffusion limited system. Absent movement of the probe, the oxygen level does not return to the initial partial pressure and cannot support a sustained elevated OCR which is a function of the slope of the concentration immediately after probe movement. The difference in the initial partial pressure between the basal and stimulated measurement is a representation of the non-stirred differences in oxygen consumption. The lower partial pressure following the addition of DNP is indicative of greater oxygen consumption. The slopes of these different regions were analyzed to determine if there was a dependence on probe dwell duration. Minimal differences in the calculated slope during each condition (2 min, 3 min and 4 min) were observed (Table 4).

Table 4 Slope of partial pressures without and with DNP.

| | Park Duration | Slope (mmHg/s) |
|---------------------|---------------|----------------|
| Basal | 2 min | -0.018 |
| Stimulated (DNP) | 2 min | -0.054 |
| | 3 min | -0.049 |
| | 4 min | -0.047 |

The Seahorse Analyzer creates a drastically different environment than many of the static assays that exist and the plate-based thermal screening platform that is the focus of this chapter. It was important to characterize the oxygen consumption rate in a format that closely mimics the thermal measurement system. An oxygen measurement system that used the same well plates and anti-evaporation techniques was developed. This system used a fiberoptic probe positioned (200 μm diameter) above the center of the cell monolayer. This probe is sized to have minimal impact on oxygen diffusion to the cell monolayer and can therefore remain in position throughout the duration of the experiment unlike the probe in the Seahorse system. This allows the oxygen gradient to remain constant throughout the experiment. Basal measurements were taken first, and liquid was transferred after the system reached a steady state (Figure 44). The liquid introduced to

the test well was either media with or without DNP. Experiments were conducted using 20,000 cells per well (63,000 cells/cm²).

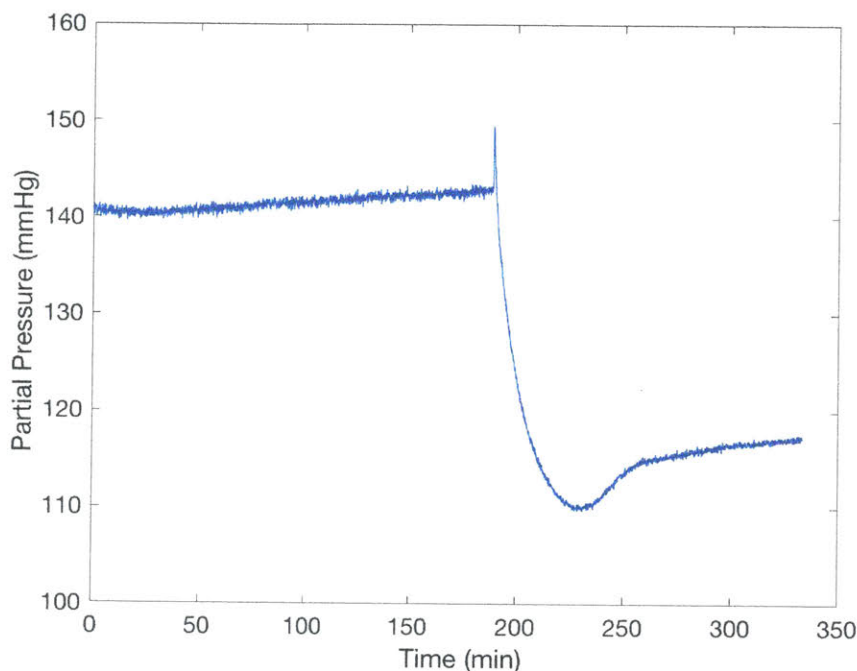


Figure 44 Example time course of oxygen measurement in a static environment. Liquid transfer occurs at 189 minutes.

The oxygen measurement is continuous throughout the transfer process. The immediate spike following transfer is due to the introduction of fresh, well-oxygenated media into the recipient well. This new supply of oxygen is quickly depleted and the system approaches a new equilibrium. The new equilibrium is a combination of two distinct phenomena: the increased height associated with liquid transfer and the addition of a chemical agent. The liquid transfer triples the media height. The slope immediately post liquid transfer corresponds to a similar oxygen environment as the mixing that occurs with the Seahorse Analyzer. The slope 1 to 3 minutes after liquid transfer was characterized for the addition of media with and without DNP. DNP addition into a well without silicone above the media was also evaluated (Table 5).

Table 5 Summarizes the slope of oxygen partial pressures collected with the fiberoptic probe.

| | Silicone Oil | Slope (mmHg/s) |
|---------------------|--------------|----------------|
| Basal | Yes | -0.0165 |
| Stimulated (DNP) | Yes | -0.0434 |
| | No | -0.0464 |

The relationship between the slope under basal vs. stimulated conditions is also very similar between these two methods indicating that liquid transfer in the static system mimics probe movement of the Seahorse system. The elevated OCR with DNP is short-lived in the static system. The system settles to a new steady-state OCR post liquid transfer. This is characterized by a lower partial pressure. This partial pressure is independent of the presence of DNP (Figure 45) suggesting the change is predominately a function of the height change.

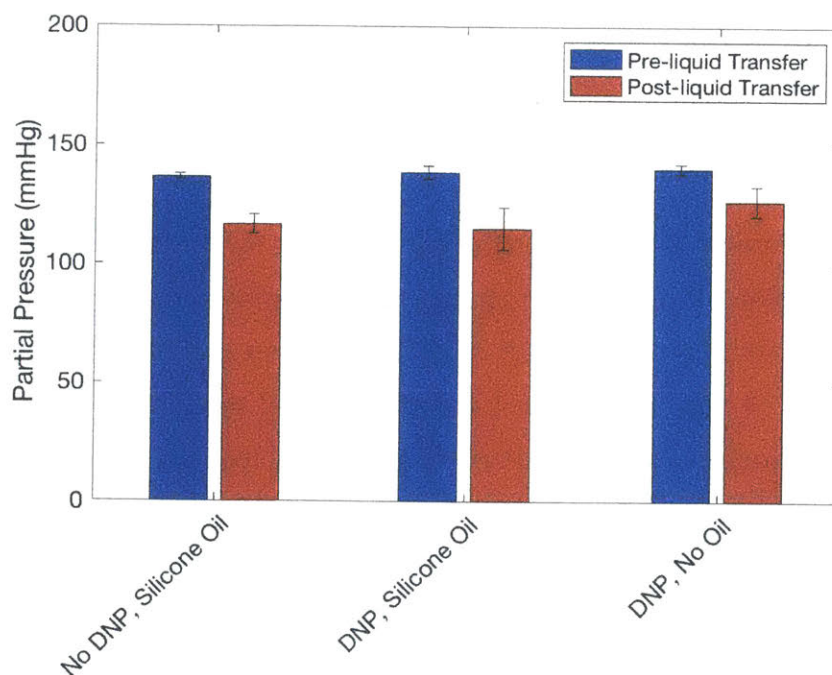


Figure 45 The decrease in partial pressure is driven by the increased height rather than the response to DNP.

Obtaining the OCR from the fiberoptic probe measurements requires determination of how diffusion of oxygen is controlled. Partial pressure measurements before and after the addition of DNP were compared to determine if silicone oil was limiting diffusion of oxygen. The partial pressure of with and without oil were the same both before and after DNP addition. This indicates that the diffusion is only limited by the aqueous layer (not the silicone) and follows Fick's First Law:

$$Flux = J = -D \frac{\Delta c}{\Delta d} = -D \frac{C_B - C_T}{h_m}$$

The increased oxygen gradient following liquid transfer is not large enough to overcome the increased height (3x). This results in a lower oxygen consumption rate (Figure 46) after liquid than before liquid transfer. Oxygen consumption in a static system would, therefore, not be expected to cause an increase in thermal output due to DNP addition.

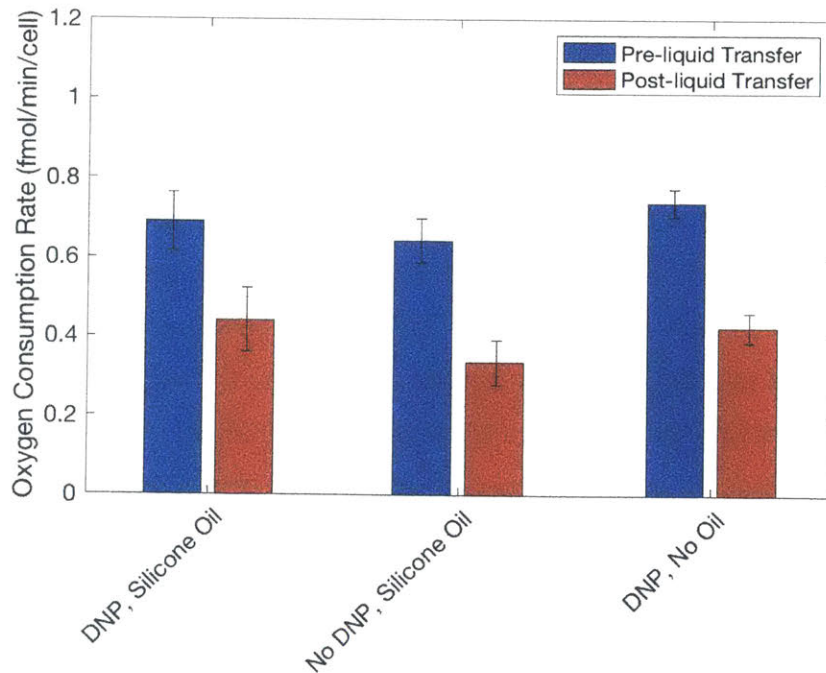


Figure 46 OCR was independent of the presence of silicone oil on top of the media. In all cases (with and without DNP), a decrease in OCR was observed after the liquid transfer.

The thermal measurement of the C2C12 cells was also conducted using the thermal screening platform to see if the previously reported level of thermal output could be attributed to a non-OCR mechanism. Measurement of cells in response to DNP was on the order of 1 mK (three orders of magnitude less than the 1 K reported in the literature). The measured thermal output resulting from DNP exposure was not statistically different from exposure to media without DNP or from the thermal excursion associated with liquid transfer alone (no cells).

Discussion

This work provides valuable insight into the considerations that should be taken when measuring thermal output using a plate-based approach. The screening platform was validated and applied to both chemical and biological systems. Techniques for measuring OCR were explored to provide context for the results obtained from the cell system evaluated as part of this work.

Primary considerations in system design and experimental protocol focus on the need to reduce evaporation and consider thermal crosstalk when deciding on the position of distinct experimental configurations. Specific considerations for biological systems, beyond the application agnostic ones, include the method of oxygen transport in the well. Some oxygen and thermal measurement systems involve stirring or mixing, either intentionally or as a byproduct of the measurement method. This provides a drastically different oxygen transport profile than static systems that rely on a diffusion-based transport mode. This is an important consideration when comparing to results obtained from *in vitro* cell culture which rarely involves frequent mixing. Diffusion-based biological systems are more likely to suffer from lower oxygen levels, a lack of nutrients, and a more acidic environment at the cell monolayer providing further sources of discrepancy between different systems. These microenvironment changes are important to consider when comparing results measured with different systems and techniques.

This difference was most apparent when conducting oxygen consumption measurements between mixed and unmixed systems. The difference in the measured OCR was an order of magnitude different. The measurements made using the Seahorse Analyzer occur immediately after the probe moves from the rest position to the cell monolayer. The movement of the probe disrupts the diffusion-based oxygen gradient and provides a temporary spike in the oxygen content at the cell monolayer.

Another aspect of this work was to explore previously reported results in the literature of a 1 K increase in the temperature of cells in culture when stimulated with a mitochondrion uncoupling agent. This measurement was obtained using an IR camera in a static system. The work also evaluated distinct experimental configurations in neighboring wells which would be prone to significant levels of thermal cross-talk, particularly at 1K of thermal output. It is also unlikely that a static system would provide any sustained increase in oxygen consumption rate. Further exploration of the results reported in the literature are needed to determine the source of this 1 K increase in temperature.

This work presents a validated thermal measurement system with a sensitivity of 1.75 mK. This was used to measure thermal output from a chemical reaction system. The maximum utility of this system and other diffusion-limited systems is in thermal measurements of non-oxygen based thermal output (e.g. screening for binding)⁶⁰. The use of this platform for such applications is the focus of continued work in the Cima Lab. Continued work related to the system design focuses on further reducing the background thermal excursion associated with liquid transfer to improve measurement sensitivity.

Methods

Data Collection

The surface mount thermistors were populated on a printed circuit board. The thermistors are powered in series with a constant current using a Kiethley 6210 current source. Thermistor resistance values were obtained by measuring voltage and using Ohm's law to convert to a resistance. Voltage measurements were made using a 2182A

Nanovoltmeter. Resistances are then converted to temperatures using the Steinhart-Hart equation.

Power Output Calibration

Conversion of thermal measurements to power output was conducted through the use of a calibration curve developed by conducting resistive power dissipation experiments. Resistors were epoxied into the bottom of the 8-well strip using a thermally conductive epoxy. The wells were filled with silicone oil. The calibration curve was based on power dissipation levels of 3.24 μW , 6.25 μW , 12.5 μW , and 25 μW .

Cell Culture

Mouse myoblast cell line C2C12 was grown in Dulbecco's Modified Eagle Medium (DMEM) with 10% (v/v) fetal bovine serum (FBS) and 1% (v/v) penicillin streptomycin. Cells were maintained in a humidified incubator at 37° C with 5% CO₂.

Tests are conducted in a customized cell culture plate that has a reagent well to hold the reagent to be introduced to the test well containing cells. Twelve to eighteen hours before the oxygen consumption measurement was commenced, the cells were removed from the cell culture flask and re-plated in a custom cell culture plate. The cells were plated at a density of 20,000 cells per well. Cell densities were determined with a hemocytometer. Densities were adjusted until the counted concentration was within 10% of the target concentration. DMEM with FBS is removed from the wells and replaced with DMEM without FBS prior to the beginning of the experiment.

The experimental test plate had a pair of wells that were coupled with microfluidic tubing (ID: OD:1/32"). The wells were covered with a molded silicone sheet. The sheet was adhered to the polystyrene well-strip with a double-sided pressure sensitive adhesive. The assembled well strip was placed in the experimental test fixture with needles piercing the silicone septa. The needle in the reagent well was connected to a pneumatic system (OB1) to pressurize the well. The needle in the test well was connected to a vent.

Oxygen Consumption Measurements

A 200 μm diameter fiberoptic probe was placed at the bottom of the well immediately above the cell monolayer. Oxygen measurements were collected using the Oxylite Fiber-optic oxygen meter (Oxford Optronix).

Thermistor Calibration

This system utilizes NTC (negative temperature coefficient) thermistors for sensing. The relationship between temperature and measured resistance is most accurately represented with the Steinhart-Hart equation. The fit parameters of the equation were determined by measuring thermistor resistance at three known temperatures after allowing the system to reach equilibrium. Calibration was conducted at the nominal operating temperature of 37° C and outer bounds of 36° C and 38° C. A Steinhart-Hart relationship was determined for each thermistor to account for any slight differences in thermistor response.

Page Intentionally Left Blank

Chapter 4: Quantitative pH Sensor

Background

The depletion of oxygen in tumors has been thoroughly discussed in Chapter 2 of this dissertation. One of the results of the oxygen reduction in tumors is acidification of the tumor micro-environment. This occurs when glycolysis occurs in poorly oxygenated environments, producing lactic acid. Excessive lactic acid production leads to a drop in pH⁶¹. Extracellular tumor pH plays an important role in predicting treatment efficacy⁶² and monitoring treatment response. While the production of lactic acid is induced by a lack of oxygen, the two parameters are not always correlated⁶³. This necessitates distinct sensors to track each physiological parameter independently.

One of the most common metrics of tumor response is a reduction in tumor volume measured using an imaging platform (MRI or CT). It can be difficult to track tumor size between imaging sessions due to the changes in patient orientation in the scanner. An anatomical feature (such as a bone) or a small metallic fiducial marker can be used as a reference point to improve consistency between imaging sessions. The process is still highly operator dependent and prone to inaccuracies, even with the aid of one of these reference features.

Another challenge with this method is the potential lag between treatment initiation and a reduction in tumor size. An *in vivo* study in mice, presented in the British Journal of Cancer, has shown that a tumor pH drop can serve as a leading indicator of treatment success.⁶⁴ Rapid identification of patient response enables physicians to quickly pivot to alternative treatments or modify dose level in unresponsive patients. This provides a cost savings opportunity to the system because the patient isn't treated repeatedly with an ineffective therapeutic. It also allows patients to avoid side-effects from a treatment with a low likelihood of success.

A pH sensor capable of making repeated quantitative measurements over the duration of treatment would enable a more reliable method to track tumor response. This information could be used to make the decision to alter treatment dose or frequency in order to increase efficacy. The pH measurements in the previously referenced paper were completed with a pH probe.⁶⁵ The authors state the inevitability of patient discomfort associated with the use of a probe and stress the importance of achieving a non-invasive measurement method.

An ideal clinical pH sensor shares many of the same traits as the oxygen-sensing technology previously outlined. It should be quantitative, passive, non-migrating, MRI compatible, and sensitive in the relevant range. Prior efforts in the Cima Lab to develop quantitative MRI-based pH sensors focused on homopolymer configurations utilizing polyhydroxyethylmethacrylate (pHEMA).⁶⁵ These sensors meet many of the characteristics of an ideal pH sensor, but are limited in their range of sensitivity.

This sensor utilizes chemical exchange to measure environmental pH. A hallmark of chemical exchange-based pH sensors is the peak in the relaxation time vs pH curve. This occurs at the point of slowest chemical exchange. The peak relaxation time occurs at pH 6.5 for the pHEMA-based sensor (Figure 47). Values on both sides of the peak are realizable physiologically and given a single measured relaxation time, there would be no way to determine whether that value corresponded with a value to the right or left side of the peak.

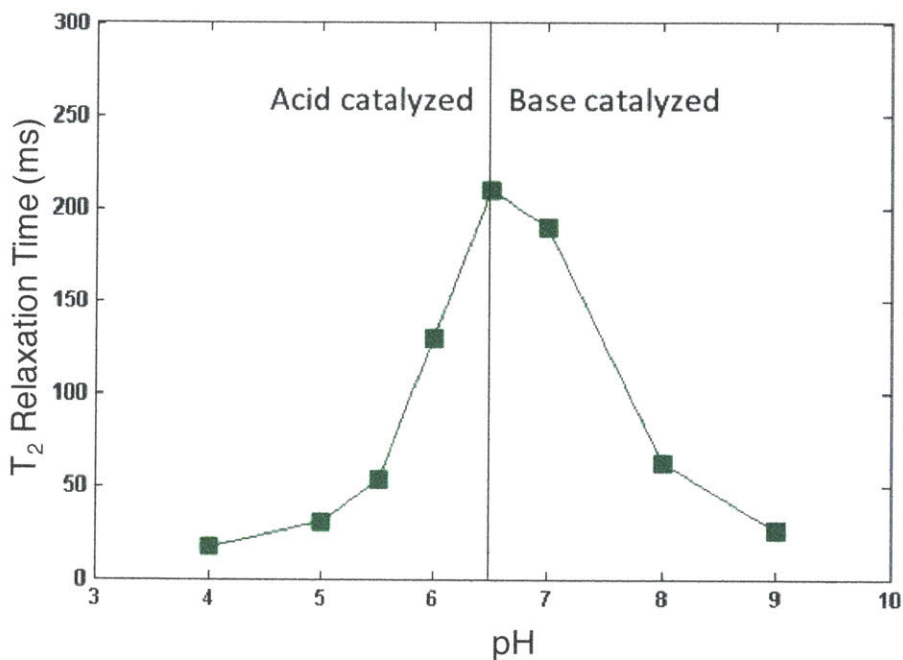


Figure 47 The relationship between T_2 relaxation time of a PHEMA-based sensor and pH.

The peak position of the sensor relaxation time profile is a function of the pKa. The pKa of a polymer can be controlled by adjusting its structure to improve the stability of the proton on the backbone. One promising method to achieve this is to develop a copolymer-based sensor that combines monomers that have complementary properties. Copolymers that consist of combinations of anionic and cationic monomers can work cooperatively, once polymerized, to enable certain configurations and levels of protonation that wouldn't otherwise be stable with a monomer. Copolymers that combine anionic and cationic repeat units can shift the pKa to higher levels⁶⁶.

Results

Different ranges of copolymer mixtures were evaluated for their T_2 relaxation profiles. Molar monomer ratios of 75%/25%, 70%/30%, 60%/40% and 25%/75% of dimethylaminoethylmethacrylate/acrylic acid were evaluated (Figure 48).

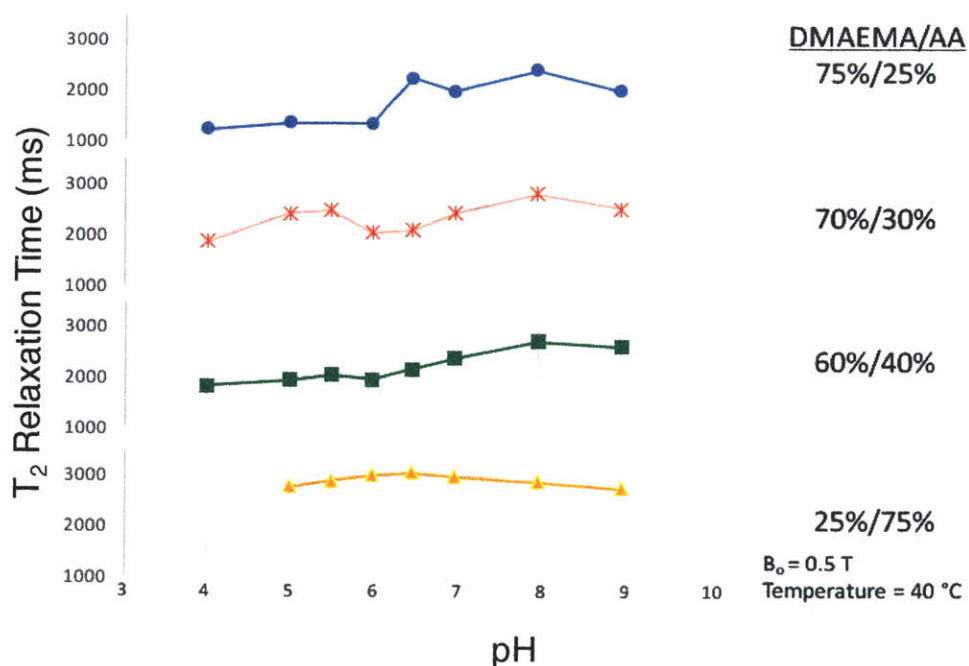


Figure 48 The T_2 relaxation profile of four co-polymer configurations of DMAEMA and AA. Configurations were evaluated for location of the local and absolute maxima and the existence of monotonically increasing regions.

The general shape of the curve can be attributed to the interactive effect of the copolymer configuration. The lower pKa acrylic acid repeat units serve as a sacrificial proton to provide charge balance to stabilize the protons present on the DMAEMA repeat units. This charge balance reduces the energy penalty associated with the proton remaining on the DMAEMA repeat unit at higher pH levels. The 60%/40% ratio was selected based on the primary peak occurring near pH 8 and the small secondary peak occurring in the acidic range.

The preferred copolymer formulation was further evaluated to characterize the variability of the sensor between batches (Figure 49). Variability of synthesis plays an important role in the ability to distinguish between different pH values, because sensor resolution is a function of how accurately the T_2 relaxation time is measured and variability in the sensor synthesis which impacts the underlying material response.

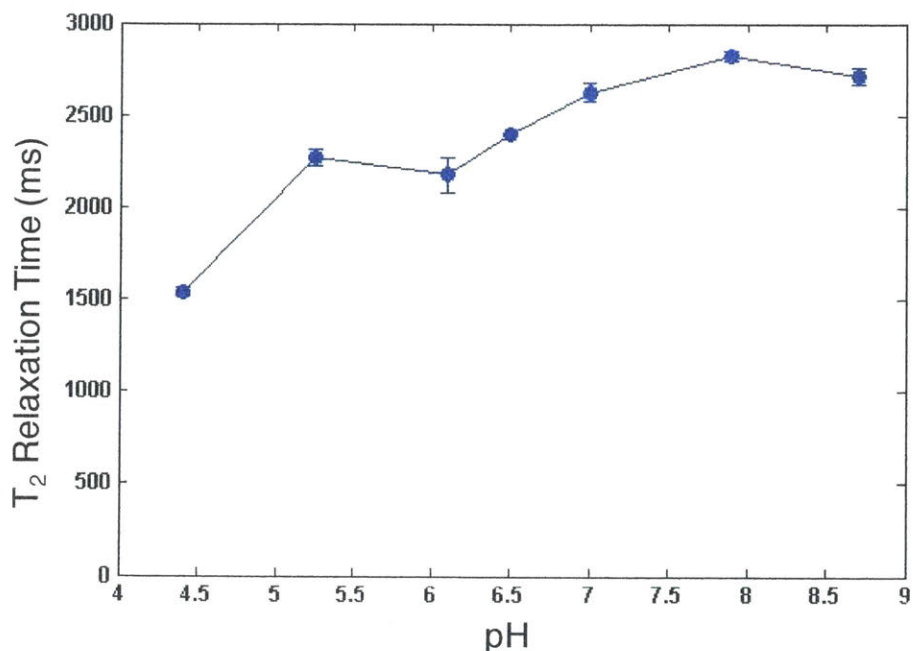


Figure 49 There is a low level of variability between distinct batches of copolymer pH sensors. Error bars represent the standard deviation across three samples.

Further Expansion of the pH Range

The T₂ relaxation time peak at pH 7.8 enables sensing at pH values between 6.25 and 7.8, the areas of greatest interest. Values above pH 7.8, to the right of the major peak, are not likely to occur *in vivo* and thus a measured relaxation time could be mapped to the proper pH with confidence and with little risk that the reading actually corresponds to the more basic pH. Sensitivity of this formulation is limited in the lower pH range by the presence of the secondary relaxation time peak and the relatively flat region between pH values of 5 and 6.25.

It is desirable to achieve a pH sensor that is capable of measuring the entire pH range to avoid the need to select the sensor formulation based on anticipated application and allow unexpected pH environments to be characterized. A method to achieve this involves physically combining two distinct sensors with different relaxation time/pH response curves (Figure 50). A proposed method for achieving this involves physically mixing the pHEMA sensor and the copolymer sensor after curing. Physically mixing the sensors

means that they experience the same environment but do not interact, in a manner similar to the distinct repeat units of the copolymer. These two materials are ideal for this application because of their complementary relaxation profiles, order of magnitude difference in relaxation time, and different peak relaxation time positions. No single pH values have pHEMA and co-polymer sensor relaxation times that are the same. Simultaneous measurement of these materials and the application of a multi-exponential fitting approach to the individual relaxation times can be decoupled and separately mapped into the pH domain.

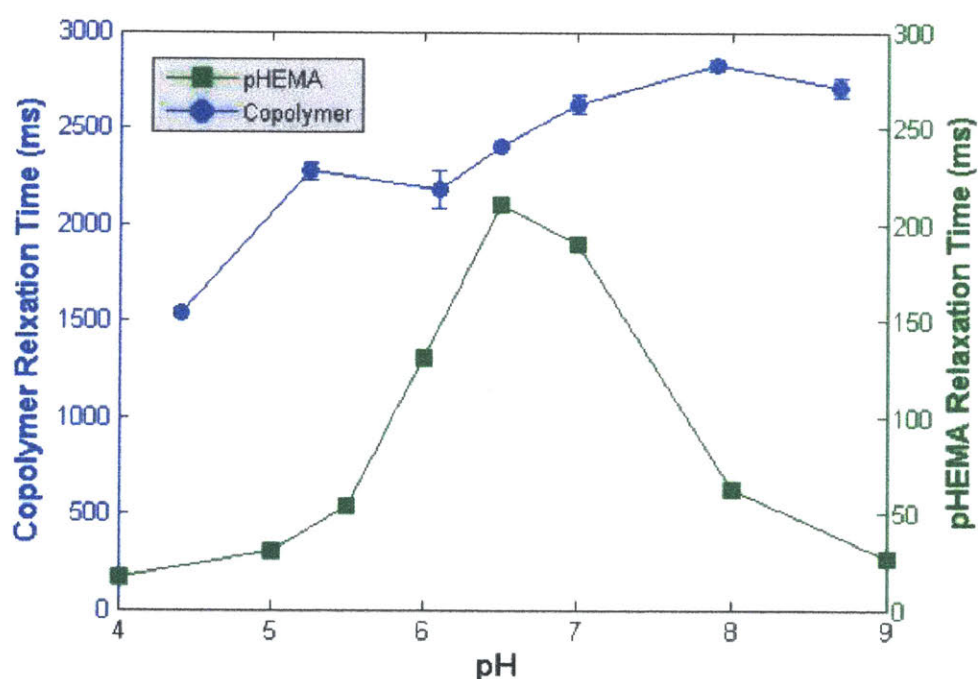


Figure 50 The copolymer and pHEMA sensors have peak positions at distinct pH values which allow them to be used together to map the full pH range. Figure shows the T_2 relaxation time of each material

Synthesis Process Improvements

The existing synthesis methods are sufficient to develop a sensor capable of measuring pH in the desired range, but it is important to have a robust process with minimized variability before transitioning to *in vivo* experiments or scaling to eventual clinical implementation. It was observed that polymerization proceeds rapidly after initiator

addition, and would begin during the dispensing process for the larger batch sizes required for scaled-up manufacturing. This is problematic because it introduces temporal dependency during synthesis which will hurt resolution. Methods to reduce synthesis sensitivity were explored, including initiator concentration, initiator type, and temperature during mixing (immediately prior to dispensing). The configurations evaluated are outlined in Table 6.

Table 6 The synthesis configurations evaluated.

| APS Concentration | Temed Concentration | Temperature Pre-Cure |
|-------------------|---------------------|-------------------------------|
| 5 mM | 5 mM | Room Temperature |
| 1 mM | 1 mM | Room Temperature |
| 5 mM | N/A | On Ice (10 min) before mixing |
| 5 mM | N/A | Room Temperature |
| 5 mM | N/A | Chilled 4°C (30 min) |

The hydrogel pre-polymer mixture was dispensed directly into 10 mm NMR tubes. The order in which the tubes were measured was randomized to avoid a measurement order-related bias. New initiator systems and synthesis configurations were evaluated based on three criteria: similarity of the relaxation time to the baseline sensor properties, variability across tubes, characterized by the standard deviation, and the difference in relaxation time between tube 1 and tube 6. A sensor produced with the baseline initiator system had an average relaxation time of 1213 ms with a standard deviation of 120.2 ms and a difference between tube 1 and tube 6 of 322 ms (Table 7). The most promising alternative initiator system used only 5 mM of APS (no TEMED) and the pre-polymer solution was placed at 4° C for 30 minutes prior to the addition of the initiator. This system produced an average relaxation time of 1188 ms with a standard deviation of 23.5 ms and a difference between tube 1 and tube 6 of -46 ms.

Table 7 The results of the five different synthesis configurations evaluated.

| APS Conc. | Temed Conc. | Thermal Treatment | Average (Tubes 1 to 6) | Std Dev (Tubes 1 to 6) | Tube 1 – Tube 6 |
|-----------|-------------|-------------------------------|------------------------|------------------------|-----------------|
| 5 mM | 5 mM | RT | 1213 ms | 120.4 ms | 322 ms |
| 1 mM | 1 mM | RT | 2024 ms | 30.3 ms | 82.6 ms |
| 5 mM | N/A | On Ice (10 min) before mixing | 1191 ms | 33.4 ms | -110 ms |
| 5 mM | N/A | RT | 1176 ms | 35.7 ms | -114 ms |
| 5 mM | N/A | Chilled 4°C (30 min) | 1188 ms | 23.5 ms | -46 ms |

Discussion

A quantitative pH sensor, capable of measuring the full pH range, has many clinical and research applications. The cross-linked polymeric nature of these sensors prevents migration, which allows longitudinal measurements at a fixed tissue location. The synthesis of a new co-polymer sensor that has improved sensitivity in the neutral pH range offers many new *in vivo* sensing opportunities. The synthesis process was optimized to reduce variability as the system scales to larger quantities. Approaches to further improve the clinical applicability of the sensor by mechanically mixing sensors of different formulations to expand the pH sensitivity to the entire pH range are also presented.

The next steps for the development of this technology involve translation of this sensor to a pre-clinical animal model. Much of the data supporting the importance of tissue and tumor pH is less established than the role of tissue oxygen levels. It is critically important to develop the pre-clinical, and eventually the clinical, data to support the adoption of the technology.

Methods and Materials

pHEMA Synthesis

HEMA (Hydroxyethyl methacrylate), EGDMA (ethylene glycol dimethacrylate), and deionized water are mixed in a 20 mL scintillation vial. The vial is then placed under a 3.5 Torr vacuum for 15 minutes to remove dissolved oxygen. EGDMA serves as a chemical cross-linker for the hydrogel system. APS (ammonium persulfate) and TEMED (tetramethylethylenediamine) are then added in 5 mM concentrations each. The pre-polymer solution is then dispensed in 1 mL volumes into an 8-well polystyrene cell culture plate that serves as a mold for the polymer synthesis. Curing occurs at 80° C for 30 minutes.

Co-polymer Synthesis

AA (acrylic acid), DMEMA (dimethyl amino ethyl methacrylate), EGDMA, and deionized water are mixed in a 20 mL scintillation vial. The vial is then placed under a 3.5 Torr vacuum for 15 minutes to remove dissolved oxygen. EGDMA serves as a chemical cross-linker for the hydrogel system. APS and TEMED are then added in 5 mM concentrations each. The pre-polymer solution is then dispensed in 1 mL volumes into an 8-well polystyrene cell culture plate that serves as a mold for the polymer synthesis. Curing occurs at 80° C for 30 minutes. Adjustments to the synthesis were made based on the results outlined previously.

Relaxometry Measurements

T_2 measurements were made using a small-bore benchtop relaxometer with a 0.5 Tesla field strength (Bruker). A CPMG pulse sequence was used to measure the T_2 relaxation time.

Experimental Setup

Experiments should be carried out in buffer with an ionic strength equal to that of *in vivo* conditions (~150 mM). This will take into account the screening effect that the materials

would encounter *in vivo*. Hydrogel samples were soaked in buffers for at least 48 hours before testing. Hydrogel samples were removed from the buffer before being placed in the NMR tube for measurement in the benchtop relaxometer. The surfaces of the hydrogel were blotted with a cloth to remove buffer on the surface of the sample.

Page Intentionally Left Blank

Chapter 5: Conclusions and Future Work

This dissertation presents on *in vitro* methods to measure thermal output in chemical and biological applications and the development of sensors for *in vivo* measurement of oxygen and pH. This work was motivated by unmet needs in clinical practice.

Clinical implementation of the *in vivo* oxygen sensor presents a tremendous opportunity to make a significant impact in the treatment of patients suffering from a wide variety of diseases and ailments. The early feasibility trial will provide critical information that guides the subsequent develop of a next generation of oxygen sensors. The oxygen sensor is a platform technology that provides opportunity for meaningful measurement in a wide variety of clinical and non-clinical applications. The presented future embodiments offer alternatives for enhanced sensitivity and suitability for long-term implantation to enable longitudinal tracking. The presented family of silicone-based oxygen sensors will enable customization of radiation dose distribution, something currently desired by clinicians but not possible with the existing offering of oxygen measurement methods. This has the potential to greatly improve treatment outcomes for patients with hypoxic tumors.

The thermal screening platform provides a research tool for plate-based measurement of chemical and biological systems. The system was validated using a resistor model and used to characterize the thermal output from a urea hydrolysis reaction. The thermal measurement system and a companion oxygen consumption measurement system were used to elucidate the complications associated with measuring oxygen consumption and the associated thermal output from *in vitro* cell culture. The greatest utility, currently, of this system is focused on measuring thermal output from systems not requiring oxygen consumption (e.g. chemical reactions and bacterial cultures).

Oxygen and pH are both associated with metabolic processes in living tissues. The change in pH is induced by a hypoxic environment in some cases, but in other cases these changes are not correlated. Tissue pH has been shown to play a role in treatment

efficacy, but the clinical data is less well established than the role tissue oxygen levels play in oncology. Past efforts to develop quantitative MRI-based pH sensors have been of limited utility due to the range of sensitivity being limited to the acidic range. The novel sensor presented has overcome the sensitivity limitations of past formats. This sensor provides the opportunity to develop the pre-clinical data to support translation of the sensor. This sensor could be used alone or in conjunction with the oxygen sensor.

References

- 1 Lauterbur, P. Image Formation by Induced Local Interactions: Examples Employing Nuclear Magnetic Resonance. *Nature* 242 (1973).
- 2 Liu, V. H., Vassiliou, C. C., Imaad, S. M. & Cima, M. J. Solid MRI contrast agents for long-term, quantitative in vivo oxygen sensing. *Proc Natl Acad Sci U S A* 111, 6588-6593, doi:10.1073/pnas.1400015111 (2014).
- 3 Li, M., Vassiliou, C. C., Colucci, L. A. & Cima, M. J. (1)H nuclear magnetic resonance (NMR) as a tool to measure dehydration in mice. *NMR Biomed* 28, 1031-1039, doi:10.1002/nbm.3334 (2015).
- 4 Kaur, J., Tuor, U. I., Zhao, Z. & Barber, P. A. Quantitative MRI reveals the elderly ischemic brain is susceptible to increased early blood-brain barrier permeability following tissue plasminogen activator related to claudin 5 and occludin disassembly. *J Cereb Blood Flow Metab* 31, 1874-1885, doi:10.1038/jcbfm.2011.79 (2011).
- 5 van Zijl, P. C. & Yadav, N. N. Chemical exchange saturation transfer (CEST): what is in a name and what isn't? *Magn Reson Med* 65, 927-948, doi:10.1002/mrm.22761 (2011).
- 6 Zhou, J., Payen, J. F., Wilson, D. A., Traystman, R. J. & van Zijl, P. C. Using the amide proton signals of intracellular proteins and peptides to detect pH effects in MRI. *Nat Med* 9, 1085-1090, doi:10.1038/nm907 (2003).
- 7 Ling, W., Regatte, R. R., Navon, G. & Jerschow, A. Assessment of glycosaminoglycan concentration in vivo by chemical exchange-dependent saturation transfer (gagCEST). *Proc Natl Acad Sci U S A* 105, 2266-2270, doi:10.1073/pnas.0707666105 (2008).
- 8 *Cancer Stats Facts: Cervical Cancer*,
 <<https://seer.cancer.gov/statfacts/html/cervix.html>> (2018).
- 9 Banerjee, R. & Kamrava, M. Brachytherapy in the treatment of cervical cancer: a review. *Int J Womens Health* 6, 555-564, doi:10.2147/IJWH.S46247 (2014).
- 10 Parkin, D. M., Bray, F., Ferlay, J. & Pisani, P. Global cancer statistics, 2002. *CA Cancer J Clin* 55, 74-108 (2005).
- 11 Koutsky, L. A. *et al.* A controlled trial of a human papillomavirus type 16 vaccine. *N Engl J Med* 347, 1645-1651, doi:10.1056/NEJMoa020586 (2002).
- 12 Green, J. A. *et al.* Survival and recurrence after concomitant chemotherapy and radiotherapy for cancer of the uterine cervix: a systematic review and meta-analysis. *Lancet* 358, 781-786, doi:10.1016/S0140-6736(01)05965-7 (2001).
- 13 Goel, S. *et al.* Normalization of the vasculature for treatment of cancer and other diseases. *Physiol Rev* 91, 1071-1121, doi:10.1152/physrev.00038.2010 (2011).
- 14 Secomb, T. W., Hsu, R., Ong, E. T., Gross, J. F. & Dewhirst, M. W. Analysis of the effects of oxygen supply and demand on hypoxic fraction in tumors. *Acta Oncol* 34, 313-316 (1995).
- 15 Gillies, R. J., Schornack, P. A., Secomb, T. W. & Raghunand, N. Causes and effects of heterogeneous perfusion in tumors. *Neoplasia* 1, 197-207 (1999).

- 16 Søvik, A. *et al.* Radiotherapy adapted to spatial and temporal variability in tumor hypoxia. *Int J Radiat Oncol Biol Phys* 68, 1496-1504, doi:10.1016/j.ijrobp.2007.04.027 (2007).
- 17 Milosevic, M. *et al.* Tumor Hypoxia Predicts Biochemical Failure follow Radiotherapy for Clinically Localized Prostate Cancer. *Clinical Cancer Research* (2012).
- 18 Höckel, M. *et al.* Association between Tumor Hypoxia and Malignant Progression in Advanced Cancer of the Uterine Cervix. *Cancer Research* 56 (1996).
- 19 Wilson, W. R. & Hay, M. P. Targeting hypoxia in cancer therapy. *Nat Rev Cancer* 11, 393-410, doi:10.1038/nrc3064 (2011).
- 20 Rischin, D. *et al.* Tirapazamine, cisplatin, and radiation versus cisplatin and radiation for advanced squamous cell carcinoma of the head and neck (TROG 02.02, HeadSTART): a phase III trial of the Trans-Tasman Radiation Oncology Group. *J Clin Oncol* 28, 2989-2995, doi:10.1200/JCO.2009.27.4449 (2010).
- 21 Lyng, H., Sundfør, K. & Rofstad, E. K. Oxygen tension in human tumours measured with polarographic needle electrodes and its relationship to vascular density, necrosis and hypoxia. *Radiother Oncol* 44, 163-169 (1997).
- 22 Movsas, B. *et al.* Hypoxia in human prostate carcinoma: an Eppendorf PO₂ study. *Am J Clin Oncol* 24, 458-461 (2001).
- 23 Nordsmark, M., Bentzen, S. M. & Overgaard, J. Measurement of human tumour oxygenation status by a polarographic needle electrode. An analysis of inter- and intratumour heterogeneity. *Acta Oncol* 33, 383-389 (1994).
- 24 Le, Q. T. *et al.* Comparison of the comet assay and the oxygen microelectrode for measuring tumor oxygenation in head-and-neck cancer patients. *Int J Radiat Oncol Biol Phys* 56, 375-383 (2003).
- 25 Vaupel, P., Briest, S. & Höckel, M. Hypoxia in breast cancer: pathogenesis, characterization and biological/therapeutic implications. *Wien Med Wochenschr* 152, 334-342 (2002).
- 26 Koong, A. C. *et al.* Pancreatic tumors show high levels of hypoxia. *Int J Radiat Oncol Biol Phys* 48, 919-922 (2000).
- 27 Fyles, A. *et al.* Tumor hypoxia has independent predictor impact only in patients with node-negative cervix cancer. *J Clin Oncol* 20, 680-687, doi:10.1200/JCO.2002.20.3.680 (2002).
- 28 Pitson, G. *et al.* Tumor size and oxygenation are independent predictors of nodal diseases in patients with cervix cancer. *Int J Radiat Oncol Biol Phys* 51, 699-703 (2001).
- 29 Höckel, M. *et al.* Intratumoral pO₂ predicts survival in advanced cancer of the uterine cervix. *Radiother Oncol* 26, 45-50 (1993).
- 30 Höckel, M., Vorndran, B., Schlenger, K., Baussmann, E. & Knapstein, P. G. Tumor oxygenation: a new predictive parameter in locally advanced cancer of the uterine cervix. *Gynecol Oncol* 51, 141-149, doi:10.1006/gyno.1993.1262 (1993).
- 31 Höckel, M. *et al.* Association between tumor hypoxia and malignant progression in advanced cancer of the uterine cervix. *Cancer Res* 56, 4509-4515 (1996).

- 32 Stone, H. B., Brown, J. M., Phillips, T. L. & Sutherland, R. M. Oxygen in human tumors: correlations between methods of measurement and response to therapy. Summary of a workshop held November 19-20, 1992, at the National Cancer Institute, Bethesda, Maryland. *Radiat Res* 136, 422-434 (1993).
- 33 Janssen, H. L., Haustermans, K. M., Balm, A. J. & Begg, A. C. Hypoxia in head and neck cancer: how much, how important? *Head Neck* 27, 622-638, doi:10.1002/hed.20223 (2005).
- 34 Jain, R. K. Antiangiogenesis strategies revisited: from starving tumors to alleviating hypoxia. *Cancer Cell* 26, 605-622, doi:10.1016/j.ccell.2014.10.006 (2014).
- 35 Hill, R. P., De Jaeger, K., Jang, A. & Cairns, R. pH, hypoxia and metastasis. *Novartis Found Symp* 240, 154-165; discussion 165-158 (2001).
- 36 Finger, E. C. & Giaccia, A. J. Hypoxia, inflammation, and the tumor microenvironment in metastatic disease. *Cancer Metastasis Rev* 29, 285-293, doi:10.1007/s10555-010-9224-5 (2010).
- 37 Chang, J. & Erler, J. Hypoxia-mediated metastasis. *Adv Exp Med Biol* 772, 55-81, doi:10.1007/978-1-4614-5915-6_3 (2014).
- 38 Knocke, T. H., Weitmann, H. D., Feldmann, H. J., Selzer, E. & Pötter, R. Intratumoral pO₂-measurements as predictive assay in the treatment of carcinoma of the uterine cervix. *Radiother Oncol* 53, 99-104 (1999).
- 39 Brown, J. M. & Wilson, W. R. Exploiting tumour hypoxia in cancer treatment. *Nat Rev Cancer* 4, 437-447, doi:10.1038/nrc1367 (2004).
- 40 Wang, J. Z., Li, X. A. & Mayr, N. A. Dose escalation to combat hypoxia in prostate cancer: a radiobiological study on clinical data. *British Journal of Radiology* 79, 7 (2006).
- 41 Viswanathan, A. N. *et al.* International brachytherapy practice patterns: a survey of the Gynecologic Cancer Intergroup (GCIg). *Int J Radiat Oncol Biol Phys* 82, 250-255, doi:10.1016/j.ijrobp.2010.10.030 (2012).
- 42 Viswanathan, A. N., Szymonifka, J., Tempany-Afdhal, C. M., O'Farrell, D. A. & Cormack, R. A. A prospective trial of real-time magnetic resonance-guided catheter placement in interstitial gynecologic brachytherapy. *Brachytherapy* 12, 240-247, doi:10.1016/j.brachy.2012.08.006 (2013).
- 43 Grover, S. *et al.* Image Guided Cervical Brachytherapy: 2014 Survey of the American Brachytherapy Society. *Int J Radiat Oncol Biol Phys* 94, 598-604, doi:10.1016/j.ijrobp.2015.11.024 (2016).
- 44 Garcia-Parra, R. *et al.* Investigation on tumor hypoxia in resectable primary prostate cancer as demonstrated by 18F-FAZA PET/CT utilizing multimodality fusion techniques. *Eur J Nucl Med Mol Imaging* 38, 1816-1823, doi:10.1007/s00259-011-1876-z (2011).
- 45 Nehmeh, S. A. *et al.* Reproducibility of intratumor distribution of (18)F-fluoromisonidazole in head and neck cancer. *Int J Radiat Oncol Biol Phys* 70, 235-242, doi:10.1016/j.ijrobp.2007.08.036 (2008).
- 46 Dewhirst, M. W. Relationships between cycling hypoxia, HIF-1, angiogenesis and oxidative stress. *Radiat Res* 172, 653-665, doi:10.1667/RR1926.1 (2009).

- 47 Kodibagkar, V. D., Cui, W., Merritt, M. E. & Mason, R. P. Novel ^1H NMR approach to quantitative tissue oximetry using hexamethyldisiloxane. *Magn Reson Med* 55, 743-748, doi:10.1002/mrm.20826 (2006).
- 48 Mayer, A. *et al.* Lack of correlation between expression of HIF-1 α protein and oxygenation status in identical tissue areas of squamous cell carcinomas of the uterine cervix. *Cancer Res* 64, 5876-5881, doi:10.1158/0008-5472.CAN-03-3566 (2004).
- 49 Hutchison, G. J. *et al.* Hypoxia-inducible factor 1 α expression as an intrinsic marker of hypoxia: correlation with tumor oxygen, pimonidazole measurements, and outcome in locally advanced carcinoma of the cervix. *Clin Cancer Res* 10, 8405-8412, doi:10.1158/1078-0432.CCR-03-0135 (2004).
- 50 Bloembergen, N., Purcell, E. & Pound, R. Relaxation Effects in Nuclear Magnetic Resonance Absorption. *Physical Review* 73, 679-746 (1948).
- 51 Perozzo, R., Folkers, G. & Scapozza, L. Thermodynamics of protein-ligand interactions: history, presence, and future aspects. *J Recept Signal Transduct Res* 24, 1-52 (2004).
- 52 Paulik, M. A. *et al.* Development of infrared imaging to measure thermogenesis in cell culture: thermogenic effects of uncoupling protein-2, troglitazone, and beta-adrenoceptor agonists. *Pharm Res* 15, 944-949 (1998).
- 53 Foy, B. D., Rotem, A., Toner, M., Tompkins, R. G. & Yarmush, M. L. A device to measure the oxygen uptake rate of attached cells: importance in bioartificial organ design. *Cell Transplant* 3, 515-527 (1994).
- 54 Herst, P. M. & Berridge, M. V. Cell surface oxygen consumption: a major contributor to cellular oxygen consumption in glycolytic cancer cell lines. *Biochim Biophys Acta* 1767, 170-177, doi:10.1016/j.bbabbio.2006.11.018 (2007).
- 55 Zhang, Y. *et al.* Loss of manganese superoxide dismutase leads to abnormal growth and signal transduction in mouse embryonic fibroblasts. *Free Radic Biol Med* 49, 1255-1262, doi:10.1016/j.freeradbiomed.2010.07.006 (2010).
- 56 Abe, Y. *et al.* Bioenergetic characterization of mouse podocytes. *Am J Physiol Cell Physiol* 299, C464-476, doi:10.1152/ajpcell.00563.2009 (2010).
- 57 Sridharan, V. *et al.* O(2)-sensing signal cascade: clamping of O(2) respiration, reduced ATP utilization, and inducible fumarate respiration. *Am J Physiol Cell Physiol* 295, C29-37, doi:10.1152/ajpcell.00466.2007 (2008).
- 58 Yamada, T., Yang, J. J., Ricchiuti, N. V. & Seraydarian, M. W. Oxygen consumption of mammalian myocardial cells in culture: measurements in beating cells attached to the substrate of the culture dish. *Anal Biochem* 145, 302-307 (1985).
- 59 Almeida e Sousa, L. *et al.* Calorimetric determination of rate constants and enthalpy changes for zero-order reactions. *J Phys Chem B* 116, 6356-6360, doi:10.1021/jp302933f (2012).
- 60 Di Trani, J. M. *et al.* Rapid measurement of inhibitor binding kinetics by isothermal titration calorimetry. *Nat Commun* 9, 893, doi:10.1038/s41467-018-03263-3 (2018).

- 61 Hill, B. G., Dranka, B. P., Zou, L., Chatham, J. C. & Darley-Usmar, V. M. Importance of the bioenergetic reserve capacity in response to cardiomyocyte stress induced by 4-hydroxynonenal. *Biochem J* 424, 99-107, doi:10.1042/BJ20090934 (2009).
- 62 Zhang, X., Lin, Y. & Gillies, R. J. Tumor pH and its measurement. *J Nucl Med* 51, 1167-1170, doi:10.2967/jnumed.109.068981 (2010).
- 63 Raghunand, N. *et al.* Enhancement of chemotherapy by manipulation of tumour pH. *Br J Cancer* 80, 1005-1011, doi:10.1038/sj.bjc.6690455 (1999).
- 64 Helmlinger, G., Yuan, F., Dellian, M. & Jain, R. K. Interstitial pH and pO₂ gradients in solid tumors in vivo: high-resolution measurements reveal a lack of correlation. *Nat Med* 3, 177-182 (1997).
- 65 Lindner, D. & Raghavan, D. Intra-tumoural extra-cellular pH: a useful parameter of response to chemotherapy in syngeneic tumour lines. *Br J Cancer* 100, 1287-1291, doi:10.1038/sj.bjc.6605022 (2009).
- 66 Vassiliou, C. C., Liu, V. H. & Cima, M. J. Miniaturized, biopsy-implantable chemical sensor with wireless, magnetic resonance readout. *Lab Chip* 15, 3465-3472, doi:10.1039/c5lc00546a (2015).